Distribution Agreement

In presenting this thesis or dissertation as a partial fulfillment of the requirements for an advanced degree from Emory University, I hereby grant to Emory University and its agents the non-exclusive license to archive, make accessible, and display my thesis or dissertation in whole or in part in all forms of media, now or hereafter known, including display on the world wide web. I understand that I may select some access restrictions as part of the online submission of this thesis or dissertation. I retain all ownership rights to the copyright of the thesis or dissertation. I also retain the right to use in future works (such as articles or books) all or part of this thesis or dissertation.

Signature:

Kevin Michael Roenitz	Date

The Search for Interstellar Organic Ions

By

Kevin Michael Roenitz
Doctor of Philosophy
Chemistry

Susanna Widicus Weaver, Ph.D.
Advisor

Francesco Evangelista, Ph.D.
Committee Member

Michael Heaven, Ph.D.
Committee Member

Accepted:

Lisa A. Tedesco, Ph.D.
Dean of the James T. Laney School of Graduate Studies

Date

The Search for Interstellar Organic Ions

By

Kevin Michael Roenitz
B.A., Illinois Wesleyan University, 2015

Advisor: Susanna Widicus Weaver, Ph.D.

An abstract of
A dissertation submitted to the Faculty of the
James T. Laney School of Graduate Studies of Emory University
in partial fulfillment of the requirements for the degree of
Doctor of Philosophy
in Chemistry
2020

Abstract

The Search for Interstellar Organic Ions

By Kevin Michael Roenitz

Interstellar clouds are the cold, dark regions that eventually undergo gravitational collapse to form stars and ultimately new planetary systems. During star formation, complex organic molecules that form on the icy mantles of dust grains are liberated into the gas phase in so-called "hot cores". The molecules released encounter H_3^+, the most common ion in the interstellar medium (ISM). In the gas phase, the complex organic molecules can now react with H_3^+, which acts as a proton donor, to protonate these organic molecules. It is theorized that these protonated organic ions fuel the production of larger organic molecules in the ISM through ion-molecule reactions with polar species. The most common complex organic molecule that enters the gas phase from the icy grains is methanol and therefore the most common complex organic ion in the ISM is predicted to be protonated methanol. This ion has yet to confirmed as its rotational spectrum has not be recorded. As such, this ion has been of major interest in the field of astrochemistry. In addition, protonated methanol is highly fluxional as it has both a methyl rotor, and a H_2O wagging motion and is isoelectronic to methylamine. These characteristic makes it an appealing ion to study for spectroscopists studying fundamental properties of fluxional molecules. Due to the difficulty of trying to observe and assign its rotational transitions, work has been conducted to help improve our ability to do so. This has taken the form of instrumentation development of microwave-(sub)millimeter double-resonance and in the development of lock-in fast-sweep. Additionally, work has been done to ease the assignment of protonated methanol by removing potential spectral "weeds" that might arise during its spectral study by investigating a number of methanol clusters including argon-methanol, methanol-water, and methanol-methanol. Lastly, as a forerunner to protonated methanol experiments, attempts have been made to produce and observe protonated formaldehyde. This ion is thought to be a possible precursor to the formation of interstellar glycine, the simplest amino acid.

The Search for Interstellar Organic Ions

By

Kevin Michael Roenitz
B.A., Illinois Wesleyan University, 2015

Advisor: Susanna Widicus Weaver, Ph.D.

A dissertation submitted to the Faculty of the
James T. Laney School of Graduate Studies of Emory University
in partial fulfillment of the requirements for the degree of
Doctor of Philosophy
in Chemistry
2020

Acknowledgement

This was actually the hardest part of my thesis to write; not because I didn't know how I wanted to thank all my amazing family, friends and colleagues, but because I was at a loss for words on how to describe my time in grad school. Some days, it was hard just to get out of bed, but other days were full of joy. How does one even begin to describe such paradoxical events over the course of five years? All that I can say is that I was blessed to have so many people who cared and supported me throughout my time here at Emory University.

I want to first thank my advisor, Susanna Widicus Weaver, for all of your patience, kindness, unbelievable support and belief that I was more than up to the task of getting my doctorate. The first few years were incredibly hard on me, but you always stood by me and helped me get my bearings with a supportive chat or useful kick in the behind. That support helped me get my first win in lab when I was able to produce and detect protonated formaldehyde on my own. After that, successes in lab came more often and my belief in myself greatly increased. You are simply the best adviser I could have ever imagined. Period.

I want to thank my committee members, Dr. Michael Heaven and Dr. Francesco Evangelista, for their support and guidance over the past five years. I greatly appreciate the thoughtful questions and comments about my work over the years including both my lab work and proposals. I am also thankful for the ability to always come to you both for guidance when I encountered a problem I didn't know how to approach. I greatly appreciate the belief you both had in me to succeed and the time you gave me to make sure that happened.

Next I want to thank my amazing fiancè, Sarah Fleischauer. We started seeing each other just at the start of my second year right before things got really difficult for me and you have stuck with me throughout. I am eternally grateful for all your love, compassion, and support during my grad school career. You always were able to see the best in me and helped show me that when I started to doubt myself. Additionally, I will also be in you debt for reading and editing every single page of this thesis. You are the love of my life and I look forward to our next adventure as we move to Portland and begin our life together. I love you with all my heart!

My family, Mom, Dad, and my sister Christine have been incredibly supportive even while I've been literally across the country. Knowing that you guys are just a phone call away and that you will always pick up and talk with me helped make that distance feel much smaller than it actually was. Your love and support really mattered to me and helped me adjust to life at grad school. I also have to say all the little care packages and gift cards to Einstein's really helped me get through writing my thesis. Thank you for everything you guys have done to make my life just that much easier. I love you all so so much!

I could not have completed this journey without my best friends John, Britta, Jared, Houston, Alec, and Chase. You guys have helped me get through each stage of my grad school career with the long phone calls, daily lunches during the work week, and all the support you guys could muster. It meant the world to me that I could talk to you guys and blow off some steam or just catch up with whatever crazy

stories you guys had to tell. And to be frank, there was a lot of crazy stories you guys had to tell! I cherished these moments and look forward to many more wild and crazy stories and times with you all!

Also I could not have done this without the help of my amazing labmates. First I want to thank my friend and mentor, Dr. Luyao Zou, for helping learn how to work in lab and helping to mentor me with how to go about tackling problems. To AJ, who always helped me get through the day with a laugh and a smile. To Morgan, who was always there for a nice long chat about life and anything else that was one our minds. To Carson, for your support and kindness as we struggled through grad school together. To Hayley, Connor, and Kat, with your endless support, sass, and insightful questions that helped me be a better friend and mentor to you all. And lastly to my labmate, Chase, who has become one of my closest friends - you got this and have a blast with Hayley with your move to Wisconsin! Also I want to thank my dear friend Dr. Mallory Green who was always there for me when I need help and support as we through our degrees. Best of luck in Berlin! I know you will do great!

Before starting this grand adventure through the work I completed while at Emory, I have a few word I want to say to my current labmates. You guys are simply amazing and each of you have incredibly bright futures. I know the next few years will be hard with some of you moving to Madison and Maryland, and others staying in Georgia, but you will always have each other there to support you on your way. We may not be all in the same place or even time zone, but if you guys ever need help or just want to chat I will always be there for you for whatever you need. You guys will make it and are truly some of the best scientists and people I have ever been blessed to have in my life. So, thank you and good luck. I will always be cheering for you.

Table of Contents

List of Figures

List of Tables

Chapter 1 Introduction and Motivation

1.1 The Interstellar Medium and Astrochemistry

The interstellar medium (ISM) consists of the matter that is found between solar systems. The ISM is comprised of diffuse clouds, dense clouds, and warm star-forming regions called "hot cores". This matter and how it is formed and chemically evolves is the focus of the research being conducted in the Widicus Weaver lab. This research specifically focuses on how the precusors of life - amino acids, sugars, and other biomolecules - were formed. It has been well established that amino acids have been detected in meteorites, but it has not been established how and where those amino acids are formed [1, 2]. With complex organic molecules forming on the icy mantles of dust grain surfaces in the ISM, it is possible to build up some chemical complexity [3–5]. As the mass of the dust cloud starts to increase, the dust will being to gravitationally collapse in order to form a star [6]. This produces a star-forming region where the increased temperature sublimates these complex organic molecules, which can then interact with ions and radicals found in the gas phase [7, 8]. Once in the gas phase and possibly ionized due to cosmic rays, the complexity of the molecules increases through ion-molecule reactions [8]. Each of these steps in the evolution of complex organic molecules is an area of study in the Widicus Weaver lab. In particular, the focus of the research contained in this dissertation centers on the ionization and subsequent reactions produced when complex organic molecules desorb off of the icy mantle of the dust grains and interact with ions and ionizing radiation found in the gas phase.

In order to better understand the goals of this work it is important to understand each major component of the ISM and how these unique regions contribute to the

chemical evolution that occurs in interstellar space. In a dense cloud, the temperatures are around 10 K and there is a density of around ∼1,000 cm^{-3} [3, 6]. The temperature tends to be slightly lower here than the rest of the ISM due to the fact that these clouds are so dense that photons cannot penetrate deep into the cloud. Thus, while the edges of the dense cloud are around 30 K, the inner regions are much colder at 10 K. Due to low temperatures present in this region, most molecules tend to freeze to the icy mantles of dust grains. Once frozen on to the icy mantle, the molecules can then react with each other and increase the chemical complexity on the grain.

This is how carbon monoxide, the most common organic molecule, undergoes hydrogenation to produce methanol - the most common complex organic molecule [4, 9]. The addition to carbon and hydrogen atoms to carbon monoxide on the grain surface leads to larger alcohols and aldehydes [4, 10–14]. If instead of carbon monoxide being the molecular backbone, a nitrile undergoing hydrogenation will form methylamine [11, 15]. This is theorized to be a precursor to interstellar glycine. When in mixed ices with HCN, NH_3, and an aldehyde, it is possible to form amino acids in a laboratory setting [12]. No amino acids have been comfirmed to be present in the ISM [1, 2]. In addition to hydrogenation, more complex molecules can form from basic molecules like CH_4 and NH_3 under bombardment from cosmic rays and UV irradiation which cause radical reactions to occur on the grain surface [4, 6, 11, 12, 15–17]. This type of bombardment is very similar to what occurs in diffuse clouds.

In contrast with dense clouds, the diffuse clouds have different conditions and are thus dominated by a different set of chemical reactions. The diffuse clouds have a much lower number density, ∼10 to 1000 cm^{-3} with temperatures ranging between 30 to 100 K [3]. With the high temperatures, more molecules are still in the gas phase instead of being frozen out on grain surfaces [3, 7]. Due to the much lower density present in the diffuse clouds, light is better able to penetrate deep into the

cloud. This penetration means there is a high flux of ionizing radiation in the form of comsic rays and vacuum UV light [3, 7]. While this region is still primarily atomic or neutral species, it is theorized that ion-neutral reaction are the main driving force in gas phase chemistry.

The main reason for these ion-neutral reactions being the driving force behind gas phase chemistry is because of kinetics. Under terrestrial conditions, most reactions follow the Arrhenius rate law shown in Equation 1.1.

$$k = A(T)e^{-E_a/k_bT} \tag{1.1}$$

The rate coefficient k is determined by a rate factor A (which has a slight temperature dependence) the activation energy E_a, the Boltzmann constant k_b, and the temperature T. Due to the low temperature in the ISM, the activation energy typically dwarfs k_bT, which makes the exponential term a large negative number and thus the rate coefficient is very small [3]. Thus, most reactions do not proceed efficiently. In contrast, ion-neutral reactions follow Langevin kinetics shown in 1.2.

$$k = 2\pi e(\frac{\alpha}{\mu})^{1/2} \tag{1.2}$$

Here, the rate coefficient k is determined by the electronic charge, the polarizability α, and the reduced mass of the reactants μ [3]. This means that ion-neutral reactions are driven by the ratio between the polarizability and the reduced mass instead of the temperature. This means that a typical ion-neutral rate coefficient will be an order of magnitude or more larger than the neutral-neutral reactions simply because of the difference in kinetics that drive the gas phase chemistry [3]. The most common ion that forms in the ISM is H_3^+, which acts as a proton source in the gas phase [3, 7]. This ion can then react with a number of common neutral molecules and atoms in the gas phase like H_2, CO, CH_4, C_2H_2, O, N and C to form more complex ions and molecules [3, 7, 9, 17]. These ions then go on to react with polar molecules to form

larger and larger molecular species.

With the basics of both the dense and diffuse clouds detailed, it is now possible to discuss star-forming regions. A star-forming region has the high molecular density seen in dense cloud regions, with density of 10,000 or more molecules/cm^3, but with increased temperatures ranging from 100-300 K [3, 4, 7]. This means the temperature is high enough for the complex molecules to desorb off of the grain surfaces and now interact with the ions and proton sources that are present in the gas phase [9]. This allows complex organic molecules like methanol to react with H_3^+ and become protonated. With H_3^+ being the most common ion in the ISM and methanol being the most common complex organic molecules, it is reasonable to predict that protonated methanol would be the most complex organic ion.

Protonated methanol is predicted to be in the ISM, but has yet to be confirmed because no rotational spectra have yet been recorded in the laboratory [18]. Despite not being confirmed yet, it is predicted to be a major contributor in producing large complex organic molecules like methyl formate and glycolaldehyde in the gas phase [2]. There have been some studies on protonated methanol focusing on kinetics and its infrared spectrum [18–21]. Despite these works, it has yet to be detected in the gas phase with rotational spectroscopy. This is partly because it is a difficult ion to form in sufficient quantities to detect. Also, protonated methanol is isoelectronic with methylamine, and is likewise subject to large amplitude motions [22]. Consequently, the rotational spectrum of protonated methanol will be very complex and thus hard to analyze. These problems necessitate the development of new techniques in order to better produce, detect, and then assign the spectrum of protonated methanol.

1.2 Current Techniques and Instrumentation in the THz Regime

Rotational spectroscopy can trace it is roots back to World War II with the advent of radar [23]. Over the past century the technology and techniques used to produce and detect in the microwave and millimeter/submillimeter regime have advanced dramatically. The use of rotational spectroscopy to detect molecules in the ISM is based on its ability to differentiate between molecules based on their structure [24]. Each molecule has its own unique rotational constants based off the dipole moments of the molecule. As such, if a molecule does not have a dipole moment it cannot be detected. However, this still leaves a large number of molecules that can be detected. Thus, rotational spectroscopy is the ideal technique used to detect molecules in the ISM [24]. To be able to detect molecules in the ISM, one must first be able to record their spectra using radio astronomy. After that, the recorded spectra must be compared to the spectra of known molecules. The spectra of the known molecules are produced in a laboratory and as such new techniques and instrumentation have been developed in order to better detect these molecules. There are a number of ways to produce and detect astronomically relevant molecules. Here, these varied techniques will be discussed. First the production of molecules and ions and the instrumentation used to do so will be examined. After that, the production and detection of light in both the frequency and time domain will be studied along with the techniques used to increase sensitivity, detect chirality, and help assign complex rotational spectra.

The ideal environment to conduct these experiments is under vacuum conditions for three main reasons: the primary reason is that one has to conduct these experi-

ments in the gas phase in order to see rotational lines, the secondary reason is to limit the effects of pressure broadening on the recorded spectra, and the tertiary reason is to mimic the conditions of the ISM [24]. The low pressures are needed in order to produce an environment where unstable ions and molecules can be produced and remain intact long enough to be detected. The simplest way to introduce a sample into the gas phase is to use a vacuum pump in order to pull vapor off of the sample and into the gas phase [24, 25]. One can pass this vapor through a long-path spectrometer to increase sample pathlength; such a setup is called a flow cell. Another way to deliver gas samples into a vacuum chamber is by using a pulsed valve [24, 26]. Delivering high-pressure gas to a low-pressure regime through a small aperture forms a supersonic expansion, which is adiabatic and as such can be used to rotationally cool the molecules of interest.

Once a gas-phase precursor gas is delivered, there are a number of ways to ionize molecules using a flow cell or a pulsed valve. First, flow cell-based ion sources will be briefly discussed. With a continuous flow of sample, a discharge can be struck across a long pathlength flow cell in order to ionize the gas sample. There are a number of different flow cell-based ion sources like a positive column discharge, negative glow discharge, or a hollow cathode discharge source [24, 27, 28]. These discharge sources tend to produce ions at roughly room temperature or above due to heating caused by the discharge source. The type of discharge source to be used in an experiment is selected based on the target ion and which chemistry is being utilized in order to produce the ion. For instance, a hollow cathode discharge source is typically very efficient at producing protonated ions [24]. The one benefit and drawback of producing ions in a flow cell is the high number density. The high number density means detecting ions should be much easier as the number of absorbers is high. This also means it will be difficult to produce and maintain sufficient number density of highly unstable ions in order to be successfully detected using millimeter/submillimeter spectroscopy. In

order to circumvent this problem, switching to a pulsed valve based discharge source would be ideal.

The major benefit to using a pulsed valve based discharge source is to take advantage of the supersonic expansion produced when using one [24, 29]. The supersonic expansion has two major effects on the discharge. The first effect is that having the ionized gas undergo a supersonic expansion rotationally cools the ions dramatically. This forces population to be in the lower J states and thus makes detecting transitions between those lower J levels significantly easier. The second effect is that during a supersonic expansion, the expansion physically separates the gas particles from each other. This quenches any reactions occurring in the discharge source, allowing for unstable ions to be produced and then maintained. A drawback to this approach is it causes a decrease in the number density of the ions being produced. There are possible solutions to this problem, for example using an ion trap [24, 30]. There are a number of discharge sources that can be used in conjunction with a pulsed valve that include ring, needle, and slit electrode discharge sources [24, 29, 31]. Depending on the production method for the target ion, the ideal discharge source can be selected and utilized to produce the target ion.

Once the ion of interest is formed, the simplest way to detect molecular signal is by using direct absorption. This is a technique that takes the generated light, shines it through the sample, and then detects the amount of light hitting the detector [24]. The amount of light reaching the detector will decrease when on a frequency of light that the sample absorbs. While this technique only requires a light source, a sample, and a detector, it is slow and not a particularly sensitive technique. It is a slow technique because it steps across frequency space in a point-by-point fashion. As most spectral lines have a frequency width of $\sim$1 MHz in this frequency regime, the step size needs to be at a minimum of 100 kHz in order to reasonably resolve the line. However, there are a number of techniques that have been developed in

order to increase data acquisition speed. In addition, without any data processing or an increase in pathlength, direct absorption measurements tend to not be the most sensitive detection method available.

The first major drawback to direct absorption is stepping across frequency space in a point-by-point fashion is slow. As such there have been a number of techniques developed in order to increase the data acquisition rate for rotational spectroscopy. The first technique developed is the FASSST technique which utilized a frequency sweep to quickly scan through a large frequency range [24, 32, 33]. This technique originally had to rely on a Fabry-Perot cavity in order to maintain a frequency calibration for the sweep produced by a backward wave oscillator. This has been since upgraded to a direct digital synthesis card to produce and maintain the frequency sweep [33, 34]. The next big development in increasing data acquisition rate was the advent of chirped-pulse Fourier transform microwave experiments. Here, a large frequency sweep across several gigahertz or more is rapidly cycled on the time scale of a microsecond. The generated light then interacts with a gas sample and then the free induction decay is recorded in the time domain. Using a Fourier transform the time domain data would be converted into the frequency domain. This technique allows for large swathes of frequency to be recorded quickly and with a high number of averages [24, 34, 35]. This technique has recently been extended to cover parts of the millimeter/submillimeter region. These two techniques unfortunately require a lot of capital in order to purchase the equipment to effectively run these experiments. This helped push for the development of a new approach, which our group has developed and named fast sweep. This will be discussed in detail the subsequent chapter. It is essentially an inexpensive version of the latest FASSST system that produces the frequency sweep using a the FM modulation in the microwave synthesizer instead of producing it with a specialized piece of equipment [24, 36].

With the advances in data acquisition discussed, another important aspect is

techniques used to enhance sensitivity. One very simple technique used is a phase-sensitive detection like lock-in detection [24]. This technique will also be discussed in subsequent sections in detail, but in short it allows for a way to dramatically decrease the noise while improving the signal. Another way to enhance sensitivity is to increase the pathlength of the light interacting with the sample. This can be done using a multi-pass optical arrangement or by using an optical cavity [24, 37, 38]. A multi-pass increases the number of times the light interacts with the sample. This is achieved by using mirrors to reflect light through the sample in a way that is not frequency dependent. This means that any frequency of light will have the number of passes increased. In contrast, an optical cavity is frequency dependent, but can dramatically increase the number of times the light interacts with the sample [24, 39, 40]. In practice, this means that an optical cavity has more passes, but has to be continuously adjusted to cover the entire frequency range. However, a multi-pass optical arrangement can be set once and never needs to be adjusted to cover the entire frequency range.

Now, stepping away from data acquisition rates and sensitivity, it is important to discuss techniques used to assign the spectra of highly fluxional molecules and ions and determine chirality of a molecule. Double-resonance spectroscopy is a well-developed technique that has the ability to probe the interconnectivity of states in a molecule. Double-resonance is a multiphoton absorption process where the first photon (the pump) excites a transition from a lower state to an upper state; the second photon (the probe) then excites a different transition. If this transition shares either the lower or upper state of the pump transition, then the two transitions are connected and a signal modulation will appear when both the pump and probe are present [41]. This approach provides insight as to which transitions involve states that are connected to the pump transition and which do not. Because of the ability to show the interconnectivity between the states, double-resonance techniques are appealing

tools for the study of complex molecules that have complicated spectra arising either from multiple vibrational states being populated, or from effects of internal motion leading to complex spectral patterns.

Many experiments utilizing double-resonance have been conducted across a wide range of wavelengths, which include radio-microwave [42, 43], microwave-microwave [26, 44–49], microwave-millimeter [50–54], microwave-infrared [55–65], microwave-optical [66–71], microwave-ultraviolet [72, 73], microwave-X-Ray [74], millimeter-infrared [75], millimeter-optical [76–79], infrared-infrared [80–82], infrared-optical [83], infrared-ultraviolet [84–88], infrared-X-Ray [89], optical-optical [90–95], optical-ultraviolet [96], ultraviolet-ultraviolet [97, 98], ultraviolet-X-Ray [99], and phosphorescence-microwave [100, 101]. Of these previously conducted experiments, it is most relevant to focus on the five previous works reporting microwave-millimeter double-resonance. Three of these experiments were conducted by Endo and coworkers [50, 52, 54], while the other two were conducted by Jäger and coworkers [51, 53]. These double-resonance experiments were conducted with point-by-point scans, instead of using a chirp or a sweep modulation to achieve broadband coverage. They therefore are focused on detection of one transition at a time, and were limited by acquisition speed.

When conducting microwave-millimeter wave double-resonance measurements, there are four types of three level double-resonances that can occur. The microwave transition can be resonant with either the lower or upper level of the millimeter wave transition via either its own lower or upper level. See Figure 1.1 for the energy level diagram for methanol as an example.

Microwave-millimeter/submillimeter wave double-resonance is an important development for spectroscopy because of the specificity of rotational spectroscopy. Each molecule has unique rotational constants that are structure specific, and thus each molecule has a unique rotational spectral fingerprint. This combined with the high-resolution nature of rotational spectroscopy leads to unambiguous methods for identi-

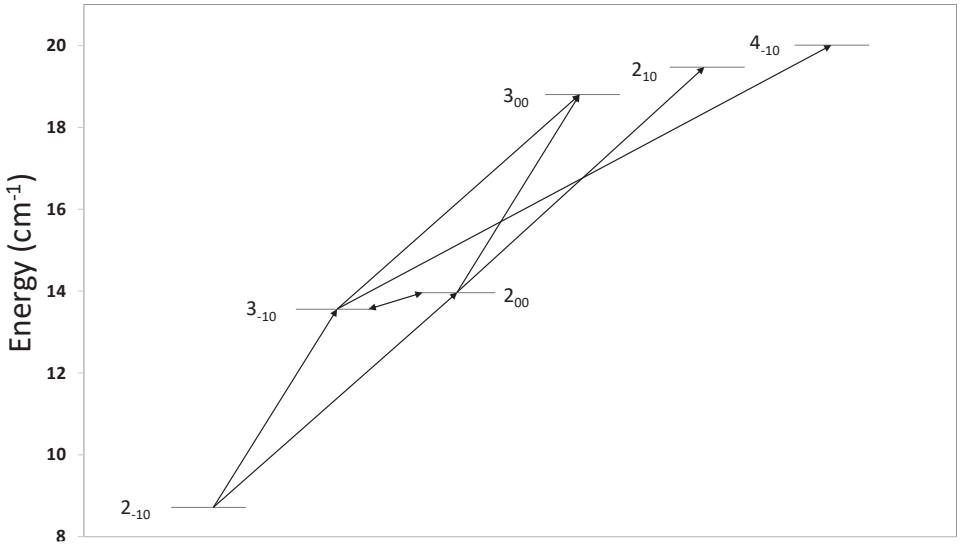

Figure 1.1: The possible double-resonance connections between methanol rotational states. The microwave transition is indicated by the double-headed arrow, while the millimeter/submillimeter transitions are indicated by the single-headed arrows. The state labeling is J $\pm$ K v_t, where $\pm$ indicates the level parity and v_t gives the vibrational quantum number of the methyl torsion. This is the same notation used for methanol in the JPL spectral line catalog. [102]

fication of molecules in a mixture, and detection of weak signals from unstable species. However, the spectra of organic molecules with large amplitude internal motion are often so complex that spectral assignment is challenging without information from multiple spectrometers covering different frequency ranges. The double-resonance technique described here uses technology from broadband techniques which offers a rapid method for line identification that can be used to ease the spectral assignment problem.

Building off of double-resonance, three-wave mixing can be utilized to determine the chirality of molecules. Until recently it was not possible to determine the chirality of a molecule using rotational spectroscopy. That has since changed with the advent of three-wave mixing [103]. This is done by pumping a base transition and a twist transition and then probing a third transition and determining how the phase shifts in response in the free induction decay [103]. This technique is very similar to traditional double resonance experiments, but has the added complexity of the probing the third transition in order to determine the chirality of the molecule.

We have applied various combinations of these ion sources, spectroscopic techniques, and instrument designs to begin assembling the tools needed to study the rotational spectra of complex organic ions that are important in astrochemistry. The specific goals of this is to produce protonated methanol using a pulesd supersonic expansion discharge source. The supersonic expansion is necessary due to how reactive the ion is. Additionally, this is a highly fluxional ion that will require new techniques and instrumentation in order to produce, detect, and assign its rotational spectrum.

1.3 Target Ions and Clusters

As mentioned above, protonated methanol is predicted to be the most common complex organic ion in the ISM, but as of yet it has not been detected and its rotational spectrum recorded using rotational spectroscopy. It is also predicted to be a

highly fluxional ion with a methyl rotor and H_2O wagging motion. These problems led to the development of double resonance in order to help assign protonated methanol. In addition to being able to assign the recorded spectrum, one must actually be able to produce the ion of interest. As this ion has never been recorded with rotational spectroscopy, it would be beneficial to attempt to produce a similar ion to protonated methanol, but have a previously recorded rotational spectrum. That led us to study protonated formaldehyde.

Protonated formaldehyde is structurally similar to protonated methanol, and has been previously detected using infrared spectroscopy and then recorded using rotational spectroscopy [27, 104–106]. These studies produced protonated formaldehyde initially using a hollow cathode in the Amano work, and then shifted to a negative glow discharge for the other three works. The frequency range covered by these studies included 3420-3500 cm^{-1} and 110-385 GHz. In addition to the rotational spectra, there has been some experimental work on determining the structure, electron-ion dissociative recombination rate constants, and infrared photodissociation spectrum [107–110]. With this body of work supporting our efforts, it was predicted that it would be possible to produce and detect protonated formaldehyde. These efforts are detailed in a subsequent chapter.

Before Bowen's work using mass spectrometry to determine the structure of protonated formaldehyde, the exact structure was of great debate for theoretical calculations. This led to a large body of work centered on predicting the structure of protonated formaldehyde, its rotational and vibrational constants and frequencies, and dissociation energy [111–120]. This work helped to inform where to search for spectral lines in both the infrared and the millimeter/submillimeter. Some work has been conducted on the valence and Rydberg states which also produced the predicted electronic spectrum of protonated formaldehyde [121]. All of this theoretical and experimental work has helped guide astrochemical studies for the production of

sugars in the ISM [122, 123]. This is due to the confirmed presence of protonated formaldehyde in the ISM.

Protonated formaldehyde has been confirmed in a number of sources in the ISM which include: Sgr B2, Orion KL, W51, Mc G+0.693, and L1689B [124–127]. It is predicted that interstellar protonated formaldehyde is produced through a proton transfer reaction involving formaldehyde and a proton donor, which is typically H_3^+, HCO^+, and H_3O^+ or by the loss of molecular hydrogen from methanol in order to produce the ion [124]. This theory seems well supported as formaldehyde, methanol, H_3^+, HCO^+, and H_3O^+ are seen where protonated formaldehyde is also detected [124, 128–130]. In addition to being a pathway for methanol and formaldehyde destruction in the ISM, protonated formaldehyde has a role in the deuterium fractionation of formaldehyde as deuterated formaldehyde can be produced by protonated formaldehyde [131, 132]. With this body of work in its current state and with the progression into higher frequency observations thanks to the Atacama Large Millimeter/submillimeter Array (ALMA), it behooves us to record the spectrum of protonated formaldehyde beyond 385 GHz.

Some of the possible routes to produce protonated methanol and protonated formaldehyde involve using methanol, hydrogen, and a inert backing gas in a supersonic expansion or flow cell discharge source. In order to minimize side reactions produced by a discharge source, a supersonic expansion is used to quench the reactions by decreasing the number of collisions. When expanding a sample with an inert backing gas like argon it is possible to form van der Waals clusters [133]. Since it will be necessary to use methanol and argon in a supersonic expansion discharge source to produce protonated methanol, it is necessary investigate the possible clusters that can form in order to isolate the discharge product lines. When attempting to produce protonated methanol, there will be three likely clusters produced: argon-methanol, methanol-water, and methanol-methanol. There have a been a number of

studies in the microwave regime focused on these clusters [133–138]. None of these clusters have spectra recorded in the millimeter/submillimeter regime. As such, their millimeter/submillimeter spectra will have to be predicted before any attempts to record their actual rotational spectra can occur. There has been some additional work focusing on the structure, intermolecular potentials, and infrared spectra of these clusters [139–142]. None of these clusters have been detected in the ISM as of this now, but this is possibly due to the lack of any millimeter/submillimeter spectra. It also most be noted that due to the low densities found in the ISM that the formation of such clusters is not facile [143]. Once these spectra are produced, it will be possible to compare the laboratory spectra to those collected by radio astronomy in order to determine if there are present in the ISM.

With this general background on the need for spectrometers and techniques that can detect and help assign highly fluxional ions and the overview of the targets of interest, it is now possible to proceed to how these experiments were conducted. Next, the general instrumentation used for the experiments will be discussed and then expanded upon with the developments made in order to help achieve the goal of recording and assigning complex organic ions. After that, the work done to produce the rotational spectra of protonated formaldehyde and argon-methanol will be discussed. Lastly, the overall impact of this work will summarized.

Chapter 2 Instrumentation

Several experimental methods were employed to begin the search for protonated ions. This section will provide a general overview of the instrumentation used, as each experiment has utilized these basic designs and then expanded upon the basic principals in order to achieve specific aims. In addition, there will be discussion of the limitations of the experimental techniques employed and how to overcome some of these limitations. Therefore, a thorough understanding of the basic designs is necessary before going into detail on how to best utilize the equipment in order to achieve the experimental goals of the experiments.

2.1 Discharge Sources

The main focus of this research has been on the creation and detection of ions, and as such it has been necessary to develop different types of ion sources to achieve these target ions. Before going into the experimental details, it is necessary to understand some of the basics of discharge and plasma chemistry. The fundamental concept of a discharge source is to run high voltage through a gas in order to ionize the gas. A plasma is formed, and a myriad of molecular products occur from chemical processes ranging from simple conformational changes to stripping a molecule of its electrons in order to produce an ion or a radical. These processes occur because the discharge source is acting as a pure energy source if it is supplying the necessary energy to break a bond or simply help the molecule get over a high energy barrier for a conformational change. The amount produced for each of these products is highly dependent on the voltage and current of the discharge, the shape and size of the discharge source, and any external forces acting upon the discharge such as magnets or even the Earth's magnetic field. As such, it is necessary to examine these factors when discussing the

discharge sources used to produce the results presented herein.

The two general types of discharge sources used in these studies utilize either a glow discharge or an arc discharge. The general differences between the two types of discharge are the voltage to current ratio and the necessity of thermal effects to cause the discharge [28]. A summary of different types of discharges is given in Figure 2.1. For glow discharges, the voltage tends to be in the hundreds of volts with only a few milliamps of current as shown in Figure 2.1. For these discharges to occur, the pressure of the ionizing gas needs to be in the range of a few millitorr. Additionally, while the discharge will produce heat, sometimes in large amounts, this heat is not needed in order for the production of ions to occur. The glow discharge works by the cathode emitting electrons that cause the gas that electrons bombard to become ionized. The the electrons tend to have higher energy but a lower flux when compared to the arc discharge, as is expected due to the high voltage and low current used to produce the discharge. A classic example of a glow discharge is the hydrogen lamp used to study the Balmer Series. This type of discharge produces light based on the spectral emission of the ionized gas instead of the metal of the electrodes [28].

In comparison, an arc discharge source tends to have lower voltage requirements but much higher currents as is shown in Figure 2.1. Thus the electrons tend to have lower energy, but higher fluxes. It must be stated that the initial strike voltages will be much higher than the running voltage. This is because the breakdown voltage, or the voltage required to induce the flow of the electrons is much higher than the voltage required to continue flowing the electrons. An arc discharge is produced when two electrodes are brought close enough together that the electrons arc from the high voltage electrode to the ground electrode. The arc is produced when the electrodes are supplied with enough thermal energy to create a flow of electrons, i.e., via thermionic emission [28]. As such, the light produced by an arc discharge will be the emission spectrum of the electrodes instead of the ionized gas. The classic

example of an arc discharge is lighting. The voltage for lighting is much higher than what would normally be expected as a result of the breakdown voltage required to induce the flow of electrons.

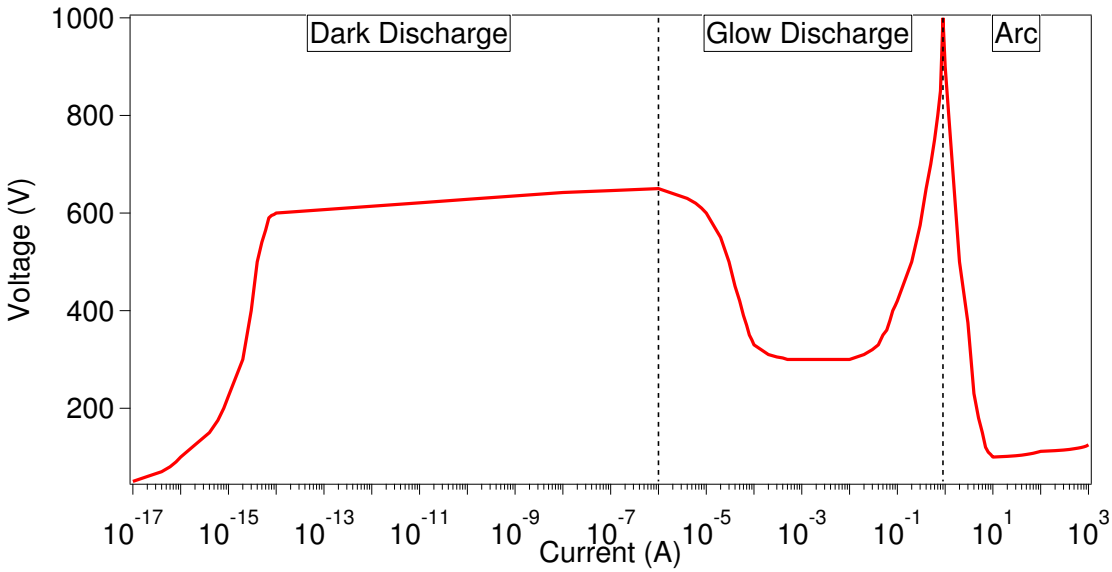

Figure 2.1: An overview of what type of discharges are produced with regards to the voltage vs. current. The black dashed line shows the separation between the different types of discharge. This image was reproduced from information found in the book Ionized Gases [28].

With the two general types of discharge sources discussed, there are a number of different parameters to consider when deciding on the type of discharge source and discharge conditions to use. Here we will focus on the types of discharge sources currently available for these studies. Each type of source and parameter used to produce the plasma will affect the chemistry occurring in the plasma. The following "rules" are more akin to guidelines and predictions than hard-and-fast rules. This is due to the fact that in a discharge, pure energy is being applied to a system, making it hard to predict exactly what will occur within the plasma as a number of reactions are occurring, creating diverse products. Certain parameters can be adjusted in order to promote a chosen reaction. For example, if the goal is to protonate a molecule it would be prudent to use an ion source that would promote collisions as protonation

occurs via the following reactions:

$$H_2 + HV \rightarrow {H_2}^+ + e^- \tag{2.1}$$

$${H_2}^+ + H_2 \rightarrow {H_3}^+ + H \tag{2.2}$$

$${H_3}^+ + R \rightarrow HR^+ + H_2 \tag{2.3}$$

For reference, "R" is a placeholder for the chemical formula of the neutral precursor molecule. As shown above in 2.1, 2.2, and 2.3, the protonation reaction requires multiple steps in order to protonate the sample. Therefore, in order to facilitate this reaction it is necessary to balance promoting enough collisions so that protonated molecules are formed, but not promoting so many that subsequent reactions are favored.

Sometimes the best way to produce the ion of interest is to strip a parent molecule of a hydrogen in order to form the ion. Here, a different ion source would be ideal as only one reaction is needed to form the ion of interest, with the goal being to form the ion and quench any further reactions. An example reaction of this type would be to make protonated formaldehyde using methanol as shown in 2.4.

$$H_3COH + HV \rightarrow H_2COH^+ + H + e^- \tag{2.4}$$

When aiming to produce a particular ion, one must choose the ion production method wisely. In our experiments, we used a hollow cathode source, a ring electrode source, and a needle electrode source. The hollow cathode and the ring electrode sources work via the protonation method where ${H_3}^+$ is formed, while the needle

electrode source works by striping off a proton to produce the ion of interest. It is important to note that the chemistry is very complex in discharges and other reactions will occur in addition to the reaction of interest. As such, when attempting to predict the amount of sample that will be produced the total ionization fraction is approximated to be $\sim 10^{-4}$, and any particular ion of interest will be $\sim 10^{-6}$ relative to the parent molecule.

The instrumentation used to produce the various ions of interest utilized a high voltage power supply (Spellman, SL2PN2000). This high voltage source applies a constant voltage to the electrodes allowing ionization to occur. Applying a constant voltage like this occurs only for the hollow cathode discharge source. When the discharge source was operated in conjunction with the pulsed valve, a pulse generator (Directed Energy Inc., PVX-4150) was used to pulse the voltage on and off along with the sample gas. This was done in order to properly synchronize the times of the pulsed valve and the discharge source. The pulse generator was used in conjunction with the ring electrodes and with needle electrode ion sources.

As a note of caution, discharge sources create significant radio frequency interference (RFI) which can be detrimental to signal collection in spectroscopic experiments, especially those using radio/cm/mm/submm wavelengths. There are some ways to mitigate the RFI by effectively grounding both the discharge source and the detector. In addition to the normal amount of RFI produced by running a discharge source, internal arcing of the discharge source may become a problem. Internal arcing occurs when the electrons that form the discharge strike ground inside the body of the source instead of flowing through the gas that is meant to be ionized. Internal arcing is caused by improper insulation or grounding within the discharge source.

The main ways to determine if the source is suffering from internal arcing is to monitor the noise in the spectrum, or by visually determining if there are flashes of light inside the discharge source in addition to the plasma expanding from the output

of the source. The primary way to fix this is to better insulate the high voltage wire so that the electrons in the wire do not arc to the grounding electrode through the basic wire insulation. This can be achieved by simply increasing the insulation on the wire with electrical tape. Typically, it is easy to determine the source of the arcing as there will be burn marks in the high voltage wire where it is arcing to ground. This problem is generally seen in the discharge sources used in conjunction with the supersonic expansion source.

2.1.1 Hollow Cathode Ion Source

A hollow cathode ion source is an example of a glow discharge source. The discharge is produced by striking a discharge between the hollow cathode and an anode. This produces a column of ionized gas throughout the hollow cathode. Having a much larger cathode in comparison to the anode allows for the cathode to extend the negative glow region of the discharge. This means the positive column is limited to the area between the anode and the cathode [144]. This region produces a large amount of positive ions and isolates them from the positive charge of the anode [28]. Therefore, having a large region in which positive ions are produced and then concentrated is beneficial when attempting to utilize the hollow cathode to produce different positive ions.

In our experiments, the cathode is a 1.4 m copper tube with a 5 cm diameter. A 1/4 inch copper tube was wrapped around the cathode and sliver soldered to the outside surface in order to establish good thermal conductivity. The hollow cathode produces the discharge with an operational pressure around 10-30 mTorr. Any higher than 30 mTorr and the effects of pressure broadening would be seen in detecting ions using lock-in detection (this technique is addressed in a subsequent section of this chapter). Before it is safe to strike a discharge, liquid nitrogen (Nexair) has to continuously circulate through the cathode as the discharge produces a vast amount

of heat. Additionally, the stainless steel anode is cooled by a chilled ethylene glycol recirculator (Super RMT Lauda Brinkmann, model RM6). Once liquid nitrogen was circulating throughout the entirety of the cathode's cooling line it was safe to strike the discharge. With the operating pressure established and cathode cooled, the discharge would be struck with a high voltage power supply (Spellman, SL2PN2000). The output voltage was held around 200-400 V with a current on the order of 100 mA. Ballast resistors around 1-10 kΩ can be applied in order to stabilize the discharge and decrease the output current if needed. The high voltage was connected to the central anode and the cathode was connected to ground.

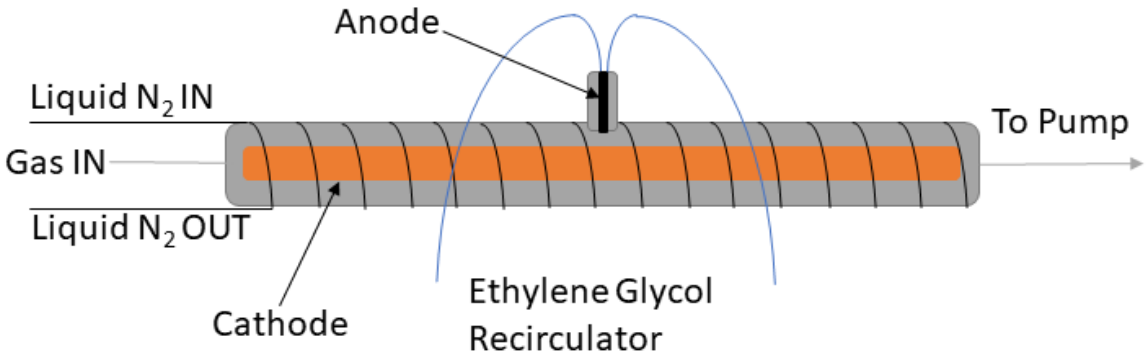

Figure 2.2: Diagram for the hollow cathode discharge source. The outer tubing on the cathode is the copper cooling lines for the liquid nitrogen to maintain optimal temperature. The stainless steel anode is cooled with an ethylene glycol recirculator. The output of the high voltage source is connected to the anode, while the cathode is grounded. Gas is flowed through the cathode while high voltage is applied to the anode in order to produce a discharge.

2.1.2 Needle Electrode Source

The needle electrode source used in our lab is an example of an arc discharge source. Here, a high voltage is applied to the needle electrodes in order to spark a discharge between the needles. This discharge source operates at the high end nearest to the glow discharge as it tends to run around 800 volts and under 10 mA. Due to the pulsed nature of this discharge source the voltage is higher while the current is lower than predicted by Figure 2.1. This is due to the discharge only being sparked

at a rate of ∼10 Hz and discharging for about 1 ms at most, meaning that it has to continuously operate around the breakdown voltage. The needle electrode source was developed to minimize the extent the discharge products could react with each other before undergoing a supersonic expansion. An example of the type of chemistry studied with such a source would be removing a hydrogen from methanol to form protonated formaldehyde.

The needle electrode source operates in a pulsed configuration and thus the high voltage power supply (Spellman, SL2PN2000) has its output routed through a pulse generator (Directed Energy Inc., PVX-4150). The pulsed generator was gated using a delay generator (Stanford Research Systems DG645) in order to have the discharge and gas to pulse at the same rate and to overlap in time. The output voltage of the power supply can operate with either positive or negative voltage. The positive voltage tends to produce a more violent discharge, while the negative voltage will produce a gentler discharge. Depending on the goal of the individual experiment, the polarity of the discharge would be selected in order to produce more or less fragmentation. Lastly, ballast resistors, 1-10 kΩ, can be applied to stabilize the discharge and decrease the output current if needed. The backing pressure of the gas can vary from 15 PSIG up to 250+ PSIG. The voltage, current, resistance, and backing pressure are all parameters that can be modified in order to more effectively produce the ion of interest.

2.1.3 Ring Electrode Source

The ring electrode source used in our lab is also an arc discharge source and is operated in a similar manner to the needle electrodes source, with a few exceptions. The major difference between the ring electrode source and the needle electrodes source is that the ring source forces collisions to occur during the discharge. This allows the discharge products to interact before the reactions are quenched by the

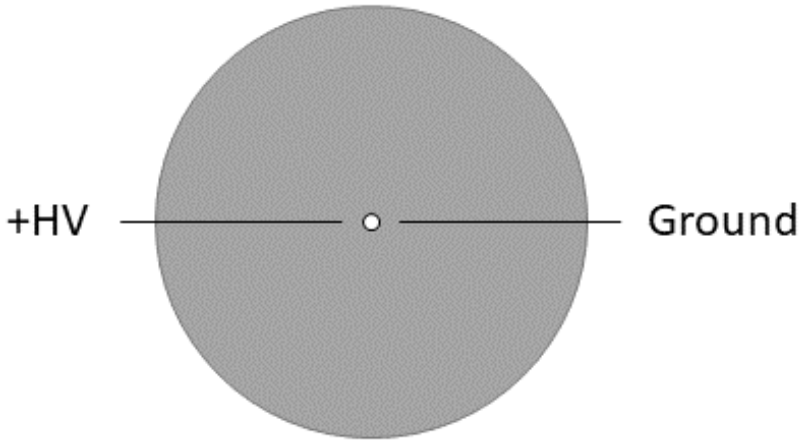

Figure 2.3: The needle electrodes are to standard sewing needles mounted to a teflon block and secured using to the pulsed valve with nylon screws and nuts. The electrodes are connected to the high voltage source using 1 kV rated wires in order to make sure the high voltage does not burn through the wires. The needles are separated from each other by 3 mm.

supersonic expansion. For some target products, this ion source would be more beneficial than the needle source. One such reaction scheme would be protonation as shown in Figures 2.1, 2.2, and 2.3. This particular design for the ring electrode discharge source was heavily inspired by the discharge source designed by Thaddeus and McCarthy [29].

In order to encourage or discourage the amount of collisions occurring in the discharge source, the inner diameter of the electrode could be changed. This inner diameter is also the gas channel that the sample gas flows through as is gets ionized. The standard inner diameter for the electrodes used in this work were 0.244 cm, but the diameters can be changed to 0.368 cm, 0.434 cm, and 0.515 cm. These inner diameter sizes correspond to the drill bit sizes #41, #27, #18, and 13/64. Changing the diameter can be beneficial to changing the reactions occurring within the discharge in order to impact the chemistry occurring within. The narrower diameters will force more collisions. The wider diameters will still allow these collisions, but will undergo the supersonic expansion slightly earlier than with the narrower diameters. Having these different diameters allows for one to modify the ring electrode source in order to

best produce the ions of interest. This can be done by having a narrower grounding electrode, but having the widest high voltage electrode. The ability to customize the ring electrode source allows for an increased ability to tailor the discharge source for each ions of interest, increasing the chances that ion production will be successful.

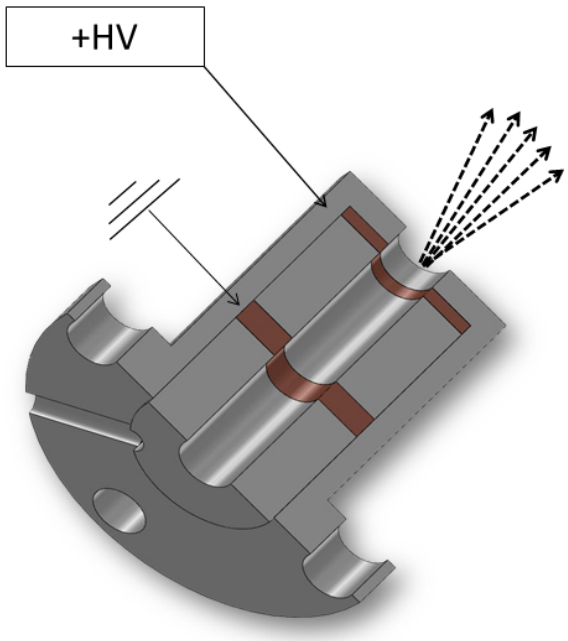

Figure 2.4: Ring electrode source design. The ring electrodes are housed in a Teflon container specially designed for them. The electrodes are separated from each other by a 0.5 in telfon spacer. The high voltage electrode is nearest the exit point of the source, while the grounding electrode is 0.5 in closer to the pulsed valve. The remaining space from the grounding electrode to the pulsed valve is buffered by a teflon spacer. The teflon is used to electrically isolate the electrodes and the pulsed valve to prevent damage or improper discharging from occurring.

2.2 Vacuum Systems and Sample Delivery

In order to fully describe how our molecular signals were measured, it is necessary to discuss the vacuum system. There were two major vacuum systems utilized in the collection of the data presented in this body of work. The first system housed a supersonic expansion discharge source, while the second housed a hollow cathode discharge source. There are certain pieces of equipment that are shared by both

systems and as such these will be described together. But, as the equipment becomes more specialized they will be described separately for clarity.

The vacuum was produced using a roots blower and rotary vane combination pump (Oerlikon-Leybold WSU 2001 and SV630 B(F)). This rough pump was able to achieve baseline pressures of $\sim$ 5 mTorr in the vacuum chamber housing the supersonic expansion source and $\sim$ 1 mTorr in the flow cell housing the hollow cathode ion source. For both vacuum systems, the gas that flowed into the chambers was controlled by mass flow controllers (MKS 1179A). The mass flow controllers used a variety of different mass flow rates from 100, 500, 1,000, 5,000, and 10,000 standard cubic centimeters per minutes (sccm). A four-channel flow rate readout (MKS Type 247) was utilized in order to finely control the gas flow rates for each gas mixture component. Using these controllers, it was possible to mix different gases at specific ratios in order to get a desired ratio between the sample gas and the backing gas being used.

For the hollow cathode, the different mass flow controllers used were the 500 and 100 sccm controllers. The backing gas was provided by the 500 sccm controller, while the sample gas (or gases) were provided by the 100 sccm controller(s). The difference in the flow controllers is due to the need to have a buffer gas to minimize ion destruction pathways through collisions with other ions. Therefore, the best way to do this is by having a nonreactive buffer gas like argon as the backing gas. The optimal gas ratios for production of each ion are different, thus the exact ratios between sample gas and buffer gas will be described in the individual experiments in subsequent chapters. Gas lines linking the outputs of the flow controllers allowed the gases to mix before the sample entered the hollow cathode via a 1/4" tube. The pressure in the hollow cathode was controlled by a needle valve, which limited the amount of gas entering the cell. This system is essentially a flow cell for ions and as such is used to produce simpler ions that can be readily formed and destroyed and

reformed again. This allows the discharge source to be able to form these molecules over a greater pathlength than other ion sources. The formation process will be described in detail in the next chapter.

For the supersonic expansion chamber, a pulsed valve (Parker Hannifin, Series 9 general valve, 1 mm pinhole) was used to inject gas samples into the chamber. Once again flow controllers control the ratio between the buffer gas and the sample gas in order to achieve peak ionization efficiency. A 500 sccm controller metered the buffer gas and the 100 sccm controllers metered the sample gas. The pulsed valve was controlled by using a pulsed valve driver (Parker Hannifin Iota One, 060-0010-900) and a digital delay generator (Stanford Research Systems DG645). The digital delay generator controlled the rate and duration of the pulse, while the pulse valve driver applied the voltage in order to operate the pulsed valve. The digital delay generator has additional functionality which will be discussed in subsequent sections. As the gas expanded into the chamber, it underwent a supersonic expansion. This adiabatic expansion caused the gas to cool to ~ 30 K or less depending on the backing pressure of the gas and the pressure in the vacuum chamber. In addition to dramatically decreasing the rotational temperature of the gas, as the gas expands reactions are quenched. This decreases the number of collisions that can occur, thus increasing the lifetime of unstable molecules. With the increased lifetime it is possible to produce and study unstable ions that cannot be created under normal circumstances.

2.3 Direct Absorption and Lock-In Detection

There are a number of ways to spectroscopically determine what molecules and ions are being observed. Rotational spectroscopy provides information related to the structure of the molecules, and as such is a powerful tool when identifying particular species in a complex mixture. In addition to being able to identify unknown molecules in a laboratory setting, the use of radio astronomy allows one to collect the laboratory

spectrum and then compare them to those collected by radio astronomy in order to discover if the molecules produced in the lab are also seen in space.

The most straightforward way to spectroscopically observe these molecules is by using direct absorption techniques. This is done by passing light through the gas sample, detecting the light, and directly recording the output from the detector on a computer. In order utilize this technique in the Widicus Weaver lab, the base microwave light is produced using a microwave synthesizer (Agilent Technologies, E8257D PSG with 1EA, UNU, 550, and UNT options). The light is then multiplied up in frequency to cover the range 50-1000 GHz using a VDI multiplier chain (Virginia Diodes Inc., S197(c)). From there, the light is directed into the vacuum chamber in order to interact with the sample gas. Once the light interacts with the sample gas, it is then directed and focused into a InSb hot electron bolometer (QMC Ltd., QFI/2BI). From there the output voltage is recorded using a digital oscilloscope (National Instruments, PCI-5124). The sample delivery from the pulsed valve and the trigger for data collection are controlled by a digital delay generator (Stanford Research Systems DG645) in order to synchronize the two systems to record signal while sample is present. The detailed schematic of this technique can be seen in Figure 2.5. The spectroscopic data are recorded as the synthesizer slowly steps point-by-point across frequency space.

The data are saved in three separate files: frequency, intensity and time. Using a 3-D integrator, the data are integrated over the time window in which the signal is present in order to produce the frequency domain data. This 3-D integrator program was developed in-house by Emory graduates Dr. Jacob Laas and Dr. Brian Hays. Traditionally, these peaks will face downward as the light intensity hitting the bolometer is decreasing because light is being absorbed, but because the polarity of the InSb bolometer used in these experiments was inverted, the absorption features are directed upward instead of the expected downward features. The data produced

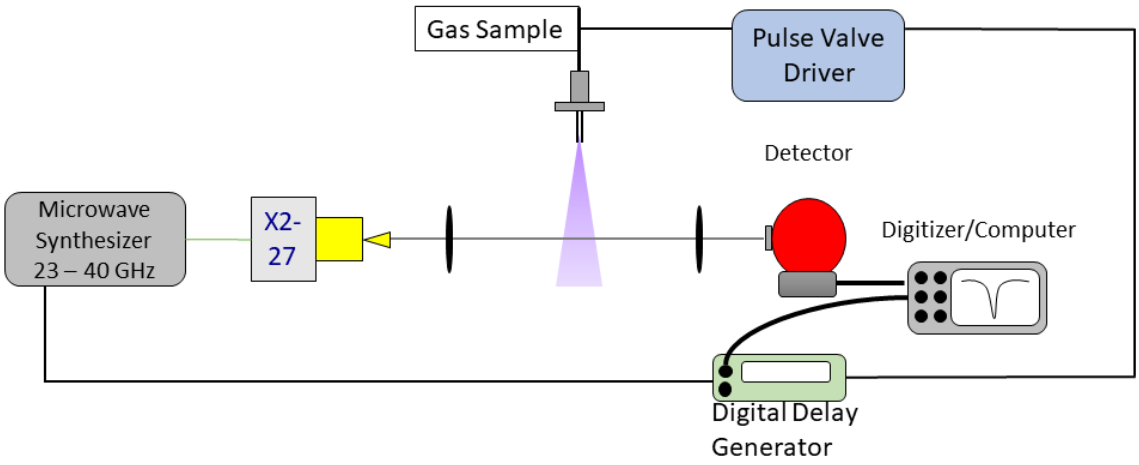

Figure 2.5: Here is the basic design for a direct absorption experiment. The synthesizer is connected to the multiplier chain which outputs its light at the sample. This light is then detected by the bolometer and the signal from there is recorded by the digital oscilloscope in the computer.

will still provide the center frequencies for each absorption feature, thus the flipped polarity is only a matter of aesthetic. For these experiments, obtaining the center frequency for the absorption feature is the primary goal. As long as the features are consistently pointed in the same direction, it is evident they are absorption features.

In comparison with direct absorption, lock-in amplification requires additional equipment and the direction of the peaks can be predetermined with equipment settings. This major difference is due to the fact that the output of the bolometer is sent to a lock-in amplifier, which provides a phase-sensitive detection technique. The equipment set-up for lock-in detection includes a microwave synthesizer (Agilent Technologies, E8257D PSG with 1EA, UNU, 550, and UNT options) used to produce the base microwave light and the modulation signal, which are mixed and then multiplied up to the THz regime using a VDI multiplier chain (Virginia Diodes Inc., S197(c)). The output of the multiplier chain is focused and directed into the vacuum chamber towards the sample. After the light interacts with the sample, it is gathered and focused into a InSb hot electron bolometer (QMC Ltd., QFI/2BI). The output of the bolometer is then routed into a lock-in amplifier (Stanford Research Systems,

Model SR 830 DSP). The modulation reference signal from the microwave synthesizer is connected to the lock-in amplifier. The lock-in processes the two signals, enhancing any signal that is in phase with the reference signal, and greatly minimizing the background noise for all others. The output from the lock-in amplifier is recorded by the computer. The schematic for lock-in detection is shown in Figure 2.6. The data are collected as the synthesizer slowly steps point-by-point across frequency space.

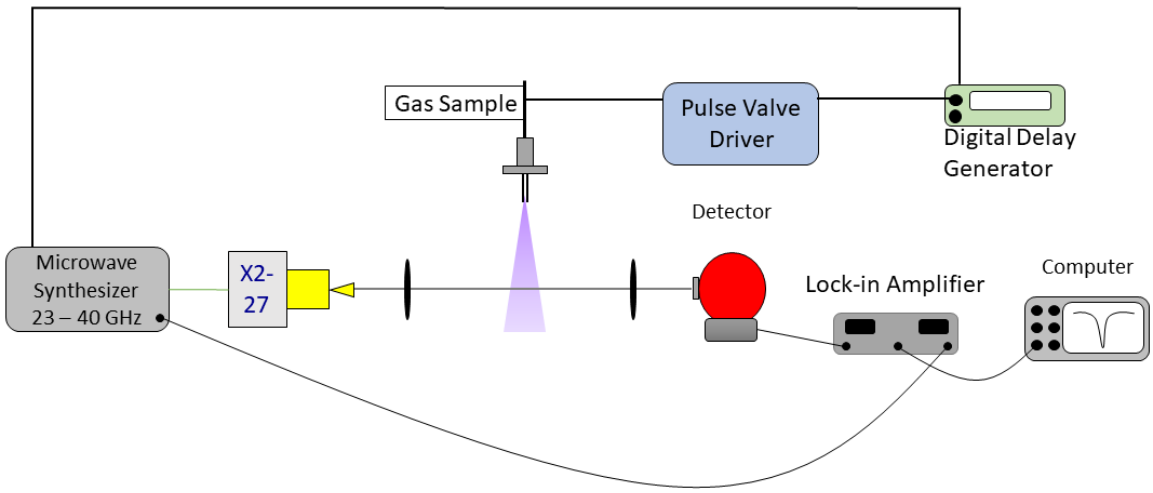

Figure 2.6: This is the instrumentation required for lock-in detection. The multiplier chain with synthesizer outputs the THz light. This light is then detected by the detector after it interacts with the sample gas. From there the signal from the detector is processed by the lock-in amplifier, which is getting the modulation reference signal from the synthesizer. Once the lock-in processes the raw data, the processed data is recorded by the computer.

The benefit to using lock-in amplification is that it greatly improves the signal-to-noise ratio in comparison to direct absorption. This is due to the fact that this is a phase-sensitive detection. This means any signal that has the same phase as the input modulation is enhanced, while any signal not in phase is averaged out. Because of this effect, the signal-to-noise ratio is vastly increased. This principle is applied when the input signal from the bolometer is mixed with the reference signal from the microwave synthesizer. This reference signal is just the modulation signal before it is mixed with the base frequency from the synthesizer. If the signal from the bolometer is in phase with the reference signal, they will constructively interfere, while signal

(or more likely noise) out of phase will destructively interfere. After the signals are mixed together, the output is passed through a low-pass filter [145].

The modulation parameters typically used in these experiments is as follows: (AM) Modulation Frequency- 15.0 kHz, Modulation Depth- 10.0 %, Time Constant- 30/10 ms, Sensitivity- adjusted as needed to optimize signal, Phase- 172 degrees, and Harmonic- 1st; (FM) Modulation Frequency- 15.0 kHz, Modulation Depth- 75.0 kHz, Time Constant- 30/10 ms, Sensitivity- adjusted as needed to see signal, Phase- 82 degrees, and Harmonic- 2nd. The 1st harmonic detection using AM is typically utilized when aligning the detector with the light source in order to maximize the transmitted light reaching the detector. In comparison, the 2nd harmonic detection using FM is used while collecting data, as it is easier to align optics using 1st harmonic detection, while it is easier to get line center information using a 2nd harmonic detection. The detection harmonic is selected if the output signal is the fundamental frequency or one of its component harmonics. When the 1st or 2nd harmonic is being detected, it is simply selecting that component of the fundamental and outputting that from the lock-in. Selecting which detection harmonic to use also results in selecting what derivative of a Gaussian lineshape the lock-in will output. A 1st harmonic detection will output the 1st derivative of a Gaussian, while a 2nd harmonic detection will output a 2nd derivative of a Gaussian. The phase is adjusted in order to maximize signal and for the peak to be pointed upwards. This is in direct contrast with direct absorption, as the direction of the peaks are due to the polarity of the bolometer.

Direct absorption and lock-in detection are two established point-by-point scanning techniques that are regularly employed in order to collect spectra in this frequency range. Despite both being point-by-point scanning techniques, the time scales on which they typically operate are very different. The direct absorption technique is limited by the response time of the detector and the acquisition rate of the data acquisition card. With the particular equipment described here, the bolometer has

the slower response time. This allows the instruments to effectively record data on sub-microsecond time scales. This is not the case with lock-in detection. The response time of the detector and the time constant of the lock-in amplifier are the limiting factors. The lowest effective time is limited by how high the modulation frequency can be set. In the case of the Stanford Research Systems Model SR 830 DSP lock-in amplifier being used in these experiments, it is limited by the detection harmonic as seen in eq. 2.5 [146].

$$\frac{102\ kHz}{DetectionHarmonic} = Mod\ Freq_{Max} \tag{2.5}$$

Because of this limitation, the fastest time scale at which a 2nd harmonic detection can run is roughly 20 microseconds, while the 1st harmonic detection can run at roughly 10 microseconds. Therefore, if a signal operating on a faster time scale is detected, it will be pulled out and broadened in time, thus shifting the center frequency of the lines. Additionally, if one is collecting data within the correct time scale, but running a pulsed experiment in which the gas pulse is on the order of a microsecond, this collection scheme will still be viable. This is because the gas will linger in the THz beam for a long enough duration before being removed by the vacuum pump. As such, lock-in detection will be able to record stable molecules or recombination products with ease. But, this method has proven ineffective in recording the spectra of short-lived unstable ions and radicals that have been the main thrust of our research goals. This selective effectiveness is due to collisions that cause the unstable products of interest to recombine into more stable molecules and radicals. Therefore, it was necessary to come up with ways to improve the time scales effective with this technique, thus improving the duty cycle, and ideally find a means to increase the speed of data collection. There has been previous work in increasing the data acquisition rate with regards to direct absorption that led to the development of fast-sweep by Dr. Brian Hays and Dr. Luyao Zou. Below I will

explain their methods and the improvements that I have made to better match these approaches with my work.

2.4 Fast-Sweep

Unlike the majority of the spectral techniques applied in the mm/submm regime, fast-sweep does not record data in a point-by-point fashion. Instead, it collects data in frequency segments, utilizing frequency modulation. Each frequency point outputted by the synthesizer is modulated with a triangle wave, resulting in a frequency sweep at each step. Thus a range of frequency points are collected with each individual data acquisition. This band of frequencies is narrower than the normal chirped-pulse methods developed by Pate and coworkers [81], but still provides a significant enhancement in data acquisition rate over traditional direct absorption. The equipment utilized in fast-sweep includes a microwave synthesizer (Agilent Technologies, E8257D PSG with 1EA, UNU, 550, and UNT options) which outputs the base microwave light with FM modulation; the light is multiplied up in frequency by a VDI multiplier chain (Virginia Diodes Inc., S197(c)). The outputted light then interacts with the sample inside of the vacuum chamber. The light is then focused onto the detector element of an InSb hot electron bolometer (QMC Ltd., QFI/2BI). The signal from the bolometer is recorded using a digital oscilloscope (National Instruments, PCI-5124). The sample delivery and data collection trigger are controller by a digital delay generator (Stanford Research Systems DG645). The schematic for fast-sweep is illustrated in Figure 2.7. Properly adjusting the trigger for data collection with the triangle wave modulation and the valve is key to effectively collecting spectra with this technique.

As stated above, fast-sweep is produced using frequency modulation in order to give the base output frequency width instead of being a discrete frequency. This modulation takes the form of a triangle wave and acts as frequency sweep, quickly going from one end of the range in frequencies to the other. One frequency sweep

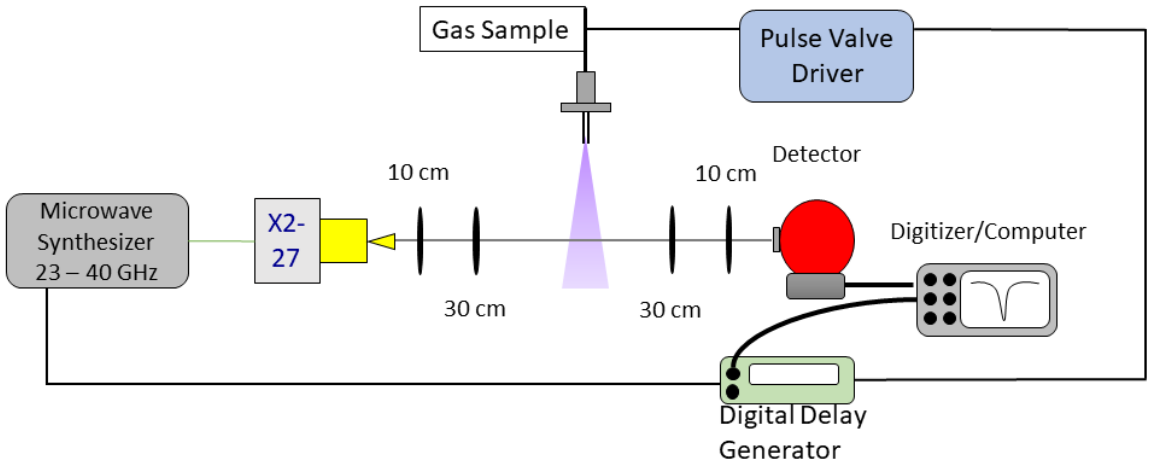

Figure 2.7: Fast sweep experimental design. The synthesizer outputs a base frequency being frequency modulated with a triangle wave. This signal is multiplied to the correct THz frequency using a multiplier chain. The THz signal is detected using an InSb hot electron bolometer. The signal from the bolometer is recorded by a digital oscilloscope on board the computer.

is a half wavelength of the triangle wave modulation. The frequency range is set by the modulation deviation and the multiplication factor of the multiplier chain being used. For example, if the modulation deviation is set to 2 MHz and the multiplication factor is six, then the bandwidth of the sweep is going to be 24 MHz. The sweep goes in both the positive and negative direction from the base frequency output. The time duration for a sweep is controlled by the modulation frequency. Increasing the modulation frequency increases the speed at which the frequency sweep occurs. When constraining the time window to have five sweeps present, a 1 kHz modulation frequency means that each data point is a microsecond in the time domain. Thus, when the modulation frequency is increased to 10 kHz each data point now marks 100 ns in the time domain.

Taking this modulation and then applying it to a dataset gives a result like that shown in Figure 2.8. The red trace shows the base FM modulation triangle wave, while the blue shows the combination of base frequency and modulation signal being detected while sample is present. Notice that the molecular signal intensity drops as a function of time as the sweep progresses. This decrease follows the pulsed valve

profile of the gas sample, allowing for the use of a simple background subtraction in order to isolate the signal from the modulation. In this instance, the foreground would be sweep one, 0-499 μs, and the background would be sweep five, 2000-2499 μs. The result of this background subtraction can be seen in Figure 2.9. The background subtraction has been automated by a python program created by Dr. Luyao Zou. We collect roughly 500 averages for reference signal so that the data processing routine can accurately perform the background subtraction. It is important to note that when the sample signal is very weak it will most likely not be visible before the background subtraction.

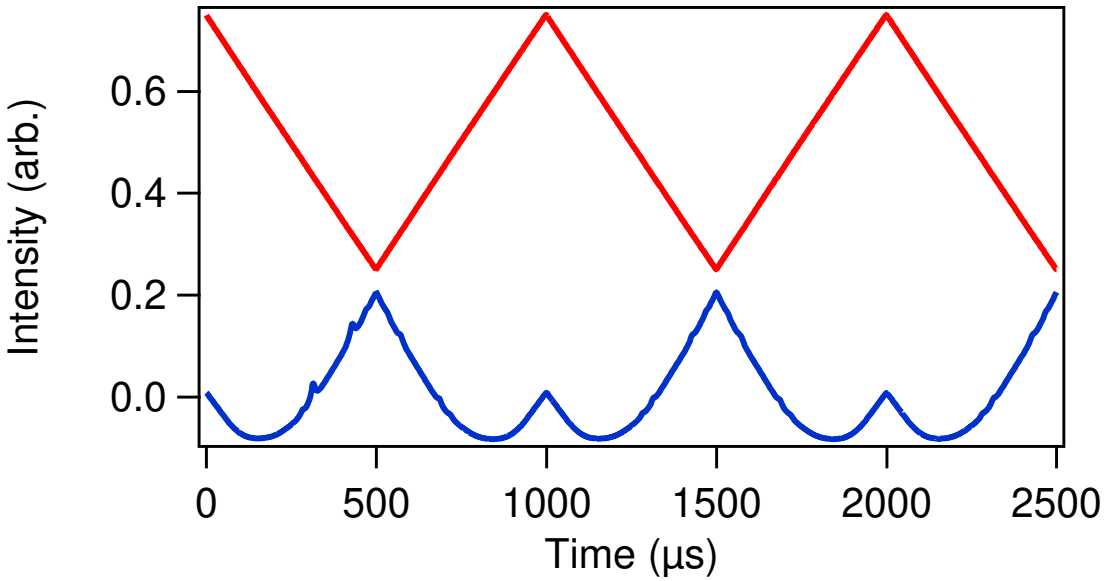

Figure 2.8: Fast Sweep Data. The red trace is the FM modulation as a triangle wave before being mixed with the base frequency from the microwave synthesizer. The blue trace is the fast-sweep output before background subtraction has occurred. It is possible to see the observed methanol signal in this trace.

Now that the basics of fast-sweep have been explained, it is pertinent to explore how it compares to the point-by-point scanning techniques that are traditionally used in this field. With lock-in detection it takes roughly one hour to record 1 GHz of spectra with a resolution of 100 kHz and no averaging. With simple direct absorption, it will take 10,000 data points to record a 1 GHz window, and if the repetition rate

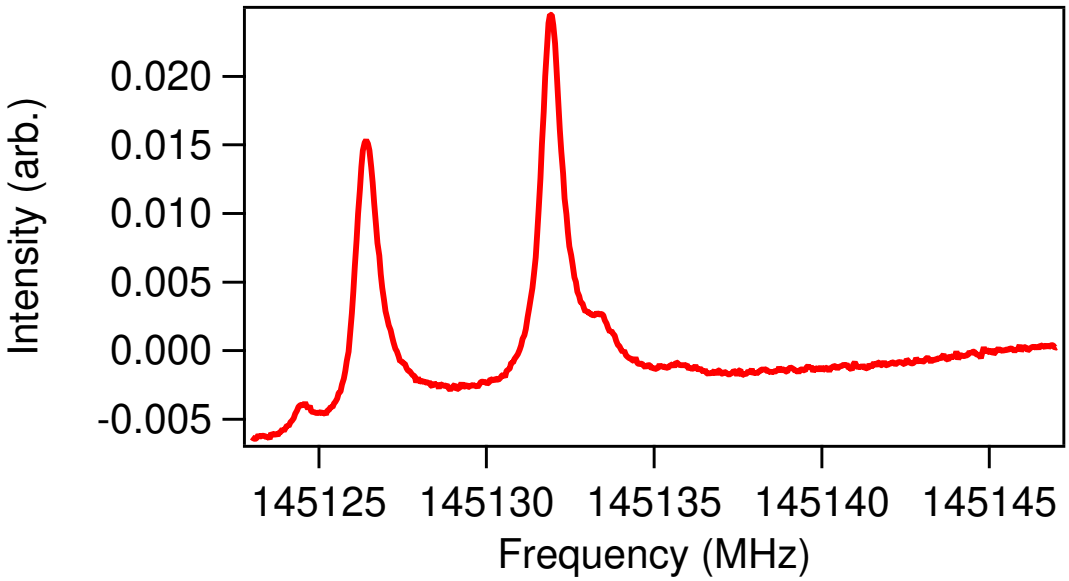

Figure 2.9: The background subtracted methanol trace. It is possible to see the two strongest methanol peaks before the background, but the two weaker methanol peaks and the Argon-Methanol signal could not be observed until the background subtract was enacted.

for the delay generator is set to 10 Hz it will take 1000 seconds or 16.667 minutes to complete that scan. This is significantly faster than lock-in detection, but only usable with stable molecules where no signal averaging is required. For unstable molecules, this approach is ineffective, and it is here that fast-sweep is extraordinarily useful. Fast-sweep can more quickly record 1 GHz of data with the same parameters defined above for direct absorption, but only requires 2 seconds of acquisition time. This occurs because the frequency sweep size will be 50 MHz and thus only 20 segments will be needed to collect the 1 GHz window. Accordingly, if the delay generator is operating at 10 Hz it will take 2 seconds to collect each segment. Therefore, this technique can effectively and rapidly record entire frequency bands worth of data with a high number of averages, making it ideal to use when searching for new unassigned lines or molecules.

Fast-sweep is significantly faster than the point-by-point scanning techniques, but it does have some drawbacks. I will be giving a general overview of these drawbacks

and practical limitations here, but for a in-depth look at this technique it would be beneficial to review the detailed analysis of the fast-sweep approach presented in Dr. Luyao Zou's thesis [147]. The main drawback associated with this technique is there can be significant deviation of the observed center frequencies of lines as a result of the nature of the technique. The frequency information is being recorded as a function of time, which is strongly influenced by the response time of the detector. The $1/e$ response time of the bolometer is approximately 500 ns, and any acquisition time approaching this limit can preclude the accurate determination of center frequencies. When the speed of the frequency sweep increases, the center frequencies will shift increasingly away from the "true" line center. This shifting also occurs when the time scale where the molecule of interest is present is very short: on the order of tens of microseconds. In order to have a full sweep present for the full duration of the molecule presence, the recording window is adjusted to focus on the time the molecule is present. The frequency of the modulation is also increased to properly scale the sweep to the correct time duration. As such, this increases the speed of the sweep which causes the center frequency of the lines to shift. This effect can also be observed when the modulation deviation is increased, leading to very large swaths of frequency being recorded at once. Typically, if the speed increases beyond 50 kHz/μs, then the center frequency will start to be shifted. Lastly, there is a frequency shift observed regardless of speed, and this shift is associated with the distance the line center frequency is from the base output frequency. This frequency shift is always present regardless of the speed of the frequency sweep and the frequency shift increases the further the line is from the center frequency of the sweep.

Despite this major draw back, there are a number of adjustments that can be made to either operationally overcome or limit the impacts of these effects. The solution for this frequency shifting problem is typically to reduce the speed of the frequency sweep. This can be done a number of ways. The simplest way to achieve this outcome

is to decrease the amount of frequency space the sweep covers or to increase the time it takes for a single frequency sweep to occur. This first approach is achieved by decreasing the modulation deviation, while the second is achieved by decreasing the modulation frequency. The first approach is an option in every instance, while the second is only constrained by the length of time over which the sample is present. The sample needs to be present for the entire length of a single sweep at a minimum. It is still possible to overcome the frequency shift even it is not possible to decrease the modulation frequency by taking the center frequency of the observed line and making that the base frequency. This overcomes the frequency shift that occurs from the observed line being away from the base frequency. This will have to be repeated a number of times until the "true" center frequency has been established. When attempting to utilize this solution, the best results are achieved when the frequency length of the sweep is 3 MHz.

Here the established data collection techniques have been detailed and the benefits of each technique have been discussed. While picking the technique that fits for the experimental circumstance is important, it is not the only parameter to considered. Another important parameter is how the generated light passes through the sample gas. This is controlled by what type of optical arrangements are used, which greatly impact signal strength.

2.5 Optical Arrangements

Before continuing into the details of the optical arrangements for the spectrometers used in these studies, it is beneficial to briefly discuss the Beer-Lambert Law. This describes how light can be absorbed by a sample, and the mathematical relationship is given by Equation 2.6. The law states that the Log_{10} ratio of the incident light intensity, I_o, and the the transmitted light intensity, I_t, is equal to the product of the molar absorptivity, ϵ, the path length, l, and the concentration of the sample, c.

The factors that can be influenced by optical arrangements are the input intensity, I_o, and the path length, l. The units for the molar absorptivity are $M^{-1}cm^{-1}$, while the pathlength is in cm, and concentration is in M. These parameters must be optimized to obtain the best signal-to-noise ratio of the sample.

$$Log_{10}\frac{I_o}{I_t} = \epsilon lc \tag{2.6}$$

Optical arrangements affect how the light being outputted from the multiplier chains is focused, directed towards the sample gas, and how much the light interacts with the sample. In the case of the experiments presented herein, there were two ways the optics were arranged: a single-pass configuration and a multi-pass configuration. As the names indicate, these two arrangements change the amount of times the light passes through the sample gas. First, it is necessary to explain how each optical arrangement functions and then go through the advantages and disadvantages of using one optical arrangement over the other.

A single-pass optical arrangement takes the light generated by the microwave synthesizer/multiplier chain system, focuses that light into a beam, and directs the light through the supersonic expansion. The benefit to this optical arrangement is in its simplicity. Since this type of arrangement utilizes the least amount of optical components, it generates the least amount of loss and therefore the greatest amount of power to reach the detector element. In accordance with the Beer-Lambert Law, as seen in Figure 2.6, this arrangement maximizes the initial intensity, but this comes at the expense of a shorter of path length.

A single-pass optical arrangement was constructed for the supersonic expansion experiments with a 10 cm focal length lens that collected the light produced from the multiplier, and a 30 cm focal length lens which focused the light into the sample. Next, another 30 cm focal length lens collected the light passing out of the sample region and directed it toward a final 10 cm focal length lens. This final lens focused

the light on to the detector element of the bolometer. This arrangement can be seen in Figure 2.10. The optical arrangement for the hollow cathode is similar to that of the supersonic expansion, but is modified in order to be optimized for the drastically increased path length as the cathode is 1.4 meters long. A 10 cm focal length lens was again used to collect the light from the multiplier. This light was then focused into the hollow cathode using a 50 cm focal length lens. Since the cathode can act as a waveguide, which helps to propagate the light down the length of the cathode, only a single 10 cm lens at the end of the cathode is used to focus the light on to the detector element. The optical arrangement with the hollow cathode can be seen in Figure 2.11. There was an attempt to install a 30 cm focal length lens on the inside of the vacuum chamber at the output of the cathode, but it was impossible to align the lens appropriately. This caused the lens to steer the beam off course and decrease the power. Lastly, having the lens so close to the hollow cathode ion source caused the cathode to plate the Teflon lens in copper. Over time this plating decreased the signal as the amount of copper on the lens built up and deflected light away from the detector element. The Teflon lenses used in all setups where from Thorlabs (LAT100, LAT300, and LAT500).

In comparison to the single pass optical approach, a multi-pass arrangement sacrifices some of the transmitted power in order to increase the path length of the light through the sample. In this configuration, the actual path length of the sample does not increase, but the effective path length of the light does. The main consideration in using this optical arrangement depends on whether the decrease in power is greater than the increase in path length. In a multi-pass optical arrangement, the light will reflect off of two mirrors, passing through the sample multiple times regardless of the frequency of light, but does not capture the light in an optical cavity. Thus, a multi-pass setup is frequency independent while an optical cavity only captures light at certain frequencies. Our setup is based on the design of Perry and coworkers [37],

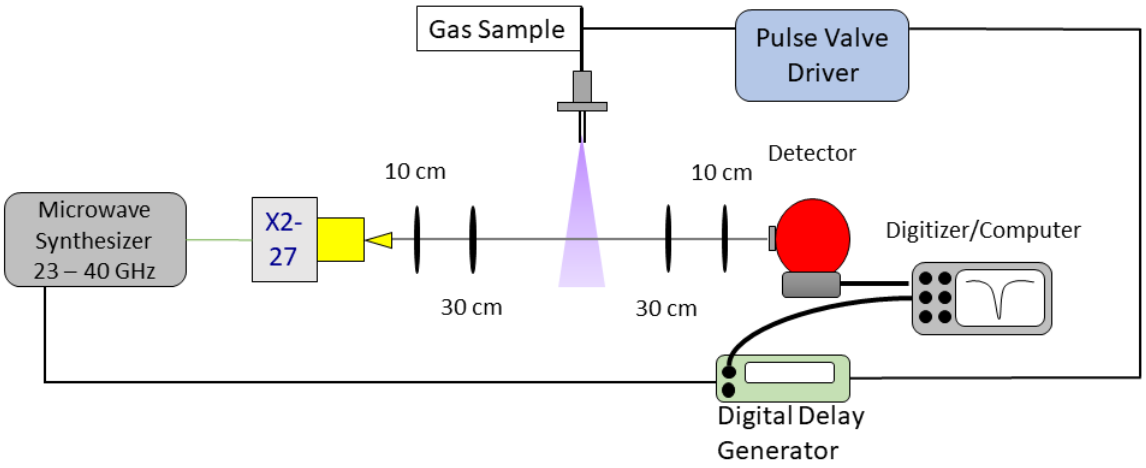

Figure 2.10: Experimental schematic for the supersonic expansion setup. Here it can be seen that the light from the multiplier chain is collected using a 10 cm focal length lens and then focused into the gas sample using a 30 cm focal length lens. Afterwards, another 30 cm lens was used to collect the light that interacted with the sample and direct it to a 10 cm lens that focused the light on to the detector element. This optical configuration is able to maximize the output power at the expense of the number of optical passes.

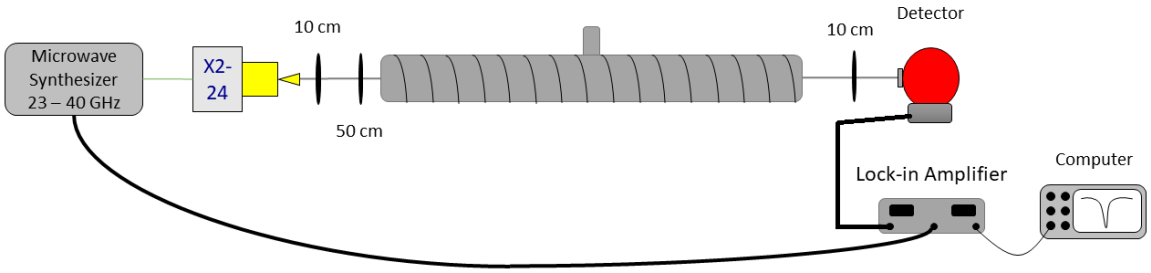

Figure 2.11: Experimental schematic for the hollow cathode setup. The light produced by the multiplier chain is collected using a 10 cm lens and then focused into the cathode using a 50 cm lens. The light that passes through the sample is then collected and focused into the bolometer using a single 10 cm lens.

which is in turn based on the Herriott cell design [38]. The difference between these two arrangements is whether the light is inputted into the system through a hole in one mirror, as in the case of a Herriott Cell, or whether it is instead inputted into the system by passing near the edge of one of the mirrors at a steep angle. The latter is much better for work in the mm/submm regime, where the beam waist is often quite large and machining an appropriate hole in the mirror is unfeasible.

Our multi-pass optical arrangement was only employed for the supersonic expansion experiments and was set up in the following way: a 50 cm lens was used to collect the outputted light and focus the light onto a set of spherical mirrors (Edmund Optics, 15.24 cm diameter and 15.24 cm focal length, NT32-836) that formed a seven-pass optical arrangement. This multi-pass configuration was centered under the pulse valve and was optimized to have as many effective passes through the sample as possible. This allows the sample to be perpendicular to the mirrors, which protected them from the discharge source. The effective increase in pathlength was a factor of $\sim$5.5. The effective path length is limited to this amount because of the intrinsic size of the THz beam which limits how many passes can fit onto the mirrors without any loss of light, and by how many passes can effectively interact with the supersonic expansion. This optical arrangement could not be applied to the hollow cathode because the vacuum chamber holding the cathode was not large enough to accommodate the mirrors necessary to form a multi-pass arrangement. Additionally, because of how the discharge source produced ions, it would direct the ions towards the mirrors. This puts the mirrors at risk of being damaged by the discharge, and thus over time would require replacement. In the end, a multi-pass arrangement was the best possible optical arrangement for the supersonic expansion experiments, while a single-pass arrangement was the only viable option for the hollow cathode discharge source.

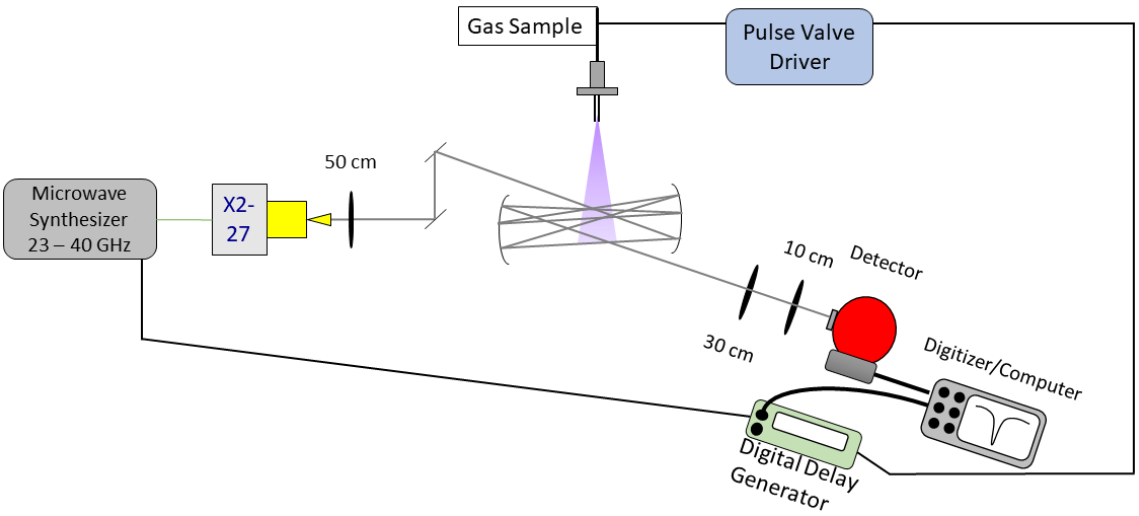

Figure 2.12: Schematic for the multi-pass spectrometer used to study discharge products with the supersonic expansion. The light provided by the multiplier chain was collected using a 50 cm lens and then focused onto the multi-pass mirrors. These two mirrors were arranged to allow seven passes before the light left the multi-pass. Once the light left the multi-pass, it was collected by a 30 cm lens and then focused onto the detector element using a 10 cm lens. This optical arrangement maximizes the path length that the light interacts with the sample at the expense of the output power reaching the detector.

Chapter 3 Developments in Instrumentation

With the goal of detecting and assigning the spectra of highly fluxional molecules and ions, it is necessary to develop new instrumentation techniques that will improve sensitivity, data acquisition rates, and the assignment of complex spectra. To achieve these instrumentation goals a number of different techniques were developed, such as pulsed valve triggered lock-in detection, lock-in fast-sweep, microwave-millimeter/submillimeter double resonance, and cavity enhanced detection. In the following sections, the benefits, limitations, and future directions of each of these techniques will be discussed.

3.1 Pulsed Valve Triggered Lock-in Detection

The first major development of new instrumentation and spectroscopic techniques was pulsed valve triggered lock-in detection (PVTLI). This technique was developed in order to more effectively sample pulsed discharge products with lock-in detection. As stated in the previous chapter, lock-in detection is a sensitive detection technique, but has the major drawback of having to operate on the tens of microseconds scale. This is on average an order of magnitude slower than the operation of the pulsed valve. Therefore, the duty cycle of lock-in detection when coupled with the pulsed valve is roughly 10% at peak efficiency, meaning the majority of the scan is averaging noise instead of signal. This dramatically impacts the detection of short-lived unstable ions and radicals, and can also lead to misleading detections. The misleading detections primarily come in the form of decomposition products from the unstable discharge products. Thus, when recording data on a longer time scale, the lines produced by the decomposition products will have increased intensity from what is actually in the

expansion while the unstable products are still present.

The initial solution for this problem was to attempt double lock-in detection. This technique has been previously implemented for the methoxy radical [148]. While successful at providing a means to utilize lock-in detection for a pulsed experiment, double lock-in detection requires the use of two lock-in amplifiers. The first was locked to the modulation in the signal and the second one was locked to the pulsed valve trigger signal. The signal must be processed this way as the input to the first lock-in is run through a low-pass filter, thus the higher frequency locked signal has to be processed first. For the experiment that produced the methoxy radical, the pulse valve repetition rate was set to 18 Hz, while the modulation frequency was set to 15 kHz. Thus, while this technique effectively increases the duty cycle, it requires more equipment and precise processing of information before usable data can be collected.

In order to decrease the amount of equipment used and streamline data processing, pulsed valve trigger lock-in detection was developed. This technique utilizes the equipment currently available for lock-in detection and direct absorption without any need for an additional lock-in. The equipment set-up for lock-in detection is as follows: the microwave synthesizer (Agilent Technologies, E8257D PSG with 1EA, UNU, 550, and UNT options) produces microwave light with frequency modulation, which is multiplied up into the THz regime using a VDI multiplier chain (Virginia Diodes Inc., S197(c)). The output is focused using a Teflon lens onto the sample. After interacting with the sample, the light is gathered and focused into the InSb hot electron bolometer (QMC Ltd., QFI/2BI). The output of the bolometer is then routed into a lock-in amplifier (Stanford Research Systems, Model SR 830 DSP), and then processed signal from the lock-in is collected using a digital oscilloscope (National Instruments, PCI-5124). Again, the gas pulse and data collection are triggered using a digital delay generator (Stanford Research Systems DG645). The full diagram is found in Figure 3.1. This technique collects data by stepping point-by-point across

frequency space.

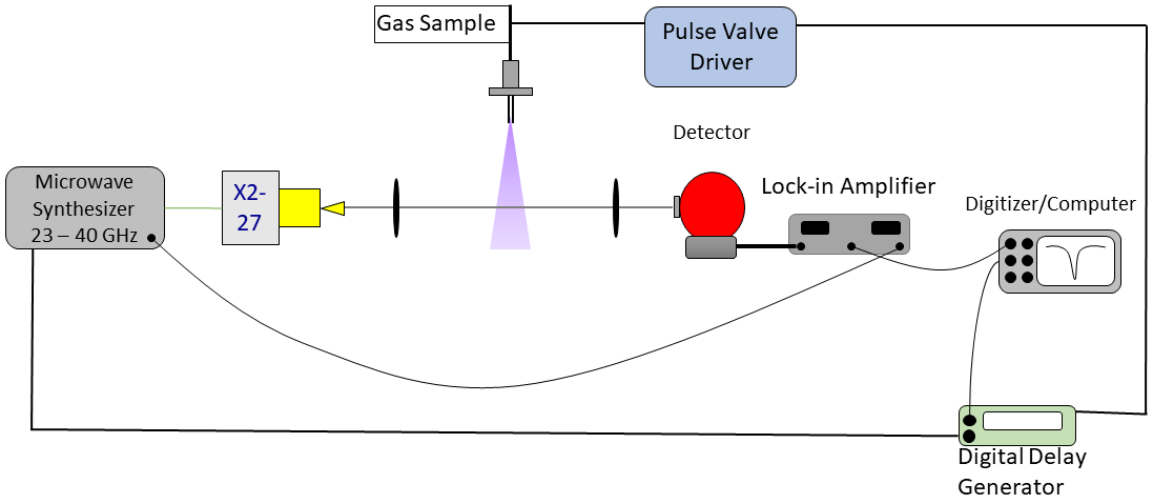

Figure 3.1: This is the detailed schematic for the pulsed valve trigger lock-in detection. The base frequency with frequency modulation is produced by the synthesizer and multiplied up in frequency by the multiplier chain. After interacting with the sample, the light is detected by the bolometer. The output from the bolometer is then connected to a lock-in amplifier. Additionally, the modulation reference signal is connected to the lock-in amplifier. With the reference signal, the lock-in amplifier is able to process the signal coming from the bolometer and output the processed signal to the computer. This processed signal is then recorded by a digital oscilloscope in the computer.

In order for this technique to work, the time constant needs to be adjusted slightly from what was previously stated for lock-in detection. Since the time scale of data acquisition using PVTLI is about two orders of magnitude shorter than normal lock-in detection, the time constant needs to be decreased and the frequency modulation increased. The increased frequency modulation is used to limit the data being broadened in time due to the time constant still being too slow. The modulation parameters used for this technique are as follows for FM modulation: (FM) Modulation Frequency- 50.0 kHz, Modulation Depth- 75.0 kHz, Time Constant- 100 μs, Sensitivity- adjusted as needed to see signal, Phase- 63 degrees, and Harmonic- 2nd. If the time constant is too high, the data will be dramatically distorted in time causing the intensity signal to be flat. To center data in the time domain, the trigger for data collection on the delay generator is adjusted to collect the data properly. Too

short of a time constant will cause the detection of random noise as the lock-in is not able to process the data.

Once data are collected, they are processed using the 3-D integrator program used to process direct absorption data. Here, raw data will be displayed as shown in Figure 3.2. Despite decreasing the time constant from 10/30 ms down to 100 μs, data will still be shifted in time. Since data are collected in a point-by-point fashion, this shifting in time will not impact processed data as the time over which the signal is integrated is manually selected as seen in Figure 3.3. Thus, while a 100 μs is ideal, it is also possible to use 300 μs as a time constant. While using the slower time constant is possible, there it requires the delay generator to record data far later in time as the signal is significantly spread out in time. The adjustment of the collection trigger timing to a few hundred milliseconds delay from the gas pulse will typically center lock-in data.

The goal of this technique was to increase the duty cycle with regards to pulsed experiments that need the sensitivity of a lock-in detection, but as with direct absorption and normal lock-in detection, this is a point-by-point scanning technique. This technique is slightly faster than normal lock-in detection because the data collection rate is determined by the repetition rate of the pulsed valve, thus delivering increased speed and sensitivity when compared to normal lock-in detection. However, in comparison with the data acquisition speed of fast-sweep, it is still fairly slow. Thus the next logical step would be to attempt to merge this technique with fast-sweep in order to record large swathes of frequency at a time instead of the point-by-point method that was established here.

3.2 Lock-In Fast-Sweep

The goal for the lock-in fast-sweep, LIFS, detection of to combine the sensitivity of a phase-sensitive detection with the increased data acquisition rate that is provided

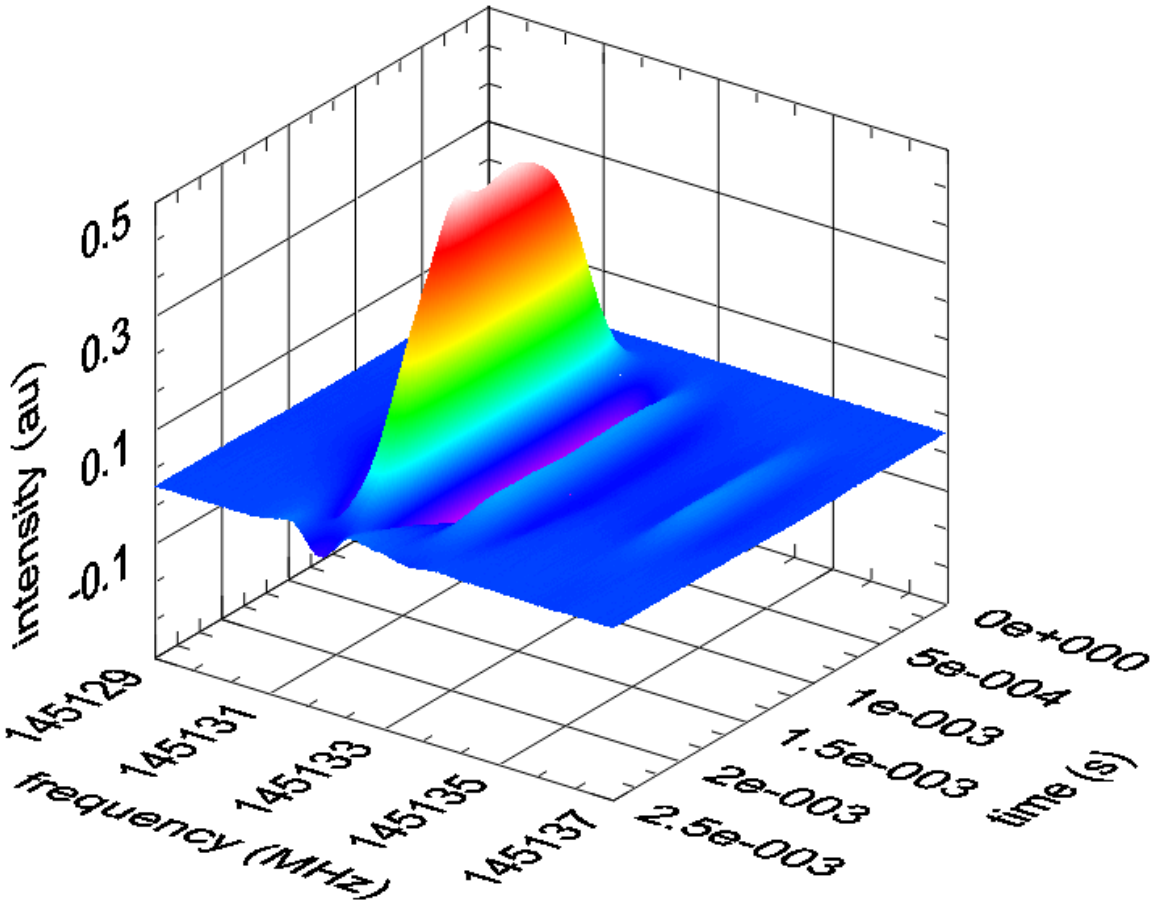

Figure 3.2: The three dimensions of a PVTLI scan. The time axis is in seconds, the frequency axis is in MHz and the intensity axis is arbitrary. Integrating over time will produce a intensity vs. frequency figure showing the spectral data in that time window.

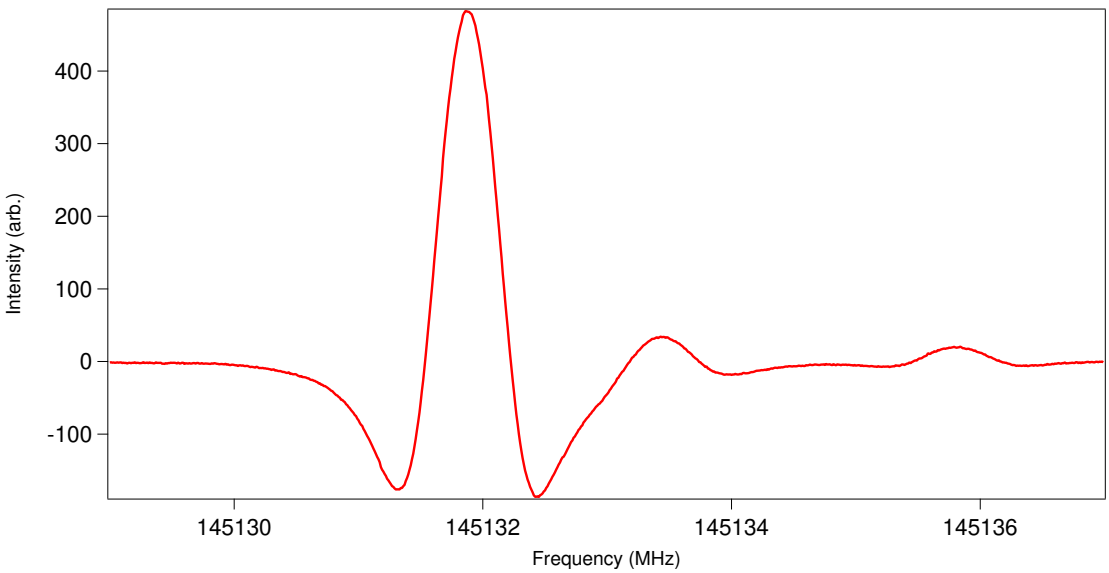

Figure 3.3: A processed PVTLI scan for methanol. The frequency axis is in MHz and the intensity axis is arbitrary.

by utilizing fast-sweep. This technique would be an upgrade from the fast-sweep technique that was developed by Dr. Brian Hayes and Dr. Luyao Zou [34, 36]. The two main upgrades to the technique would be to switch the triangle wave frequency modulation (FM) from the microwave synthesizer, used to increase the bandwidth, to an arbitrary waveform generator that can output a frequency sweep; and to change the frequency modulation to a sine wave and use lock-in detection to detect that wave as the signal sweeps across frequency space. The schematic for the experiment can be seen below in Fig. 3.4. The output microwave signal from the microwave synthesizer (Agilent Technologies, E8257D PSG with 1EA, UNU, 550, and UNT options) is mixed with a frequency sweep from an arbitrary waveform generator (AWG, Agilent M8190A). This frequency sweep goes from some frequency X to X+Y and then sweeps back down from X+Y to X. A single frequency sweep will be defined as a single positive (X to X+Y) or negative (X+Y to X) frequency ramp or a half wavelength of the triangle wave to directly compare it to fast-sweep.

The base output of the synthesizer and this frequency sweep are mixed using a mixer (Miteq, DM0520LW1) and then passed through a band pass filter (Lorch, 13IZ6-

11650/5100-S for methanol), a microwave pre-amplifier (ASL-182010), another band pass filter (Lorch, 13IZ6-11650/5100-S), a frequency doubler (Wright Technologies ATX26-220), a final band pass filter (Lorch, 13IZ6-11650/5100-S), and then the signal is attenuated to 0 dBm with microwave attenuators (Mini-Circuits) in order to enter the VDI multiplier chain (Virginia Diodes Inc., S197(c)) without damaging them. The light then entered a seven-pass optical set-up with spherical mirrors (Edmund Optics, 15.24 cm diameter and 15.24 cm focal length, NT32-836). The methanol sample (Fisher Scientific 99.9%) enters into the chamber using a pulsed valve (Parker Hannifin, Series 9 general valve, 1 mm pinhole), centered to maximize the number of optical passes with which it interacts in order to increase signal strength, with an argon backing gas (Nexair, ultra-high purity) at a pressure of 250 PSIG and a 10 Hz repetition rate. After the light interacts with the sample, it is detected with an InSb hot electron bolometer (QMC Ltd., QFI/2BI) and data were then recorded using a digital oscilloscope (National Instruments, PCI-5124). The AWG output was synchronized with the trigger for data acquisition. This allows for the start of the sweep to be properly timed in order to acquire the entire frequency sweep and accurately process data.

The output of the microwave synthesizer was set to 8000 MHz and the AWG would sweep from 4093.65 MHz to 4095.65 MHz. When mixed together and doubled and then sent to the band 5 multiplier, which is a $\times 6$ multiplier, the resultant frequency range is 145123.8 MHz to 145147.8 MHz. This frequency range covers a number of strong methanol lines. A proof of concept experiment was then run where methanol was mixed with an argon backing gas and the methanol lines were then detected using LIFS.

The initial parameters for the lock-in detection were set to a modulation rate of 15 kHz, a modulation deviation of 37.5 kHz and a time constant of 300 μs. These parameters for the lock-in were thought to be a useful starting point as they are the

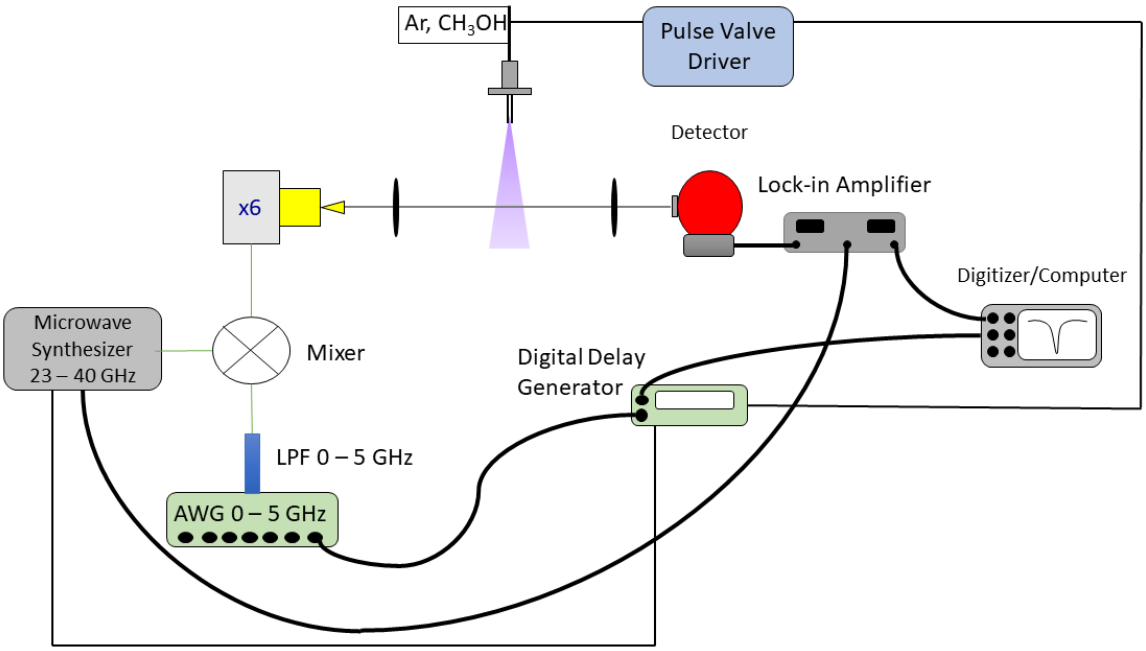

Figure 3.4: The schematic diagram for lock-in fast sweep.

parameters used for pulsed valve triggered lock-in detection. The initial frequency sweeps were only positive ramps from 4093.65 MHz to 4095.65 MHz. The first major problem with this approach was having only positive ramps caused major fluctuation in our signal. This was fixed by having the frequency sweep ramp in a positive direction and then ramp in the negative direction. This allows the AWG to gently sweep in both directions instead of having a hard reset back to its start frequency. This prevents the sudden frequency shift back, which provides spectra without large RF noise affecting the quality of the signal.

Once this source of RF noise was addressed, the next problem was with a lack of signal. This was very odd, because if the FM modulation was turned off and the output of the bolometer was directly recorded, it was possible to record a fast-sweep signal using this equipment and detect methanol this way. It was determined that the sweep was just too fast for the lock-in amplifier to detect. In order to address this the modulation rate was increased, while the time constant was decreased. In addition to those changes, the sweep rate was decreased from 24 MHz per 500 μs to

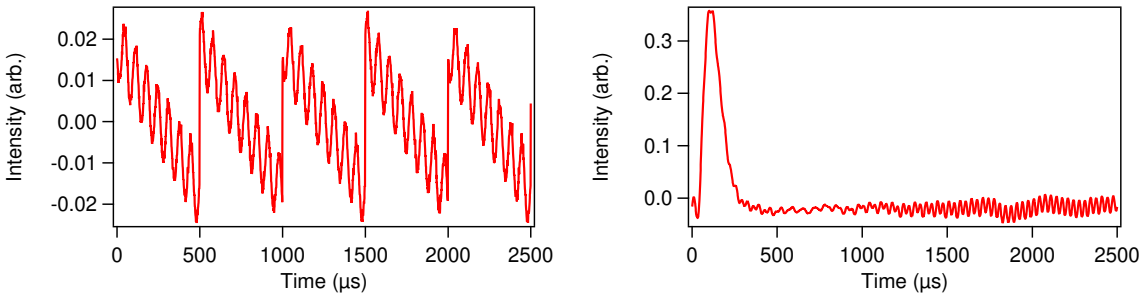

Figure 3.5: On the left, all sweeps are going in the same direction. This causes large RF noise because the hard restart of the frequency sweeps interferes with the spectrum as shown on the right. This causes part of the data to have the RF super imposed on the usable data and thus effectively washes out any signal in the first part of the sweep. The RF is caused by the jitter in the electronic components that generate the microwave frequencies.

3 MHz per 2500 μs. These changes successfully allowed for the detection of methanol using LIFS. The modulation settings used for this detection are a modulation rate of 50 kHz, a modulation deviation of 37.5 MHz, and a time constant of 30 μs.

This detection is not perfect, as the lock-in amplifier is too slow to handle both the frequency sweep and the modulation at the same time. This causes the detection to be stretched in time. This stretching also occurs for pulsed valve trigger lock-in detection, but since a 3-D integrator is used to produce the final frequency domain data this effect does not matter as the signal is integrated over time. This is not the case for LIFS. Since the frequency sweep is also a function of time, this stretching causes the methanol signal to be shifted in frequency. This means that it is possible to detect the signal using this technique and get a high number of lock-in averages quickly, but the center frequency for those detected lines will be off the center frequency as seen in Figure 3.6.

The frequency shift arises because of a limitation with the equipment currently available in this laboratory. The current lock-in amplifier can only detect modulation rates up to 102 kHz per detection harmonic. That means for a second harmonic detection it can only detect up to 51 kHz modulation rates, such that the lowest time constant resulting in a detectable signal is 30 μs. In order to successfully detect a LIFS

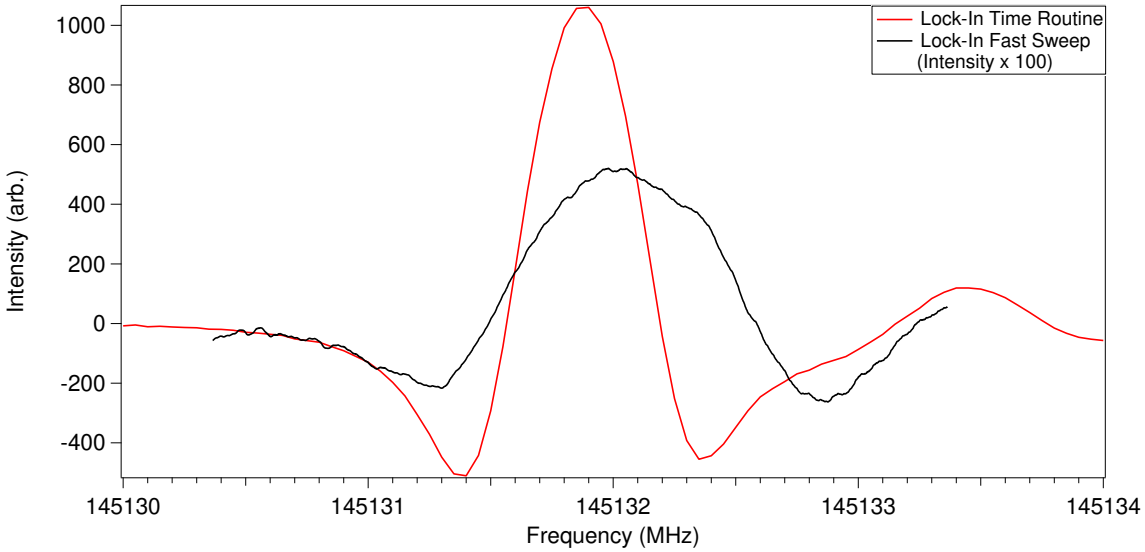

Figure 3.6: The effects of a slow lock-in amplifier using LIFS. The red trace is a pulsed valve triggered lock-in detection of the 145131.864 MHz methanol line. The same line was recorded using Lock-in fast-sweep is displayed by the black trace. As it can be clearly seen, the black trace is broadened in time as well as frequency, because the lock-in amplifier is not able to process the data on the correct time scale in order to properly record the data with the correct center frequency. As a note, the lock-in fast-sweep signal is two orders of magnitude lower in intensity as the PVTLI signal when collected using the same lock-in amplifier parameters.

signal the lowest time constant has to be used that is not faster than the modulation rate. That means the time constant cannot be faster than 1/51 kHz ($\sim$ 20 μs). This effectively limits the best usable time constant to 30 μs. The lock-in is not fast enough to effectively process data because it is contending with both the modulation and the frequency sweep, so it does not fully process the modulation and this modulation shows up as a sine wave in processed data. This also may be a problem that is fundamental to LIFS as the lock-in is attempting to process the frequency sweep and the modulation; the lock-in is attempting to lock to the modulation, but because the frequency sweep is occurring at the same time as the modulation the lock-in does not have enough time to fully process the modulation. This leads to the majority of the sine wave being removed, but leaves some of the modulation present in the processed data as shown in Fig. 3.6.

The data processing for this approach is similar to fast-sweep, but slightly different because it is not possible to have a foreground and background sweep in the same scan. That is because the frequency sweep had to be dramatically slowed in order to have the lock-in be able to process the frequency sweep and modulation effectively. As previously discussed, the frequency sweep is still too fast for the lock-in to handle and thus the sine wave is not fully removed from the scans. Therefore, both a foreground and background scan must be taken separately and the background must be subtracted manually. This means the background subtraction program that was developed to process fast-sweep data will have to be modified in order to process the LIFS data. This modification may become unnecessary with the purchase of more effective equipment.

The way forward for this technique is simple: A new lock-in amplifier is needed that has a lower time constant and can detect a second harmonic signal at a higher modulation rate than is currently possible with the equipment used in this experiment. In addition to a faster lock-in amplifier, it would also be possible to run this

experiment using a direct digital synthesizer card (DDS). The DDS is a much cheaper alternative to an AWG and still produce the frequency sweeps required to run this experiment. With the upgrade of the lock-in amplifier and the purchase of either an AWG or DDS it will be possible to quickly average lock-in scans together and significantly increase the SNR of detected lines. The last important factor to note is that this technique currently requires a detector that can process data with a relatively fast modulation frequency. For instance, in the Widicus Weaver lab there are two different bolometers; one has an InSb semiconductor and the other has a niobium semiconductor. Both that can be used to detect a LIFS signal, but only one will be able to successfully do so. The reason for this is that the niobium based bolometer has a reduced response as the modulation frequency increases past 200 Hz and essentially is blind to the light when the modulation is past 3 kHz. With it being necessary for LIFS to operate with a modulation frequency well about 50 kHz, it can only operate with the InSb based bolometer as that is capable of responding to light with such a high frequency modulation. Therefore, it is necessary to determine four things for this technique to work: How the base frequency, the frequency sweep, and the modulation will be produced; if the detector is fast enough record the outputted light; if the lock-in amplifier can process a second harmonic detection with a modulation frequency above 50 kHz; and if it is possible to use a data acquisition card fast enough to capture these data. Given the limitations with the equipment available in our lab, my work moved on from LIFS to focus on other possibilities for simplifying assignment of complex spectra.

3.3 Microwave-Millimeter/Submillimeter Double-Resonance

This subchapter, with minor adjustment, is reprinted with permission from K. M Roenitz, B. M. Hays, C. R. Powers, M. N. McCabe, H. Smith, S. L. Widicus Weaver,

One useful approach for making spectral assignments in a complex spectrum as is expected for fluxional ions is to use double-resonance techniques to confirm line assignments. Here two colors of light are used, one to drive a particular transition, and another to drive population out of one of the associated energy levels by driving a different but connected transition. We implemented the first test of microwave-millimeter/submillimeter double-resonance spectroscopy. The experimental design for the microwave-millimeter/submillimeter wave double-resonance experiment can be seen in Figure 3.7. The microwave-millimeter/submillimeter wave double-resonance experiment was conducted using a supersonic expansion created using a pulsed valve (Parker Hannifin, Series 9 general valve, 1 mm pinhole) which flowed Argon gas (Nexair, ultra-high purity) bubbled at 20 psig through liquid methanol (Fisher Scientific 99.9%). The pulsed valve ran at a repetition rate of 10 Hz for all experiments. Below the pulsed valve was a set of spherical mirrors (Edmund Optics, 15.24 cm diameter and 15.24 cm focal length, NT32-836) that formed a seven-pass optical cavity of millimeter/submillimeter radiation; this optical cavity probed the expansion approximately 6 cm from the pinhole of the valve. The millimeter/submillimeter radiation was produced using a signal generator (Agilent Technologies, E8257D PSG with 1EA, UNU, 550, and UNT options) and then multiplied to the appropriate probe frequency in the range of 50 GHz to 1 THz using a frequency multiplier chain (Virginia Diodes Inc., S197(c)). For the experiments conducted, the frequency range and power were 140-230 GHz and 0.5-4 mW, respectively. An InSb hot electron bolometer (QMC Ltd., QFI/2BI) was used as the detector for the millimeter/submillimeter beam. The output signal from the detector was recorded using a digital oscilloscope (National Instruments, PCI-5124).

For the double-resonance experiments, a microwave waveguide horn was mounted

below the pulsed valve and aimed at the aperture so that the entire expansion interacted with the radiation. The microwave light was produced using an arbitrary waveform generator (AWG, Agilent M8190A). The AWG output was filtered by a 0 – 5 GHz lowpass filter (Lorch, 8LA-5000-S) and combined with the +10 dBm local oscillator signal from a microwave synthesizer (Hittite, HMC-T2100) in a double-balanced mixer (Miteq, DM0520LW1). The resulting upconverted chirped pulse was then passed through a pre-amplification stage (Wright Technologies, ASL-182010), filtered by a bandpass filter (Lorch, 13IZ6-11650/5100-S for methanol), and subsequently attenuated using combinations of 3, 6, and 10 dB fixed attenuators (Mini-Circuits). The exact configuration of the attenuators varied depending on the experiment. The output was amplified with a 10 W solid state amplifier (Microwave Power, L0618-40-T526).

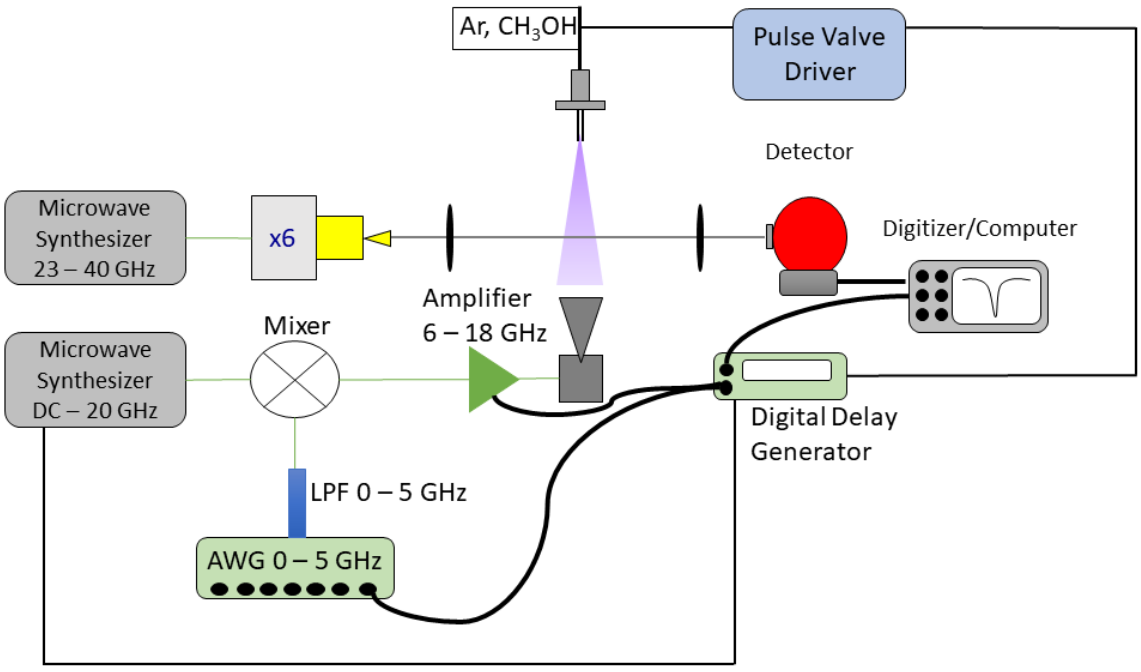

Figure 3.7: The schematic diagram of the double resonance experimental setup. The mixer component includes the double-balanced mixer, the pre-amp, the bandpass filters, and the attenuators.

Two methods were used to record the double-resonance spectra: the first method

held the millimeter/submillimeter light at a constant frequency (on- or off- resonance) while the microwave radiation was chirped across a band centered on the frequency of the resonant microwave transition. This method yielded a time trace of millimeter/submillimeter absorption signal at a fixed frequency while the microwave radiation frequency was changing as a function of time during the chirped pulse. The second method involved holding the microwave light on the resonant frequency while the millimeter/submillimeter light was scanned across a 24 MHz wide window using the fast-sweep method developed previously [36]. This fast-sweep method was adapted from a fast scan submillimeter spectroscopic technique (FASSST) which was developed by the De Lucia group [32]. This technique was later applied to a pulsed supersonic jet to study van der Waals complexes [33]. For a thorough review on the development of the sweep technique being utilized currently see Zou et al. [36]. Spectra were collected at various levels of microwave attenuation (0, 3, 6, 10, 13, 16, and 20 dB). The recorded spectra from this second approach were taken in the frequency domain. All spectra produced by both methods were averaged for 400 cycles.

The transitions that were probed for the double-resonance experiments for methanol are listed in Table 3.1.

Table 3.1: Transition frequencies of methanol used in the double-resonance experiments (in MHz)[102]

Methanol Transition	Catalog Freq.	Uncertainty
$2_{00} - 3_{-10}$	12178.584	0.012
$3_{00} - 2_{00}$	145093.754	0.003
$3_{-10} - 2_{-10}$	145097.435	0.003
$3_{00} - 3_{-10}$	157272.338	0.012
$2_{00} - 2_{-10}$	157276.019	0.012
$2_{10} - 2_{00}$	165061.130	0.005
$4_{-10} - 3_{-10}$	193441.600	0.004
$1_{10} - 0_{00}$	213427.061	0.006

The first part of the experiment was designed to test if a double-resonance signal could be detected when the millimeter/submillimeter line center was held constant,

while the microwave chirp was centered on a resonant transition. Figures 3.8, 3.9, and 3.10 show the methanol absorption response signal at the millimeter/submillimeter frequency; the overall lineshape of the signal is due to the dynamics of the pulsed valve. The timing of the resonant frequency can easily be determined by knowing the starting frequency, length of the chirped pulse, and its sweep rate. For methanol, the microwave chirp center was set to 12178.584 MHz; the recorded spectrum using a 100 MHz wide chirp at a rate of 0.2 MHz/μs is shown in Figure 3.8. The double-resonance signal can be clearly seen while the microwave chirp is on, and is no longer present when the microwave chirp is turned off. The next test was to record the spectral response when the microwave signal was on resonance, and then compare that to the response when the microwave signal was tuned to a frequency $\sim$150 MHz off resonance. The microwave chirp was slightly altered to better show the double-resonance signal by decreasing the chirp width to 10 MHz and the sweep rate to 0.02 MHz/μs. The results of this test are seen in Figure 3.9; as expected no double-resonance signal is observed when the microwave is tuned off resonance. The final test for this set of experiments was to shift the millimeter/submillimeter line center from 193441.600 MHz to the non-resonant frequency of 213427.061 MHz, while keeping the microwave frequency centered at 12178.584 MHz. The recorded spectra, seen in Figure 3.10, do not show a double-resonance signal, as expected. This is because the monitored millimeter/submillimeter transition does not have any states that overlap with the microwave transition. With these three measurements, it is clear that the spectra are displaying the double-resonance effect, since the downward peaks disappear when the microwave radiation is turned off, when the microwave chirp center frequency is shifted by $\sim$150 MHz, and when the millimeter/submillimeter light is tuned to a non-resonant frequency.

At this point, the question arose as to why all the double-resonance signals point in the same (downward) direction. It was anticipated that the double-resonance signal

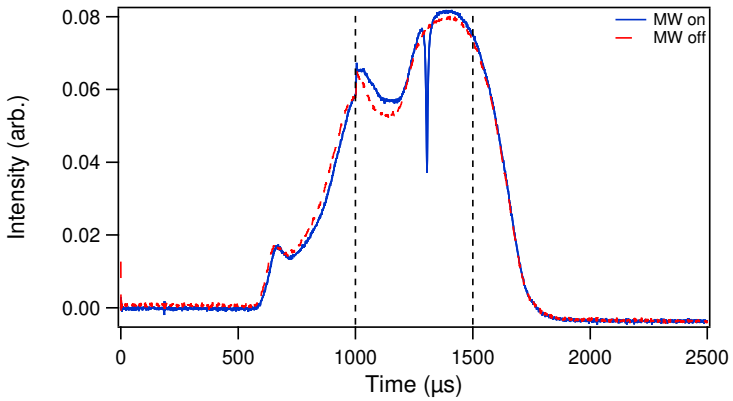

Figure 3.8: Methanol absorption signal for the 4_{-10} - 3_{-10} transition at 193,441.600 MHz with (blue) and without (red) the microwave pump. The sharp dip in the signal occurs when the instantaneous frequency of the microwave chirped pulse was on resonance at 12,178.584 MHz, corresponding to the connecting 2_{00} - 3_{-10} transition. The width and sweep rate for the microwave chirped pulse are 100 MHz and 0.2 MHz/μs, respectively. The black, vertical dashed lines represent the start and stop time for the microwave chirped pulse.

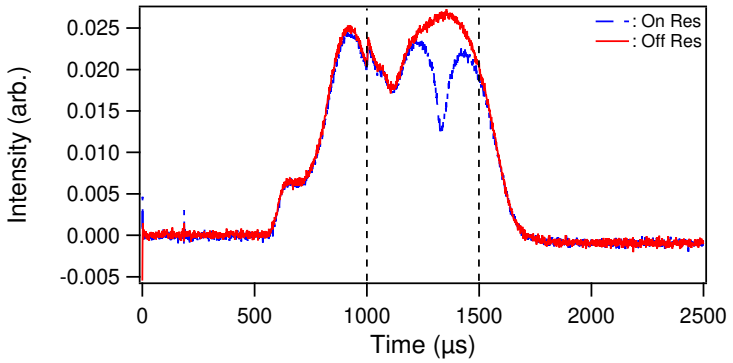

Figure 3.9: Methanol absorption signal for the 4_{-10} - 3_{-10} transition at 193,441.600 MHz with the microwave pump tuned on (blue) and off (red) resonance. The center frequency of the microwave chirped pulse was 12,178.584 MHz for the on-resonance trace, corresponding to the connecting 2_{00} - 3_{-10} transition; and 12,026.961 MHz for the off-resonance trace, where no methanol transitions are found. The width and sweep rate for the microwave chirped pulse are 10 MHz and 0.02 MHz/μs, respectively. The black, vertical dashed lines are placed at the start and stop time for the microwave chirped pulse.

direction would be level-dependent: If the connecting transition moved population from the lower state, the signal would decrease; if the connecting transition moved population into the lower state, the signal would increase. However, we saw no relationship between the level connectivity and the directionality of the signal. The

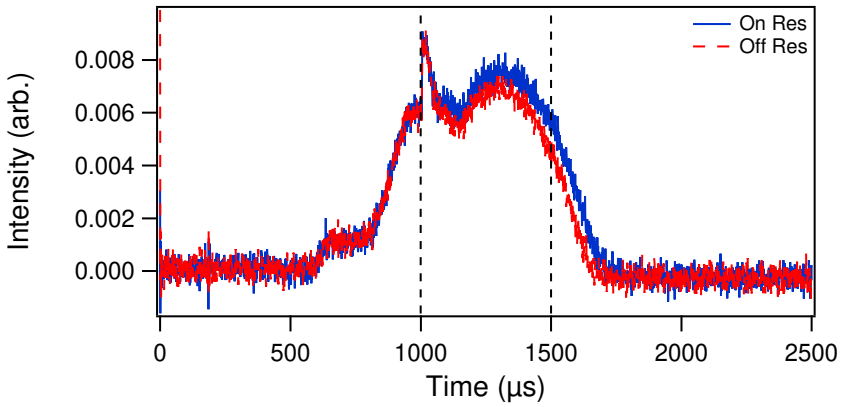

Figure 3.10: The non-resonant methanol absorption signal for the 1_{10} - 0_{00} transition at 213,427.061 MHz with the microwave pump either on the resonant 2_{00} - 3_{-10} transition at 12,178.584 MHz, or on the non-resonant frequency of 12,078.000 MHz. The on (blue) and off (red) resonant signals are displayed. No double-resonance signal is observed, as expected since the pump radiation did not connect to any resonant transitions. The black, vertical dashed lines are located at the start and stop time for the microwave chirped pulse. The width and sweep rate for the microwave chirped pulse are 100 MHz and 0.2 MHz/μs, respectively.

next step was to test the power level of the microwave pump signal to see if that had an effect on the direction of the double-resonance signal. The attenuation of microwave power was changed from 20 to 16, 13, and 10 dB; the double-resonance signals for each power level can be seen in Figure 3.11.

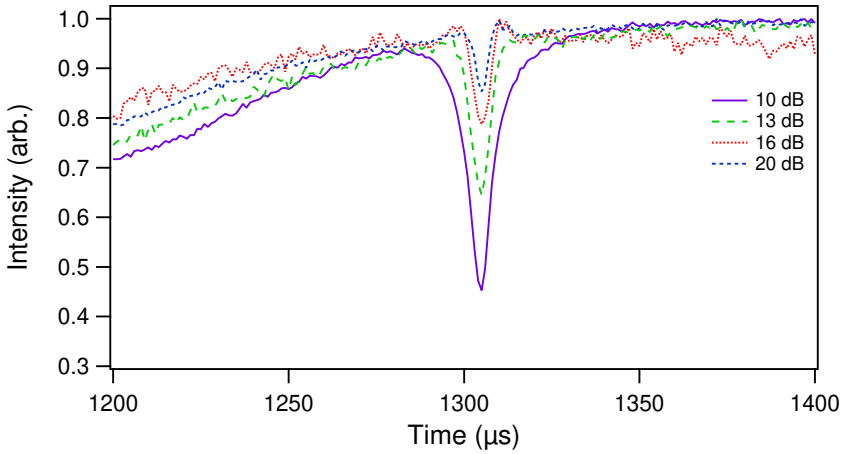

Figure 3.11: Methanol transition at 193,441.600 MHz, with the microwave chirped pulse centered on the resonant frequency of 12,178.584 MHz with various levels of attenuation at 10, 13, 16, and 20 dB. The width and sweep rate for chirped pulse are 100 MHz and 0.2 MHz/μs, respectively.

In general, the strength of the double-resonance signal depends directly on the power level, which is to be expected. However, there was no change in direction of the double-resonance signal regardless of which set of pump/probe transitions were observed, and regardless of power level. With this detection method we have clearly shown that it is possible to observe the double-resonance signal and thus identify which states are connected. Because the double-resonance signal only points in one direction, it is not possible to determine how the states are connected. To further investigate, the second detection method was used. For this method, the microwave frequency was fixed to a single value while the millimeter wave frequency was swept using the fast-sweep approach. The main benefit of using the fast-sweep technique is the increase in acquisition speed. For a traditional experiment with a repetition rate of 10 Hz, a spectral bandwidth of 10 MHz, a frequency step of 0.05 MHz, and 100 averages, a single acquisition will take around 2000 seconds [36]. In comparison, using fast-sweep with the same parameters as above, the scan would be complete in about 10 seconds. The spectra produced tested whether there were off-resonant effects on the millimeter/submillimeter spectral response that were not being probed by the first detection method. The microwave light was held at a constant frequency of 12178.584 MHz while the millimeter/submillimeter frequency was swept across the resonant transition; the results can be seen in Figure 3.12. It was suspected that the upward-pointing lobes on each side of the double-resonance signal were due to the AC Stark effect, as was previously predicted in microwave-radio frequency double-resonance experiments [42]. In the microwave-radio frequency double-resonance study, they saw the phase shift associated with the AC Stark Effect rather than the split lines. To confirm that this was the case, spectra were acquired with several different levels of microwave attenuation. It is clear from Figure 3.12 that the splitting between these lobes is dependent on the power level of the resonant microwave radiation. In their previous work on microwave-radio frequency double-

resonance, Schmitz et al. included a theoretical treatment of the observed effects using a density matrix formalism, which supports the claim that the effects being observed are indeed because of the AC Stark effect [42]. Additionally, in their Supporting Information, they provide diagrams showing predicted autler-townes doublets based on their experimental results and conditions.

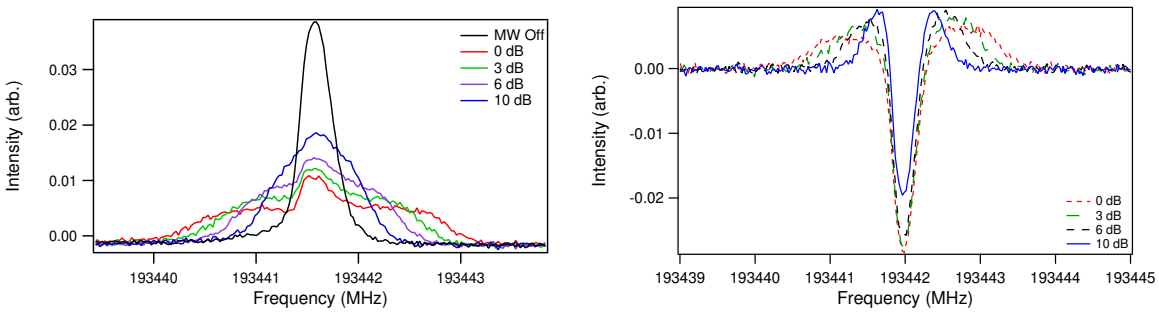

Figure 3.12: Fast-sweep millimeter spectrum of the 193,441.600 MHz methanol transition, with the microwave pump held at 12178.584 MHz. Attenuation levels of 0, 3, 6, and 10 dB were used, resulting in shifts to the Autler-Townes doublets from the AC Stark effect. The raw data can be seen on the left, while the background (i.e microwave off) subtracted data can be seen on the right.

Additional experiments were conducted to explore the effects of detuning the pump frequency. When the microwave light is tuned slightly off resonance from the stationary state, this shifts the intensity and creates an asymmetric doublet, which can be seen in Figure 3.13. The effects of detuning were initially investigated in order to determine whether it is possible to use this effect to identify the nature of connectivity for the pump radiation (i.e., whether it is connected to the lower or upper state of the probe transition). Unfortunately, this detuning does not provide enough information to completely determine the connectivity of the microwave and millimeter-wave transitions, as there are only two possible responses (higher intensity to the left or right), but four potential coupling schemes. Therefore, while this technique is helpful for determining basic connectivity between two molecular transitions, it cannot be used to discern specific level identification. Despite this drawback, it can still prove invaluable when assigning complex rotational spectra.

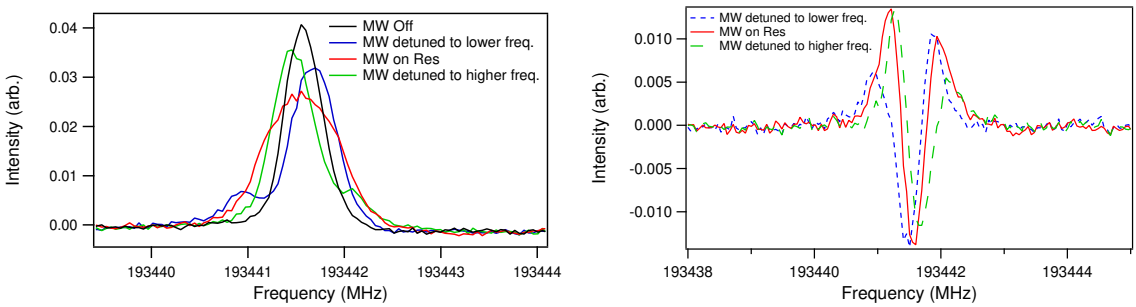

Figure 3.13: Autler-Townes doublets caused by the AC Stark effect. The effects of detuning are dependent upon the millimeter/submillimeter state being observed. In this case, the blue-shifted peak intensity is increased when the detuning frequency is below the resonant frequency, while the red-shifted peak decreased. When the detuning frequency is higher than the resonant frequency, the opposite effect occurs, with the blue-shifted peak lower and the red-shifted peak higher. The raw data can be seen on the left, while the background subtracted data is displayed on the right.

The results of these experiments did not follow the expectations based on population transfer as is assumed in a standard double-resonance experiment where the pump radiation is introduced at high power levels. Instead of inducing large population transfer to connected levels, the microwave radiation is splitting the stationary states into dressed states because of the AC Stark effect. The dressed states, known as an Autler-Townes doublet, are separated by the Rabi frequency, and the splitting is tuned by changing the microwave power level [23, 149, 150]. In this experimental scheme, there is not enough power to completely move population out of the stationary state; rather the population in the stationary state decreases, because some population is shifted to the dressed states. The decrease in population in the stationary states manifests as a decrease in signal for millimeter transitions that connect to the stationary states. Scanning across the millimeter-wave spectrum while holding the microwave frequency constant results in a spectrum with a central peak that corresponds to the transition between stationary states, and two neighboring peaks that correspond to the transition between the dressed states and the connecting stationary level. When the pump frequency is tuned to a transition frequency involving two stationary states, the resulting population in the two dressed states is equal, re-

sulting in a symmetric spectral line pattern. When the pump frequency is slightly detuned from the transition frequency involving two stationary states, the population distribution in the two dressed states is unequal and the spectral line pattern is asymmetric. This is the same result obtained by Wilson and coworkers in their MW-MW double-resonance studies on OCS [43, 49]; they referred to these off-resonant signals as "creepers" which could be shifted in intensity by detuning the pump frequency, and could be shifted in location by changing the power and hence the Rabi frequency.

We have performed benchmarking tests on a microwave-millimeter/submillimeter double-resonance spectrometer that can be used to probe rotational level connectivity in complicated spectra. This spectrometer uses technology from broadband CP-FTMW and fast-sweep millimeter/submillimeter spectroscopy to increase the acquisition speed for double-resonance spectra, greatly advancing the utility of these methods for routine characterization of complex mixtures and dense spectra resulting from complex internal motion, therefore adding a useful tool for rotational spectroscopists to use. This spectrometer can be operated in two modes: the microwave radiation can be swept across a broad frequency range, enabling multiple connecting transitions to be probed in one experiment; or the millimeter/submillimeter radiation can be swept across a broad frequency range, enabling a single connecting transition to be identified in a complex and dense spectrum that might otherwise be unassignable. Autler-Townes doublets arising from the AC Stark effect were observed, indicating that this experiment leads to splitting into neighboring dressed states arising from interaction with the electric field of the microwave radiation, rather than full population transfer arising from high-power input. Detuning the pump frequency shifts the symmetry of the Autler-Townes doublets, but does not enable specific connecting level identification.

3.4 Cavity Enhanced Spectroscopy

While the previous three techniques have focused on increasing effective data acquisition, spectral acquisition speed, and the ease with which complex data can be assigned, the last major component focuses on dramatically increasing sensitivity. If the sample cannot be detected then PVTLI, LIFS, and MW-mm double-resonance are not useful. The first attempts to do this came in the form of multi-pass optical arrangements, but the obvious next step would be to upgrade to an optical cavity to increase the sensitivity of the spectrometer. Optical cavities can be used to capture light between two highly reflective surfaces. The reason for doing this is influenced by the Beer-Lambert law and pathlength as shown in Equation 3.1. Of the variables that can be changed, pathlength can be increased by changing the optical arrangements. In a simple, single-pass arrangement, the light would pass through the sample one time. Now, switching to a multi-pass arrangement, it is possible to increase the number of passes by more than an order of magnitude under absolutely ideal conditions. The amount of passes depends greatly on the beam waist and focusing properties of the Gaussian beamshape; the smaller the beam waist the more passes can be generated with a multi-pass arrangement. This is because the light can be more tightly fit on the mirrors without light being lost on the mirror edges. With the current equipment and the beam waist of light being used, the highest number of effective passes produced is 7 passes and only increases the pathlength by a factor of 5.5. This is where optical cavities may provide an advantage. They are able to dramatically increase the number of passes the light takes through the sample. The increases in passes is typically on the order of two to three orders of magnitude and is thus the ideal optical arrangement when attempting to maximize sensitivity.

$$Log_{10}\frac{I_o}{I_t} = \epsilon lc \tag{3.1}$$

The basic use for an optical cavity is to capture a certain frequency of light between reflective surfaces, typically two concave mirrors. In order for light to be trapped in the cavity it has to be a resonant frequency of light. Which frequencies of light can be trapped in the cavity depends on the distance between the mirrors. If the mirror edges are treated as a hard boundary condition, this means only integer values of the distance between the mirrors will create a standing wave in the cavity and thus form a stable resonator. Due to this nature, a number of cavity modes will form and the separation between these modes are detailed in Equation 3.2 [151, 152].

$$\Delta\nu_{FSR} = \frac{c}{2d_{act}} \tag{3.2}$$

The spacing between modes is $\Delta\nu_{FSR}$, which is the free spectral range. It is typically defined in units of Hertz. As these experiments are in the THz regime, the units of MHz for $\Delta\nu_{FSR}$ will typically be used. The speed of light in the resonating medium is c, in meters per second, and d_{act} is the actual distance between the two resonators, i.e., the mirrors, in meters. One way to define how effective the coupling of light into a cavity is to consider the with the quality factor term Q. There are no units associated with the quality factor as it is a ratio between the observed frequency, ν, over the linewidth, $\Delta\nu$. Both of these units are in terms of Hertz. Additionally, the quality factor can be defined as the product between the angular frequency, ω and the decay time constant for the resonators, τ_{photon}. The angular frequency is in units of Hertz and the time constant is in units of seconds. These definitions for the quality factor can be seen in Equation 3.3.

$$Q = \frac{\nu}{\Delta\nu} = \omega\tau_{photon} \tag{3.3}$$

The decay time constant is defined as the ratio between the length of the resonator, the product of the speed of light in the medium, and a loss parameter, α, as shown in Equation 3.4. In order to simplify the math, the loss parameter will be treated as 1.

This has the benefit of changing the distance variable from the actual distance between the resonators to the effective distance between the resonators, thus providing a way to determine the increased pathlength and the number of passes the cavity produces.

$$\tau_{photon} = \frac{d}{c\alpha} \tag{3.4}$$

Next it would be beneficial to change the angular frequency back into normal frequency terms. The difference between the angular frequency and normal frequency is a factor of 2π as seen in Equation 3.5. This produces frequency in terms of Hertz.

$$\omega = 2\pi\nu \tag{3.5}$$

If Equations 3.3, 3.4, and 3.5 are combined and then rearranged to solve for the distance term, it would produce Equation 3.6. λ is the wavelength of light caught in the resonator in units of meters. By setting the loss parameter to 1, the distance becomes the effective distance in the cavity. By not accounting for the loss, the distance changes from the actual distance between the resonators to the effective distance between them.

$$d_{eff} = \frac{Q\lambda}{2\pi} \tag{3.6}$$

By taking the ratio of the effective length of the resonator and the actual length of the resonator, the number of passes produced by the cavity can be determined as shown in Equation 3.7.

$$Number\ of\ Passes = \frac{d_{eff}}{d_{act}} \tag{3.7}$$

Lastly, returning the loss parameter that was set aside earlier, this is simply the inverse of the number of passes or the ratio between the actual length over the effective length as described in Equation 3.8.

$$\alpha = \frac{1}{Number\ of\ Passes} = \frac{d_{act}}{d_{eff}} \tag{3.8}$$

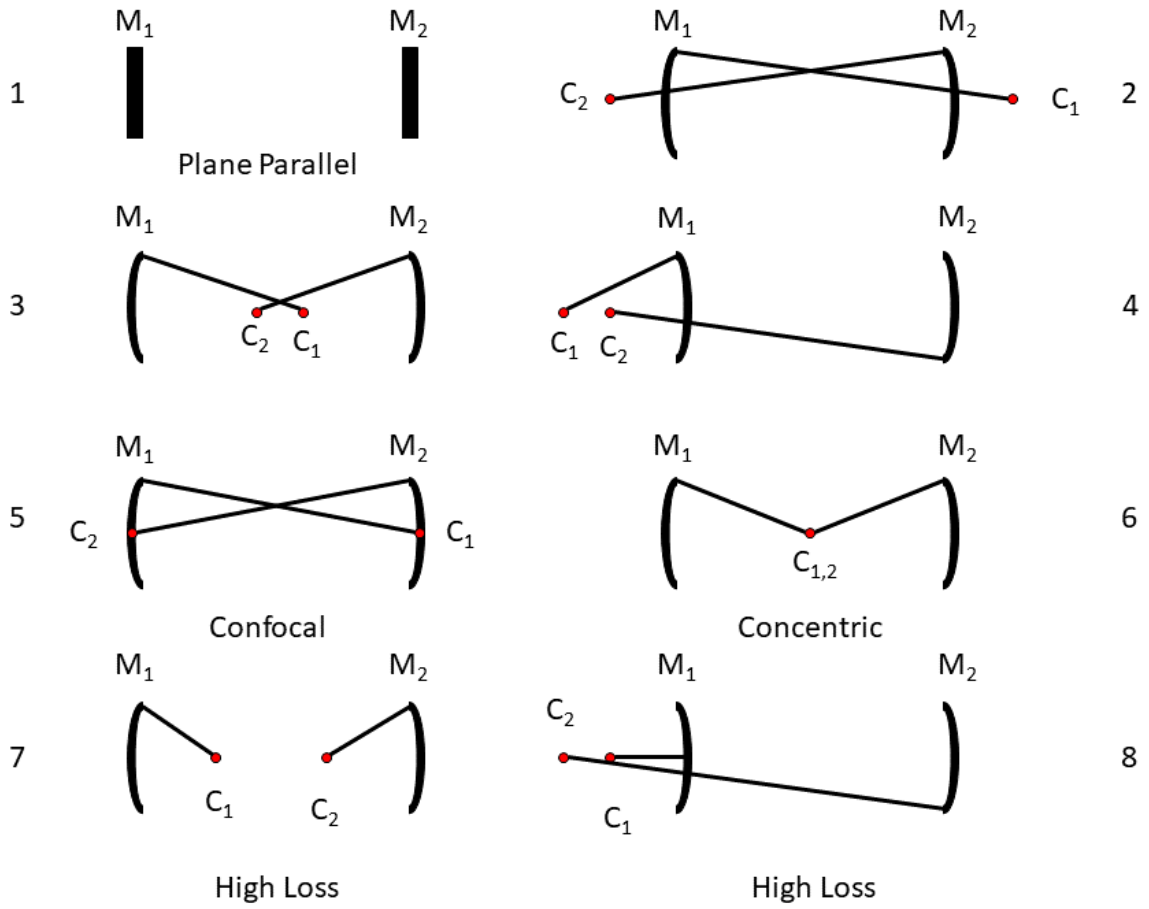

Figure 3.14: Different configuration of mirrors in order to produce an optical cavity. The first six show stable resonators, while the last two shown unstable resonators. For the purposes of this body of work configurations, 3, 5, and 6 are the most applicable. This figure was recreated based off of the original found in Quantum Electronics [151].

With the basics of how cavities function mathematically, it is now possible to talk about how the cavity was produced for these experiments. The mirrors available are a set of spherical mirrors (Edmund Optics, 15.24 cm diameter and 15.24 cm focal length, NT32-836) and one additional spherical mirror (Edmund Optics, 15.24 cm diameter and 30.48 cm focal length, NT32-839). With the use of these spherical mirrors, there are three possible stable resonators that can be made: a confocal resonator, a concentric resonator, and a resonator between these two extreme resonators. These

correspond to configuration 5, 6, and 3 in Figure 3.14. The confocal arrangement has the focal points of the mirrors on the surface of the opposing mirror, while the concentric arrangement has the focal points of the mirrors overlapping at the midpoint. By adjusting between these two extremes it is possible to change the free spectral range of the cavity and thus change the spacing between cavity modes. This functionally means that by adjusting the length of the cavity between the confocal and concentric arrangements, it is possible change the resonate frequency in the cavity and thus record a spectrum across frequency space using a cavity.

The end goal would be to apply a cavity enhanced optical arrangement to be used in conjunction with the supersonic expansion based experiments. To do this, an optical cavity was built based on a design made in the De Lucia lab [39]. In this previous work, the De Lucia group produced an optical cavity by placing the light source perpendicular with the mirrors and then using a Mylar beam splitter to couple light into the cavity. Placing a beamsplitter in the cavity would normally destroy the quality of the resonator; however, for such long wavelength light, the impact of the beamsplitter is minimal if the cavity is of good quality. Thus, the recorded power profile would show dramatic dips in power when the frequency was resonant with the cavity. Before building an optical cavity in the vacuum chamber, a cavity was built on the table top in order to determine if it would be possible to implement one with the current equipment available in the lab. The equipment used to produce this test cavity included a microwave synthesizer (Agilent Technologies, E8257D PSG with 1EA, UNU, 550, and UNT options) which outputted light to a VDI multiplier chain (Virginia Diodes Inc., S197(c)). This light was then collected and collimated the beam using a 10 cm focal length lens and directed to a 30 cm focal length lens that focused the beam on to a Mylar beam splitter. The beam splitter was custom built and allowed for different thicknesses of Mylar to be used as the beam splitter. The different thicknesses included 10, 5, 2, 1, 0.1 mil (thousandths of

a inch) mylar. The mirrors that constituted the cavity were a set of spherical mirrors (Edmund Optics, 15.24 cm diameter and 15.24 cm focal length, NT32-836) that were initially set in a concentric configuration. One of the mirrors was mounted onto a translation stage that allowed for the mirror to be moved forward and backward, thus changing the length of the cavity. For the results being discussed, the cavity length was set to 0.29 m. On the other side of the beam splitter was another 30 cm lens that collimated the light to a 10 cm focusing lens, which focused the light into the InSb hot electron bolometer (QMC Ltd., QFI/2BI). The output of the bolometer was processed using a lock-in amplifier (Stanford Research Systems, Model SR 830 DSP). The reference signal from the synthesizer to the lock-in consisted of an AM modulated signal with 15 kHz mod. frequency, and 10.0 % mod. depth. The lock-in detected the first harmonic of the bolometer signal and sent the processed signal to a digital oscilloscope (National Instruments, PCI-5124) to record the output. The details of this arrangement can be seen in Figure 3.15.

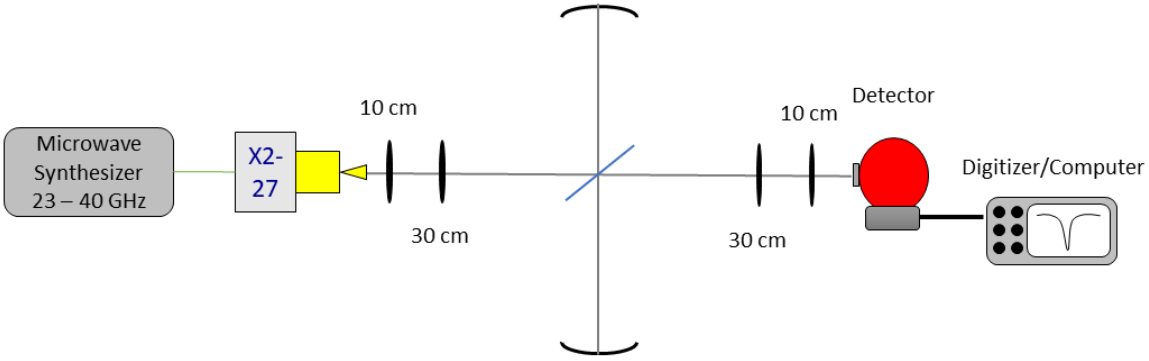

Figure 3.15: Schematic for a resonator based on the work of DeLucia et al. [39]. The light from the multiplier chain is collected using a 10 cm focal length lens and is then focused onto the beamsplitter using a 30 cm focal length lens. The beamsplitter then coupled the light into the cavity that was produced by two 12 in focal length mirrors set roughly 0.29 meters apart from each other. This produced a roughly concentric optical cavity. Afterwards, another 30 cm lens was used to collect the light from the cavity and direct it to a 10 cm lens that focused the light into the detector.

With the cavity produced and aligned, a series of tests were conducted in order to determine the cavity quality factor of each of the different thickness of Mylar

beamsplitters. The results from tests of each of the cavities are shown in Figure 3.16. The frequencies used to test each of the cavities were not overlapping, and thus they were removed from the axis labels in order to better compare the produced cavity modes. The center frequencies for each of the modes is given in the figure caption. As shown in the figure, as the thickness of the Mylar decreases the cavity modes dramatically narrow. Thus, the quality factor increased as well, as shown in Table 3.2. While decreasing the thickness of the Mylar increased the quality factor, it also decreased the amount of light being trapped in the cavity. This is seen as the depth of the cavity mode decreases as the Mylar thickness also decreases. This is not surprising as the thicker the beamsplitter, the more effective it is at coupling light into the cavity. Because of its effectiveness at coupling the light into the cavity, the thicker beamsplitters also produce a high loss cavity which causes the quality factor to decrease.

Due to the reduced light being trapped in the cavity, less light will end up interacting with the molecules being probed by the cavity. Thus, it becomes necessary to not just consider the quality factor of the cavity, but also the amount of light being coupled into the cavity. To effectively consider this, the signal-to-noise ratio was evaluated as well. As shown in Table 3.2, the values for the SNR go in the opposite direction of the quality factor with the thickest beamsplitter having the highest value. With this value in hand, the SNR$\times$Q products were examined. This value allows for the consideration of both the quality factor of the cavities and the amount of power being coupled into the cavity. From these values, it was determined the best beamsplitter to use was the 2 Mil thickness. The 2 Mil beamsplitter produces a cavity with 47 passes with about half of the light being coupled into the cavity. Thus, the prospective increase in the molecular signal should be around a factor of 23.5 when compared to a single-pass optical arrangement. The factor of 2.75 that is gained by utilizing a multi-pass optical arrangement is an order of magnitude lower

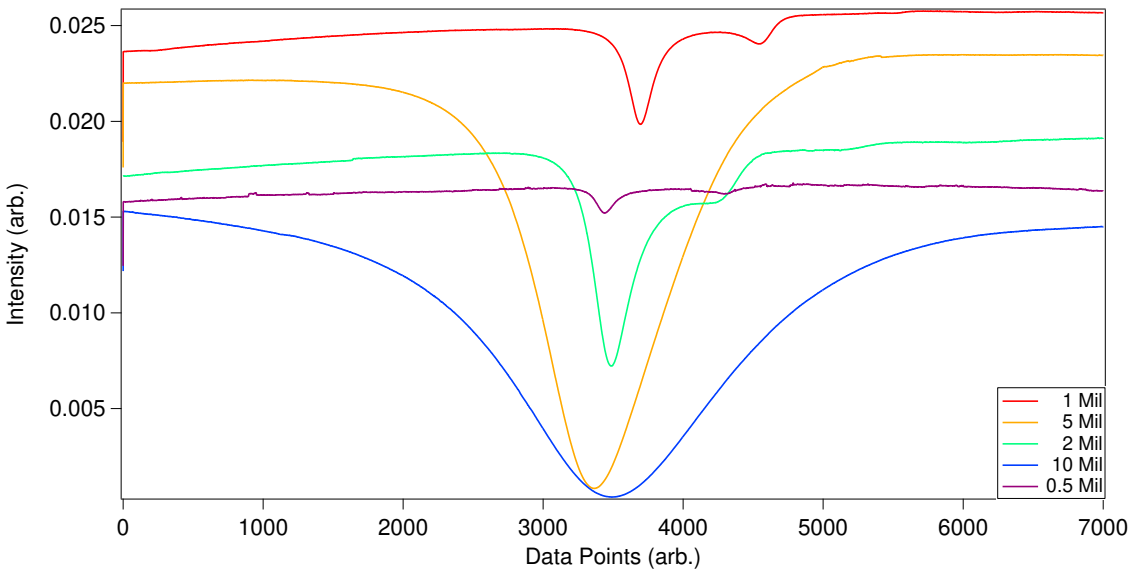

Figure 3.16: Different thickness beamsplitters were made and tested to determine the quality factor each beamsplitter produced. The signal shown here is a single cavity mode produced by the cavity. There are higher order cavity modes shown here appearing as a side mode. These are prominently shown with the 0.5, 1, and 2 Mil thickness traces, but are present in each of the traces. These higher order modes cause a slight asymmetry in the recorded cavity mode. The base frequencies each mode was produced at was removed in order to directly show the how the cavity mode narrowed as the thickness changed. The original frequencies were as follows: 10 Mil-181,064.92 MHz; 5 Mil-180,643.62 MHz; 2 Mil-180,686.86 MHz; 1 Mil-180,701.96 MHz; 0.5 Mil 180,709.37 MHz

than what is gained by using this cavity arrangement. The cavity produced here was then compared to a previously reported study using polarizers as the reflective surface [153]. All values for the polarizer cavity were taken from that body of work. For the polarizer cavity, the quality factor was well above any of the values produced with the beamsplitter cavities, but the SNR was not very high as seen in Table 3.2. As a result, the 2 Mil cavity was still a better optical arrangement due to the amount of power being coupled into the cavity.

Despite the benefits of using a cavity, there were a number of problems encountered that have delayed the implementation of this design for spectroscopic experiments. The first problem encountered was the cavity was only 0.29 meters long, which is an insufficient length for use with a discharge source that readily arcs to nearby metal.

Table 3.2: Calculated values for the quality factor, the SNR, the SNR×Q product, and the number of passes each cavity produced including for the polarizer cavity. The value determining the best cavity to use in the SNR×Q product as it accounts for both the amount of light being coupled into the cavity and how many passes the cavity produces. The higher the value the better the cavity.

Mylar Thickness	Quality Factor	SNR	SNR ×Q Product	Number of Passes
10 Mil	9,894.257	3,253.0654	32,541,189.43	8
5 Mil	17,319.621	2,469.322	42,767,685.59	15
2 Mil	52,071.147	1,821.687	94,857,213.11	47
1 Mil	88,579.387	729.006	64,574,853.80	80
0.5 Mil	112,241.845	86.738	9,735,657.90	102
Reflective Surface	Quality Factor	SNR	SNR ×Q Product	Number of Passes
Polarizer	125000.000	265.18800	33,172,571.25	67

One possible way to solve this problem was to create an asymmetric cavity. This was attempted using a 12 in focal length mirror in conjunction with a 18 in focal length mirror. The cavity produced is akin to cavity 5 in Figure 3.14. The mismatched focal lengths of the mirrors cause significant losses, resulting in a poor cavity quality. Due to these reasons, the implementation of a cavity-enhanced spectrometer was put on hold.

3.5 Future Instrumental Developments

The future for the instrumental development in the THz regime is very bright. The need for faster and more sensitive spectrometers is great. The push up to higher frequencies in telecommunications, security, and far-IR astronomy means that new hardware, light sources, and detectors are undergoing rapid development, lending themselves readily to new spectrometer designs. Also, with upgrades like a 22-pole ion trap and time-of-flight mass spectrometer, these would greatly improve the lab's capability to detect highly unstable ions. With the advancements of MW-mm double resonance, it will become increasingly possible to assign the complex rotational spectra produced by highly fluxional ions. Additionally, it should be possible to combine fast-sweep/LIFS and a cavity to produce a type of frequency comb that will be able

to average very quickly while having a very sensitive detection. This could revolutionize data acquisition for complex organic ions. If these are combined into a single experiment, collecting data for complex organic ions will be quicker and should make assignment much simpler.

Chapter 4 Protonated Formaldehyde

The instrument development conducted for this thesis was motivated by the production, detection, and assignment of complex fluxional organic ions. The most central organic ion relevant to astrochemistry is protonated methanol. As discussed in the introduction, methanol is the most common complex organic molecule in space, and as such protonated methanol should be the most common complex organic ion in space. However, protonated methanol has not been detected by radio astronomy, because there has not been a lab-based detection of protonated methanol with rotational spectroscopy in order to compare to the astronomic data. Protonated methanol is hard to produce and its spectrum is predicted to be difficult to assign. Also, the addition of a second hydrogen on the oxygen makes this ion highly reactive, and thus hard to produce in abundance. Because of the increased reactivity of protonated methanol, it can only be produced in a supersonic expansion discharge source. If production was attempted in a discharge source like a hollow cathode, the likely result would be for protonated methanol to react with methanol and snowball into organic tar. Also, the additional hydrogen causes the ion to have a H_2O wagging motion as well as a methyl rotor. This internal motion will cause the lines to be split into numerous components, thus making spectral assignment very difficult. To put it in perspective, protonated methanol is isoelectronic with methylamine. methylamine is well-known as a prototype for two low-energy internal motions, has a significant amount of literature related to its spectral assignment, and is a rather difficult molecule to assign. These difficulties spurred the development of PVTLI, LIFS, and MW-mm double resonance and is why optical cavities were investigated.

4.1 Protonated Formaldehyde from Paraformaldehyde Powder

Before blindly investigating protonated methanol, it was prudent to establish that the laboratory equipment in use could produce complex organic ions in sufficient quantity for spectroscopic study. Thus, it was decided that the first target ion would be protonated formaldehyde. There were two reasons for this: the protonation method should be similar to that of protonated methanol, and previous work has been done on protonated formaldehyde as mentioned in the introduction. Therefore, instead of blindly searching for new lines, it is possible to peak up on a single line and maximize its intensity. Additionally, both ions should be produced through the addition of a hydrogen on the oxygen atom of either methanol or formaldehyde as shown in Reaction 2.3. Thus, developing a way to protonate formaldehyde through hydrogen addition should utilize the same equipment that protonated methanol will require. These similarities between protonated methanol and protonated formaldehyde, in addition to having a number of known lines, made protonated formaldehyde the ideal ion to begin our work on the production of complex organic ions.

Before work on producing protonated formaldehyde could begin, it was prudent to determine if the ion source could produce protonated species. To test the source, it was decided that HCO^+ would be the ideal candidate as it is possible to detect both the parent molecule, CO, and the product HCO^+ using rotational spectroscopy. To do this, a 10% carbon monoxide (Matheson) in helium (Nexair, ultra-high purity) gas mixture was prepared. The gas pressure was held at 110 PSIG with a flow rate of 10 sccm with a 500 sccm flow controller (MKS 1179A). The hydrogen gas (Nexair, ultra-high purity) was also held at 110 PSIG with a flow rate of 70 sccm with a 5000 sccm flow controller (MKS 1179A). The pulsed valve (Parker Hannifin, Series 9 general valve, 1 mm pinhole) ran at a repetition rate of 10 Hz. The pulse time and duration was controlled by a pulsed valve driver (Parker Hannifin Iota One, 060-0010-

900) and a digital delay generator (Stanford Research Systems DG645). The power provided by the high voltage power supply (Spellman, SL2PN2000) was held at 900 V and 4 mA with a 1 kΩ ballast resistor and the voltage was applied using a pulse generator (Directed Energy Inc., PVX-4150). Ring electrodes were used to produce the discharge and ionize the sample gas. The operation of the pulse valve and the discharge was synchronized using the delay generator. With the delay generator, the pulse width was set to 0.5-1 ms depending on pulse valve conditions. This resulted in operating pressures of roughly 35 mTorr. Additionally, the discharge pulse width was 0.7-1.2 ms, with the discharge pulse centered on the gas pulse.

As a test to determine if the parent molecule, CO, was present, the multiplier chain was placed in the Band 5 configuration which covers the 130-225 GHz range. The CO line is on the edge of this range, but there was still enough output power to detect it. Fast-sweep was used to record all spectroscopic data used in the production of formylium (protonated carbon monoxide). After some fine-tuning of the gas flows, the CO spectrum seen in Figure 4.1 was recorded. This peak intensity compared nicely with previously recorded spectra of this line. As such, it was possible to proceed to the formation of formylium. After numerous adjustments to the gas ratio and to the discharge, HCO^+ was formed as shown in Figure 4.2. The ion was produced by initially forming H_3^+ from the hydrogen gas. The H_3^+ ion is an excellent proton source, and through a collision with carbon monoxide donates a proton to form formylium. The production efficiency for this reaction was roughly 1-2% and this reaction has little possible side products. This means the while it is possible to create ions, their number density will be very low. With the formation of formylium, it was established that protonation through hydrogen addition was a possible route to form both protonated formaldehyde and protonated methanol.

The next step was to transition from the production of formylium to protonated formaldehyde. While there are multiple ways to produce protonated formaldehyde,

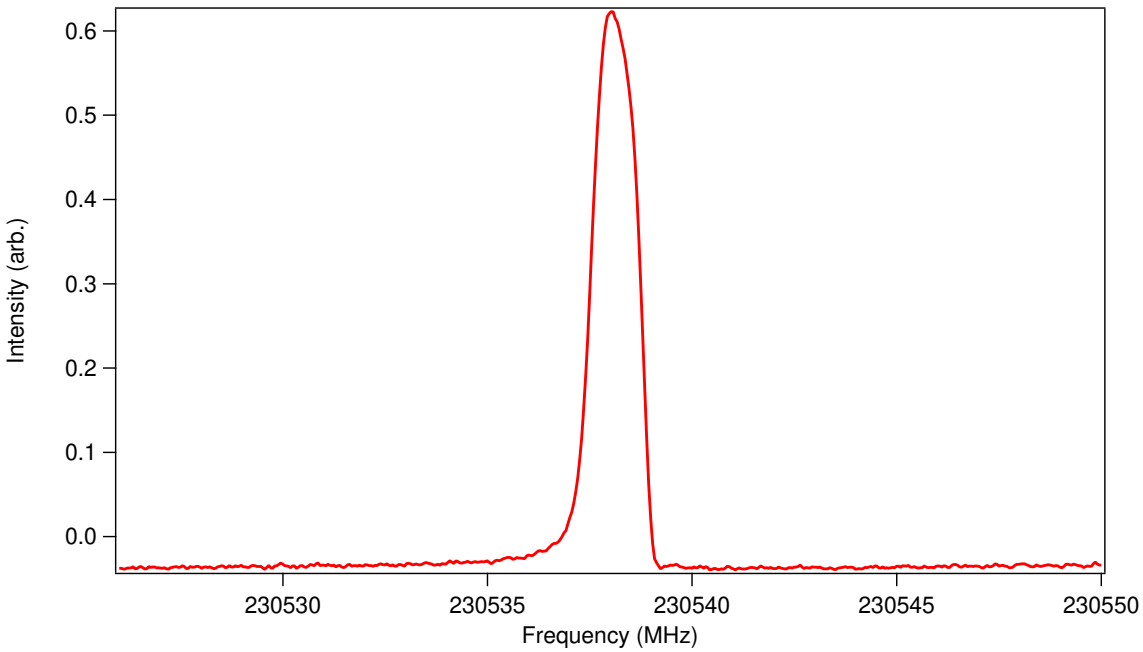

Figure 4.1: The 2 ← 1 carbon monoxide transition at 230537.224 MHz. The transition was recorded in band 5 using the fast-sweep data acquisition method. Using fast-sweep has caused the line to be slight blue shifted, by roughly 1 MHz, off of its true line center. The asymmetry in the line is do to the Doppler effect.

the most direct way would be to take paraformaldehyde powder, heat it to produce gaseous formaldehyde, and then flow hydrogen gas over the heated powder. The last step involves taking the formaldehyde and hydrogen gas mixture and applying a discharge current to the gas mixture as it supersonically expands. This way the ion forms and then the reactions are quenched by the expansion. To do this, hydrogen gas (Nexair, ultra-high purity) at 115 PSIG was metered by a 5000 sccm flow controller (MKS 1179A) set to 95 sccm flowed over paraformaldehyde powder (Alfa Aesar, paraformaldehyde 97%). The powder was contained in copper mesh that was inserted into the gas line. The metal fitting that contained the powder was wrapped in heating tape. The tape gently heated the powder to 50 °C in order to produce formaldehyde gas. Using a pulsed valve (Parker Hannifin, Series 9 general valve, 1 mm pinhole) in conjunction with a ring electrode discharge source, a plasma was produced and supersonically expanded. Again, the pulse width of the pulsed valve was set to 0.5-

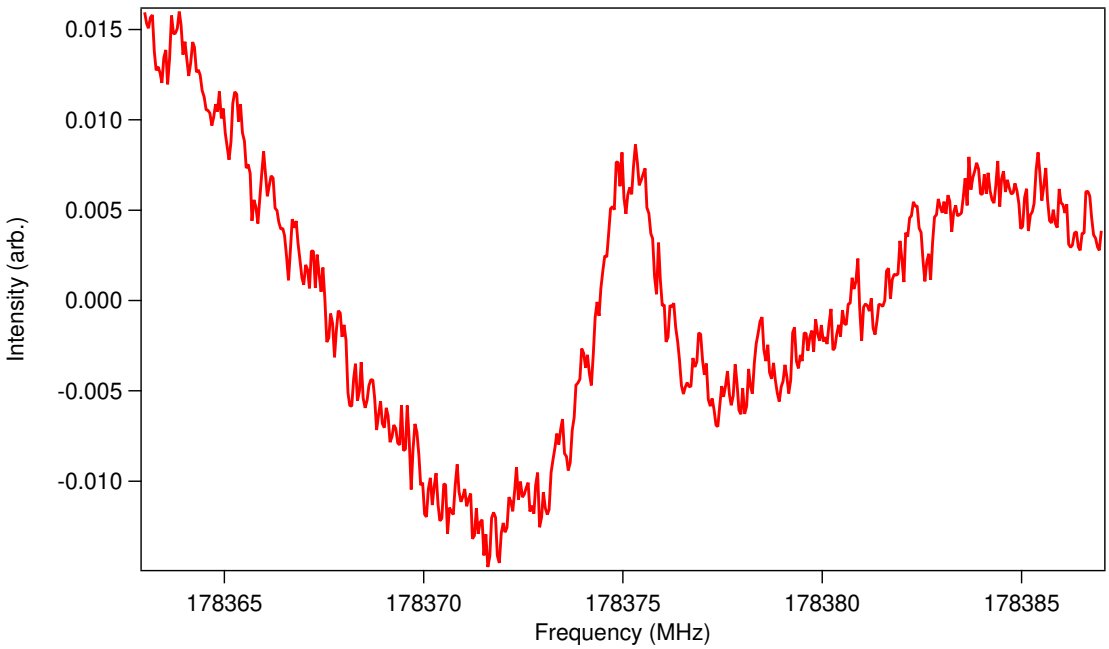

Figure 4.2: The $2 \leftarrow 1$ formylium transition at 178375.056 MHz. The transition was recorded utilizing the fast-sweep data acquisition method. The line is blue shifted by about 0.1 MHz. This is due to the center frequency selected for the fast-sweep scan being closer to the true line center of the transition. The asymmetry in the line is primarily due to the RF generated by the discharge source. There is some asymmetry due to the Doppler Effect, but this is much smaller than the asymmetry due to the RF noise.

1 ms. The discharge was applied over roughly 0.7-1.2 ms. The discharge timing was centered on the gas pulse. The pulsed valve and the pulsed discharge ran at a repetition rate of 10 Hz which was set by a digital delay generator (Stanford Research Systems DG645). The discharge was produced using a high voltage power supply (Spellman, SL2PN2000) in conjunction with a pulse generator (Directed Energy Inc., PVX-4150). The power supply outputted a voltage of 900 V with a current of 3 mA. A ballast resistance of 1.6 kΩ was used to stabilize the discharge.

Initially, before paraformaldehyde was found to be the best formaldehyde precusor, aqueous formaldehyde was used. The first problem encountered was how to extract formaldehyde vapor from the solution. The initial thought was to take the aqueous formaldehyde and bubble hydrogen through it at high pressure. To accomplish this

goal a high pressure bubbler was created, but the high amount of water and methanol in the aqueous formaldehyde solution. This would cause problems in two areas: first, the discharge would produce many side products, and as a result, second, concern being the number of unknown lines produced by these side reactions would increase significantly. Thus, it was decided to use paraformaldehyde powder as the source for the parent molecule. A special gas line fitting was developed in order to be able to handle increased temperatures and have a convenient way to add more sample. The paraformaldehyde powder was initially wrapped in copper mesh and then inserted in the gas line. While this was effective, it made refreshing that sample difficult. As such, copper mesh was inserted into the gas line perpendicular to the flow of hydrogen gas in order to stop the powder from moving away from the heat source as gas flowed. The heat source was heating tape and was set to heat the metal fitting to roughly 50 °C. Once the flow rate and heating setting were set, the spectrum of formaldehyde was recorded using fast-sweep as seen in Figure 4.3. There is a slight asymmetry in this spectrum that is caused by the Doppler effect from either an asymmetric expansion, or misalignment of the gas pulse relative to the spectrometer beam.

With sufficient amount of formaldehyde being introduced into the gas phase, the next step was to light a discharge and produce protonated formaldehyde. The discharge was produced using ring electrodes and after some adjustments to the ballast resistors, the spectrum of protonated formaldehyde was taken using fast-sweep as shown in Figure 4.4. As seen in the figure, the protonated formaldehyde signal slowly grows in and can be seen at 10,000 averages. A definite detection was made at 50,000 averages as shown in Figure 4.5. Here the spectrum was fit with a polynomial to remove the odd baseline produced by fast-sweep and smoothed using 9-point boxcar smoothing. This detection has been the lowest detected absorption coefficient this lab has ever detected to date, $\alpha = 3 \times 10^{-11}$ cm^{-1}. This number was determined using Equation 4.1. The units for the absorption coefficient, $\alpha_{\max}$, is cm^{-1}. Line

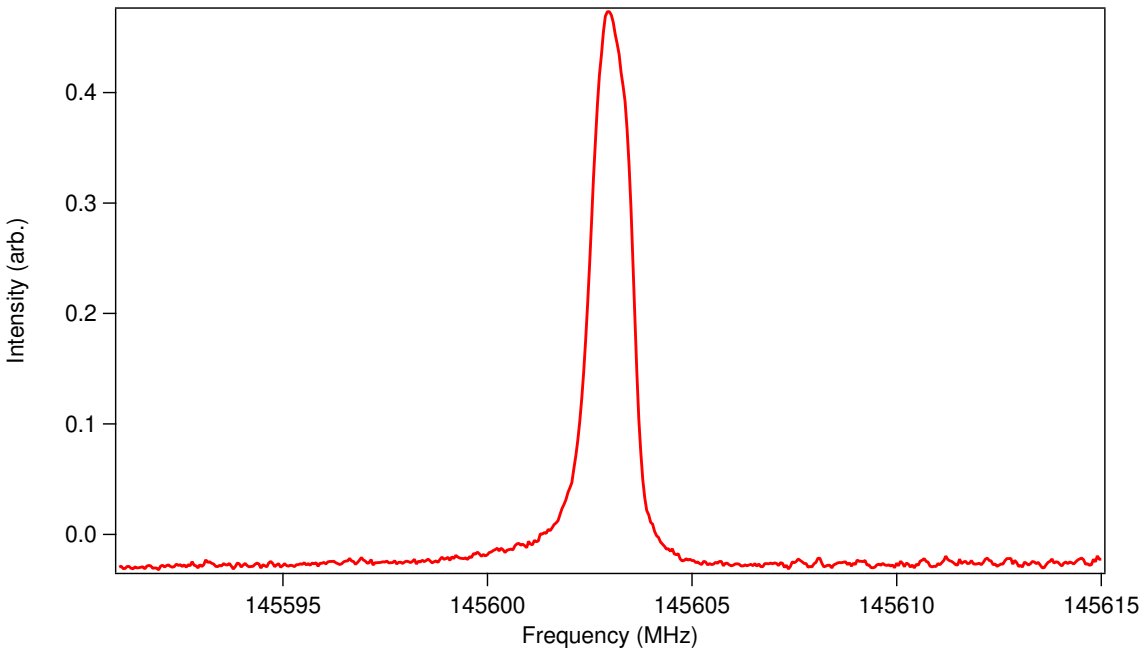

Figure 4.3: The $2_{0,2} \leftarrow 1_{0,1}$ formaldehyde transition at 145602.949 MHz. The transition was recorded in band 5 using the fast-sweep data acquisition method. The line is blue shifted by approximately 0.3 MHz due to fast-sweep. The asymmetry in the line is due to the Doppler effect.

intensity at T temperature, $I_{\mathrm{ba}}(T)$, has units of nm^2·MHz, while the partial pressure of the absorber, p, is in Torr. T$_\circ$ is defined as 300 K, while T is the temperature of the absorber in Kelvin. The Doppler width is $\Delta\nu_{\mathrm{d}}$ with units of MHz. The previous lowest detected absorption coefficient was 5×10^{-9} cm^{-1} with the detection of the methoxy radical at 137.444 GHz [148]. The detection limit for this spectrometer was improved by two orders of magnitude over the course of this experiment.

$$\alpha_{max} = \frac{I_{ba}(T)p}{\Delta\nu_d}(T_\circ/T) \times 151.194\ cm^{-1} \tag{4.1}$$

Despite the dramatic increase in the detection limit and scanning with fast-sweep, this is still a very slow scanning rate. For a 10,000 average acquisition with 24 MHz spectral width, it took 16.6667 minutes to complete. If this is extrapolated to the entire frequency range that can be scanned using the current equipment, 50-1,000 GHz, it would take $\sim$ 459 days of constant running to complete. This does not

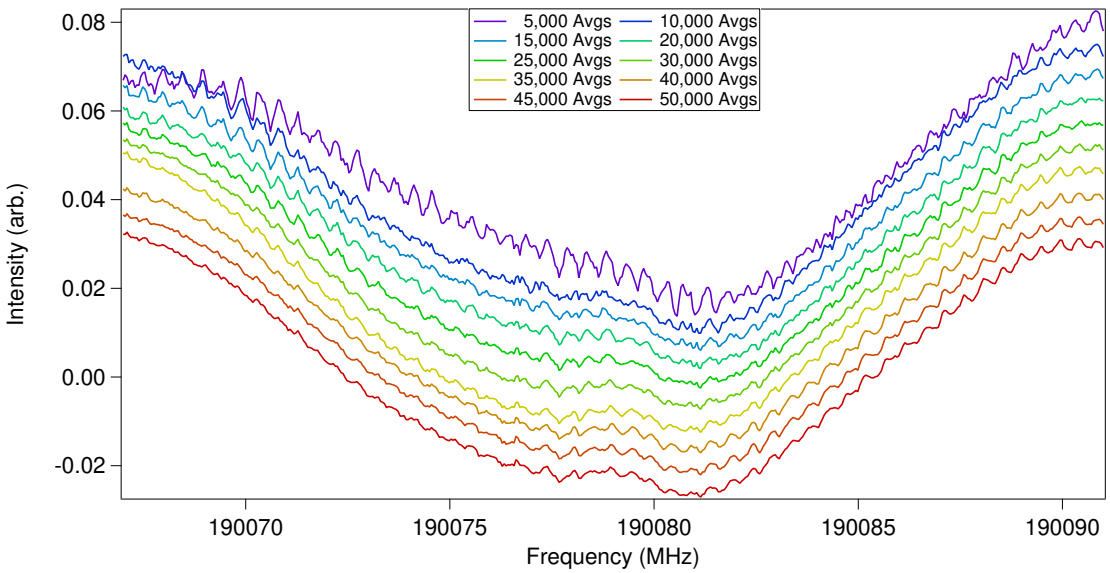

Figure 4.4: The $3_{0,3} \leftarrow 2_{0,2}$ protonated formaldehyde transition at 190079.131 MHz. The transition was recorded in band 5 using fast-sweep. The line is blue shifted by roughly 0.2 MHz by fast-sweep. The asymmetry caused the discharge source emitting a large amount of RF noise. The signal can be seen growing in as the number of averages increase. The line can be first clearly seen at 10,000 averages and the SNR of the line increases as the number of averages increases to 50,000.

include any of the time required to get accurate center frequencies using PVTLI. Additionally, over the course of this experiment the spectral signal would disappear, despite no experimental parameters being changed. This is likely due to the pulse valve tension changing slightly along with paraformaldehyde powder clogging the gas lines, but these issues take hours and sometimes days to properly fix. These adjustments would extend the 459 days of scanning required to scan across all the frequency space available using this equipment. Therefore, despite the success in producing protonated formaldehyde from paraformaldehyde powder, this approach is too inconsistent, and the number density is far too low to quickly produce spectra. Thus, other methods for producing protonated formaldehyde had to be considered. The two obvious choices were switching to methanol as the parent molecule and trying to remove a hydrogen to form protonated formaldehyde, or to attempting to produce protonated formaldehyde using a hollow cathode discharge source like previously done

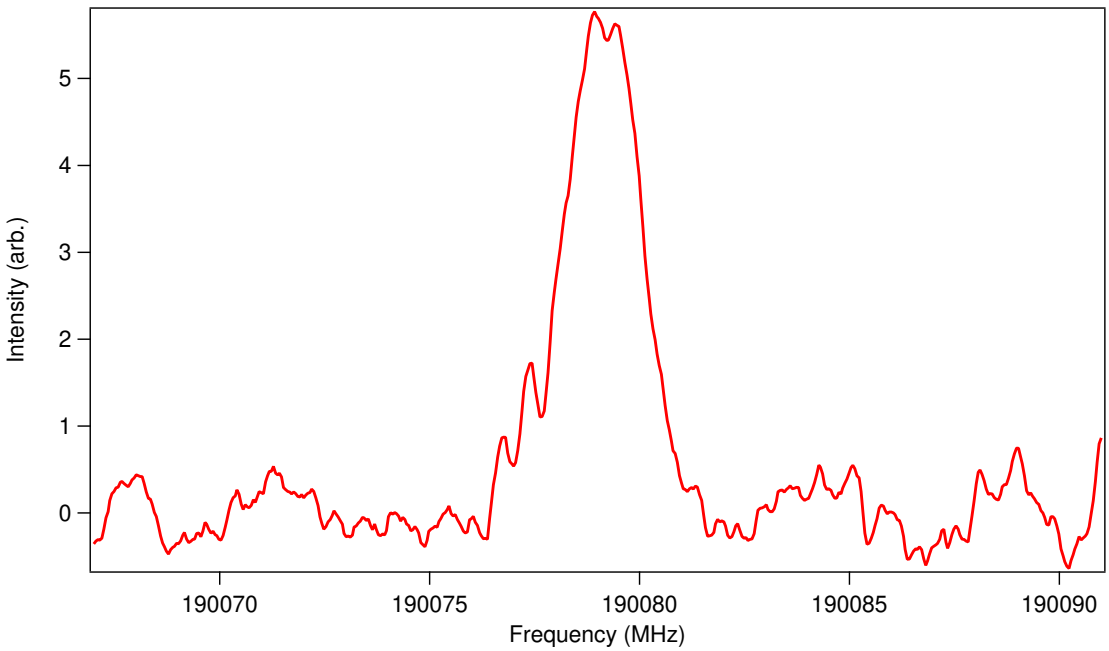

Figure 4.5: The $3_{0,3} \leftarrow 2_{0,2}$ protonated formaldehyde transition recorded with 50,000 averages at 190079.131 MHz. The transition was recorded in band 5 using fast-sweep. The baseline was subtracted using a polynomial fit and the like was smoothed using 9-point boxcar smoothing.

by Amano [27]. It was decided to first attempt to use methanol precursor in a pulse discharge experiment as to keep in line with the end goal of producing protonated methanol in a supersonic expansion discharge source.

4.2 Protonated Formaldehyde from Methanol

The use of methanol or ethanol as a precursor for protonated formaldehyde was established by the Duncan Group at the University of Georgia [31, 110]. Building off of their previous work, the ring electrode discharge source was replaced with a needle electrode discharge source, the polarity of the high voltage source was flipped to a negative polarity, and the ballast resistors were eventually removed. With these changes implemented the experimental setup changed to using a supersonic expansion created using a pulsed valve (Parker Hannifin, Series 9 general valve, 1 mm pinhole) which flowed 120 psig Argon gas (Nexair, ultra-high purity) through liquid methanol

(Fisher Scientific 99.9%). The gas expanded out of the pulse valve and was ionized by the needle electrode discharge source and supersonically expanding. The repetition rate for the pulsed valve and the pulsed discharge source was 10 Hz. This was set by a digital delay generator (Stanford Research Systems DG645). Here the gas pulse width was set to 0.5-1 ms depending on pulse valve conditions and the discharge pulse width was set to 0.7-1.2 ms. Resulting in operating pressures of roughly 35 mTorr. The discharge was produced using a high voltage power supply (Spellman, SL2PN2000) in conjunction with a pulse generator (Directed Energy Inc., PVX-4150). The power supply outputted a voltage of ± 900 V with a current of 3 mA. Typically, no ballast resistors were used to stabilize the discharge.

The initial target product to determine discharge conditions when running with a methanol discharge was formaldehyde. Formaldehyde was being produced in as shown in Figure 4.6. This signal was produced by normal lock-in detection as PVTLI had yet to be developed. The idea behind using formaldehyde was to find the peak formaldehyde intensity by adjusting discharge parameters like voltage and ballast resistance which in turn affected the current. The results of this testing can be seen in Figure 4.7. Here, the peak formaldehyde intensity was shown as a function of both the voltage and the current being outputted from the power supply. The formaldehyde signal was recorded using lock-in detection. The goal was to determine ideal discharge conditions for formaldehyde and then try certain discharge conditions that were slightly under the ideal conditions for formaldehyde when searching for protonated formaldehyde. Decreasing the power should be more ideal in the production of protonated formaldehyde as only one hydrogen is being removed instead of two for the formation of formaldehyde. Unfortunately, when testing these conditions protonated formaldehyde was not detected as shown in Figure 4.8. The lock-in detection spectrum shown is just noise where signal should be for protonated formaldehyde. What was realized after a significant amount of testing was there were a number of

routes to produce formaldehyde. One route was through directly making it in the discharge and the other was through decomposition products. The signal using lock-in detection was capturing both types of production and as such, the target molecule had to be switched and instrumentation had to be developed in order to better detect pulsed discharge products.

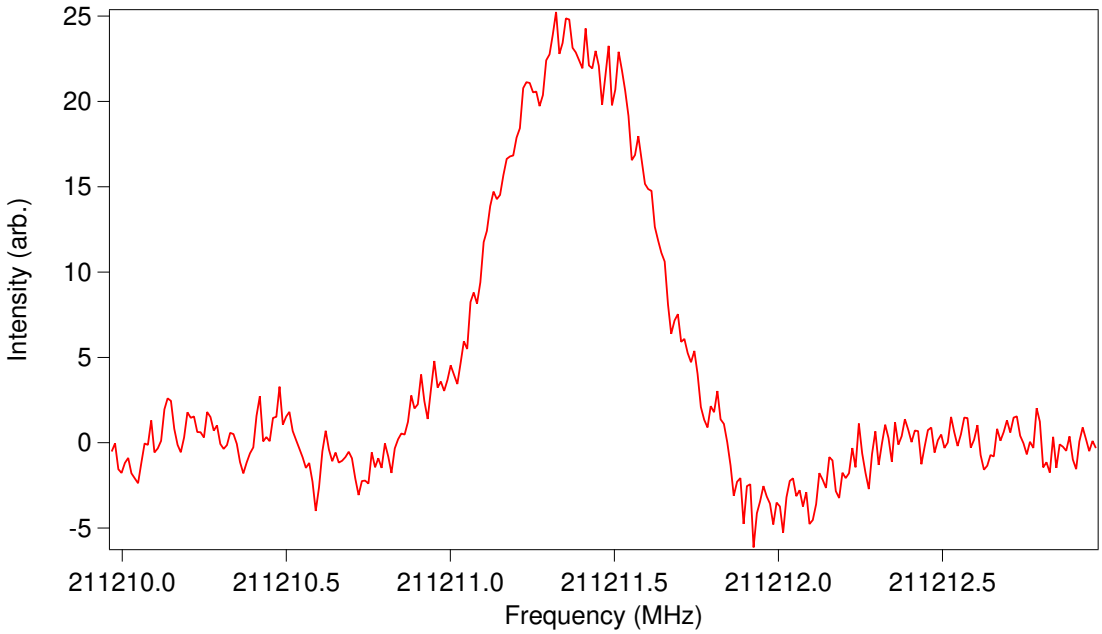

Figure 4.6: This is $3_{1,3} \leftarrow 2_{1,2}$ formaldehyde transition at 211211.468 MHz produced from a discharge of methanol in argon. The transition was recorded using lock-in detection with 60 averages. The sensitivity was set to 5 mv, the time constant was 30 ms, and the frequency step size was 0.01 MHz. The optical arrangement was a single-pass setup. The asymmetry in the line is do to the Doppler effect.

It would be ideal to only detect the direct discharge products and not also detect the decomposition product. This goal led to the development of PVTLI, which has been described in detail previously. This was initially characterized using formaldehyde as shown in Figure 4.9. While it was possible to detect formaldehyde at high sensitivity and fewer averages using this technique, it is still a stable discharge product. Therefore, it was necessary to switch to detecting the methoxy radical instead of formaldehyde. The idea is to now change the discharge parameters in order maximize the production of the methoxy radical as a potential tracer for the protonated

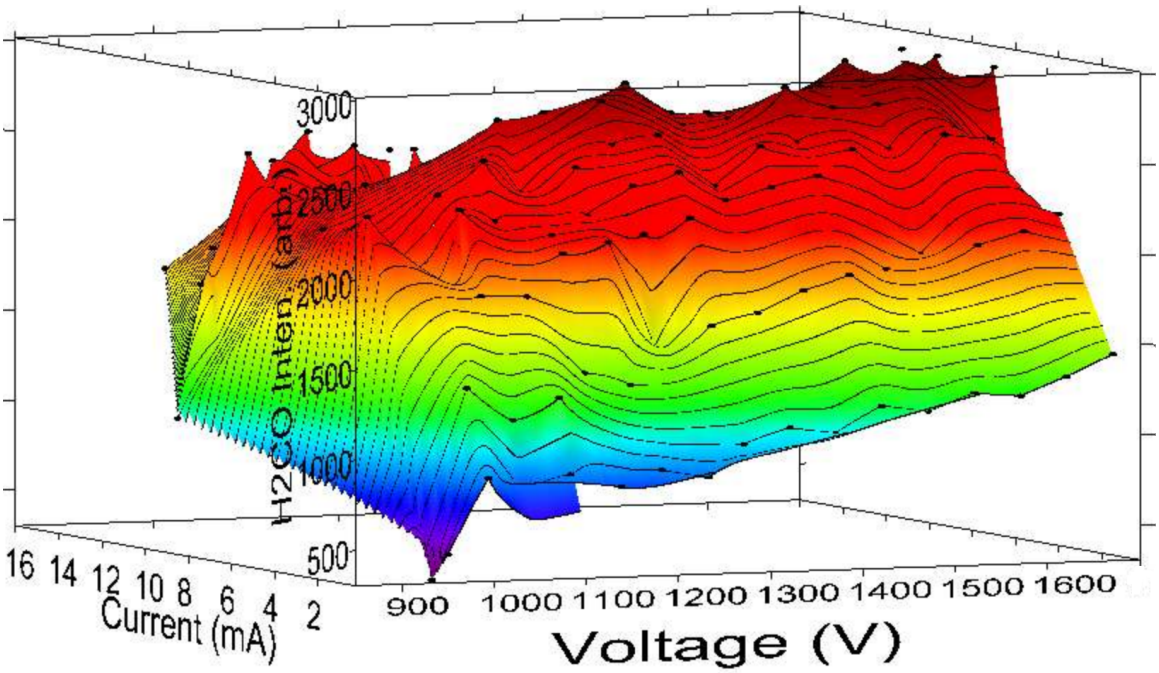

Figure 4.7: This is $3_{1,3} \leftarrow 2_{1,2}$ formaldehyde transition at 211211.468 MHz was recorded using lock-in detection with 2 averages produced from a discharge of methanol in argon. The resolution was set to 10 mv, the time constant was 30 ms, and the frequency step size was 0.01 MHz. The X-axis is the voltage, the Y-axis is the current and the Z-axis is the peak intensity of the formaldehyde line. The voltage was adjusted using the high voltage power supply, while the current was adjusted by changing the ballast resistors.

formaldehyde ion. This was a very similar problem that was previously encountered when producing a methanol plasma as they were also initially using formaldehyde as the target molecule [148]. Their solution was to use double-lock-in modulation to detect the methoxy radical signal, while PVTLI was used in this work. The initial attempts to detect the methoxy radical utilized standard lock-in detection, but due to the low duty cycle only noise was recorded. Once the detection method was changed to PVTLI, the methoxy radical signal was detected as displayed in Figure 4.10. The needle electrode discharge source was discovered to be particularly good at producing radicals in the course of these experiments. This has generated a number of new experiments into the production of different radicals, but those experiments are a part of the thesis work of my fellow graduate student Connor Wright and thus

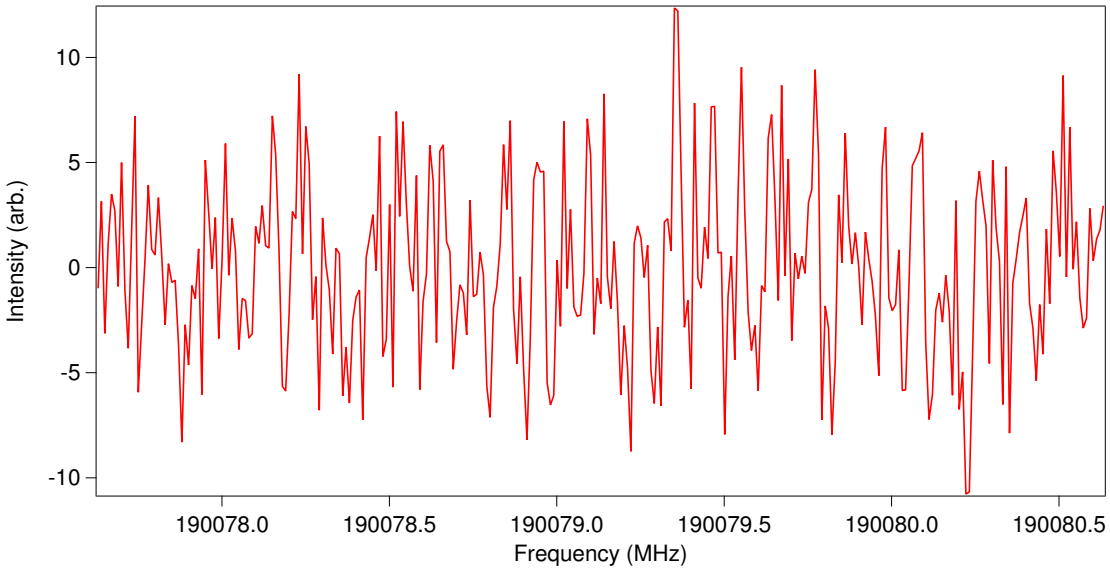

Figure 4.8: The $3_{0,3} \leftarrow 2_{0,2}$ protonated formaldehyde transition recorded at 190079.131 MHz using lock-in detection with 300 averages with a single-pass setup. The sensitivity was set to 5 mv, the time constant was 30 ms, and the frequency step size was 0.01 MHz.

will not be discussed in this body of work.

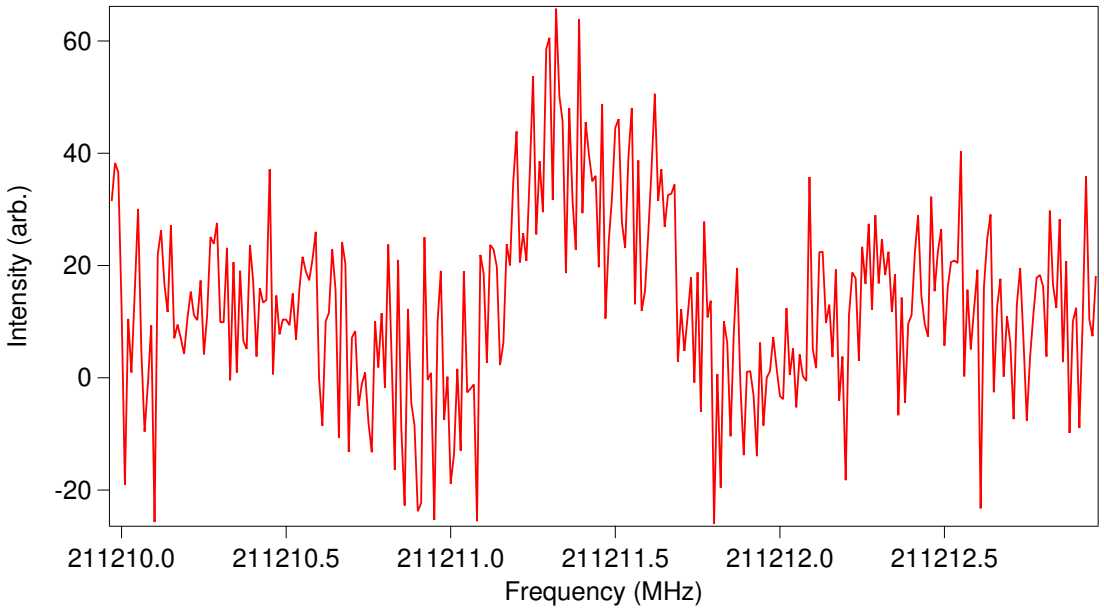

Figure 4.9: The $3_{1,3} \leftarrow 2_{1,2}$ formaldehyde transition at 211211.468 MHz. The transition was recorded in band 5 using PVTLI with 20 averages. The sensitivity was set to 100 mv, the time constant was 100 μs, and the frequency step size was 0.01 MHz. The optical arrangement was a single-pass setup.

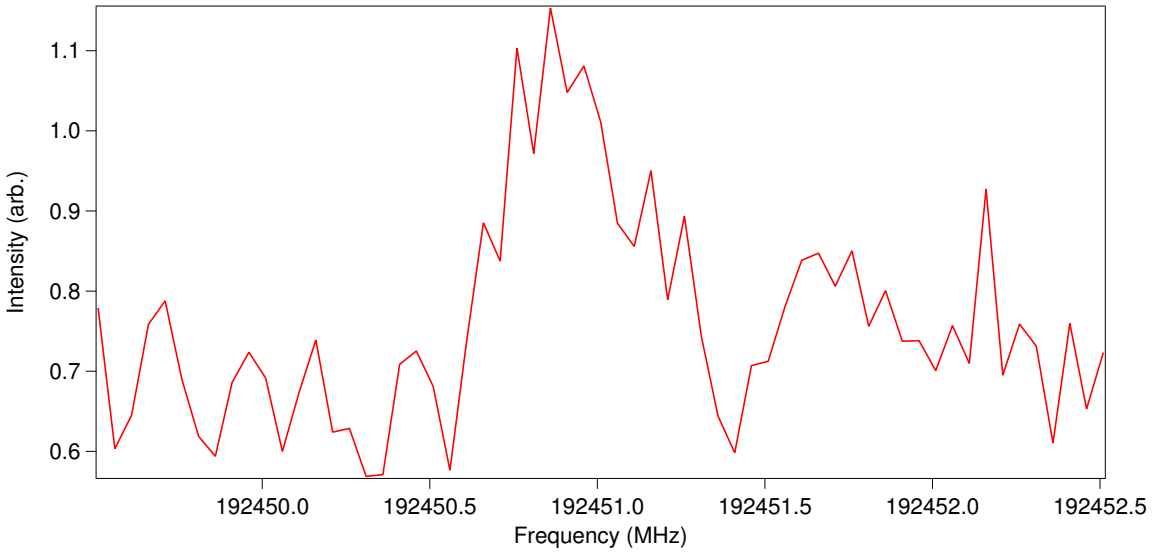

Figure 4.10: The $3_1, 0, 0, 5 \leftarrow 2_{-1}, 0, 0, 4$ methoxy radical transition recorded at 192451.014 MHz using lock-in detection with 4000 averages with a single-pass setup. The sensitivity was set to 100 mv, the time constant was 100 μs, and the frequency step size was 0.05 MHz. The increase in step size was done in order to speed up data collection. The labeled quanta are N_K, v, t, F

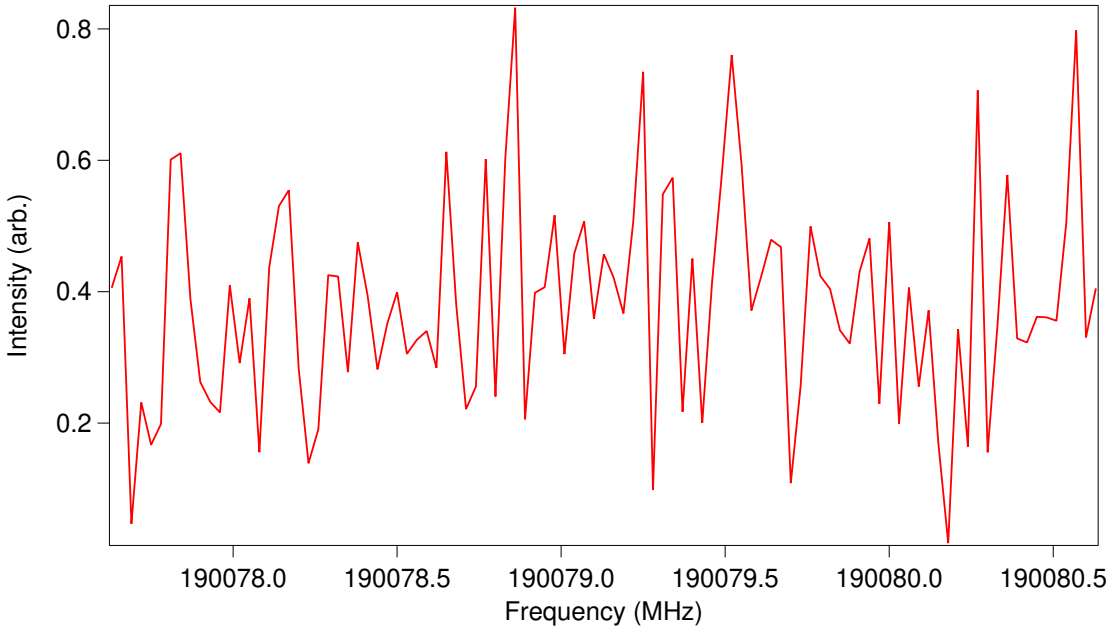

Figure 4.11: The $3_{0,3} \leftarrow 2_{0,2}$ protonated formaldehyde transition recorded at 190079.131 MHz using lock-in detection with 1500 averages with a single-pass setup. The sensitivity was set to 100 mv, the time constant was 100 μs, and the frequency step size was 0.03 MHz. The increase in step size was done in order to speed up data collection.

With the ability to detect the methoxy radical, the discharge parameters were adjusted to maximize its production. Once these adjustments were completed, the scanning frequency was changed to scan for protonated formaldehyde as seen in Figure 4.11. Sadly, the success in producing radicals with the needle electrode source did not translate into success in producing protonated formaldehyde. Based on the signal intensity of the methoxy radical when averaged for 4000 averages, it was determined that if protonated formaldehyde was detected with a SNR of roughly 3 it would require around 1000 averages to do so. Recording each of these thousand average scans took about eight hours to complete, thus requiring a lot of time trying to find the right parameters that could produce protonated formaldehyde. In the end, it was decided that attempts to produce protonated formaldehyde in a supersonic expansion discharge source would be put on hold until a quadrupole mass spectrometer was installed. This would allow for the real time detection of ions and thus the ideal discharge conditions could be easily determined in a single day versus weeks of changing a single parameter and then scanning all day for a non-detection. With the decision to wait until a quadrupole mass spectrometer was installed, the last available way to produce protonated formaldehyde was to utilize a hollow cathode.

4.3 Protonated Formaldehyde in a Hollow Cathode

The previous ways protonated formaldehyde were produced was in either in a negative glow discharge or a hollow cathode [27, 104–106]. By returning to what has previously been done, the goal of producing this ion as a stepping stone towards protonated methanol was put on hold. In preparation to run further experiments with the hollow cathode a few upgrades were first introduced and then the hollow cathode was characterized using HCO^+. The cathode originally had a cross-joint where on three separate view-ports the gas lines, cooling lines, and Teflon windows were introduced. This resulted in about 30 cm of dead space where the THz light

would not be interacting with sample. In order to reduce this dead space, the three separate view-ports were condensed into a single flange. This flange reduced the dead space to about 5 cm and fastened the THz view-port onto the flange instead of just being clamped on to the vacuum chamber. The rear view-port was also upgraded so the THz view-port would be bolted to the flange instead of being clamped on.

In order to test the protonation ability of the hollow cathode, it was decided to attempt to produce HCO^+ as done with the ring electrode source. The HCO^+ was produced in the cathode using hydrogen gas (Nexair, ultra-high purity) at 20 PSIG, and was metered by a 100 sccm flow controller (MKS 1179A) set to 10 sccm. A 10% carbon monoxide (Matheson) in helium (Nexair, ultra-high purity) gas mixture was prepared. This mixture was set at 20 PSIG, and was metered by a 100 sccm flow controller (MKS 1179A) set to 60 sccm. The gases were mixed together and then flowed into the cathode. The pressure of the mixed gas was controlled using a needle valve in order to maintain pressure around 25 mTorr. The cathode was cooled using liquid nitrogen (Nexair) that was continuously circulated throughout it. The anode was cooled to -35 °C by a chilled ethylene glycol recirculator (Super RMT Lauda Brinkmann, model RM6). With the cathode and anode appropriately cooled, the discharge was struck. The high voltage power supply (Spellman, SL2PN2000) was set to ∼200 V and 150-200 mA. The detection method used was standard lock-in detection as shown in Figure 4.12. With this detection, it was confirmed that the protonation reaction was possible using these parameters and thus the next step was to produce protonated formaldehyde.

Using hydrogen gas (Nexair, ultra-high purity) at 20 PSIG, and metering by a 100 sccm flow controller (MKS 1179A) set to 10 sccm, the gas flowed over paraformaldehyde powder (Alfa Aesar, paraformaldehyde 97%). The powder was inserted into the gas line that had copper mesh blocking the powder from being pulled into the vacuum chamber. The metal fitting was heated to roughly 50 °C using heating tape

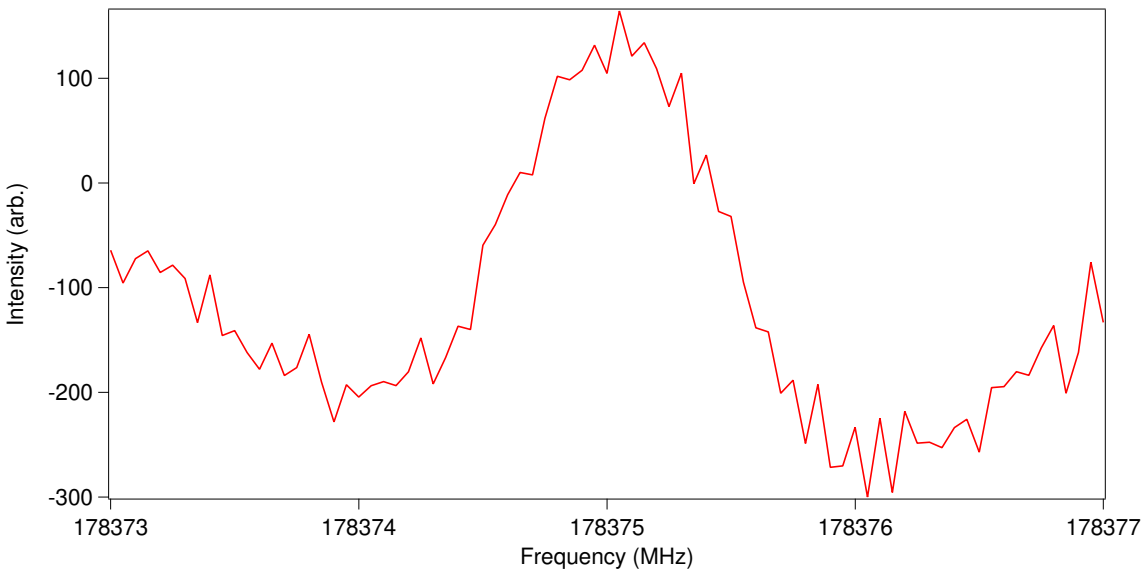

Figure 4.12: The 2 ← 1 formylium transition recorded at 178375.056 MHz using lock-in detection with 10 averages. The sensitivity was set to 2 mv, the time constant was 10 ms, and the frequency step size was 0.05 MHz. The increase in step size was done in order to speed up data collection.

in order to introduce formaldehyde gas. The mixture of formaldehyde and hydrogen were then flowed into the cathode. Again a needle valve was used to control the pressure of the gases to around 25 mTorr. Going above 35 mTorr pressure would result in pressure broadening. Initially, the cathode was cooled using continuously circulating liquid nitrogen (Nexair). The anode was cooled by a chilled ethylene glycol recirculator (Super RMT Lauda Brinkmann, model RM6) set to a temperature of to -35 °C. With the cathode and anode appropriately cooled, the discharge was struck. The high voltage power supply (Spellman, SL2PN2000) was set to ∼200 V and 150-200 mA. Lock-in detection was used to detect the discharge products.

The initial scan for formaldehyde was conducted while there was no discharge present. This was done to provide a baseline intensity for formaldehyde before the discharge source was lit as shown in Figure 4.14. With the liquid nitrogen cooling being applied, the formaldehyde signal was much lower than at room temperature signal. This was due to formaldehyde freezing on the cooling lines as the temperature

of the cooling lines were at 77 K. As such, there was a large decrease of formaldehyde in the gas phase, meaning the number density of protonated formaldehyde was also decreased. When attempting to detect protonated formaldehyde, as seen in Figure 4.14, only noise was recorded. This meant that the cooling for the cathode had to be changed. In Amano's paper, they used a chilled methanol (-60 °C) recirculator to cool their cathode [27].

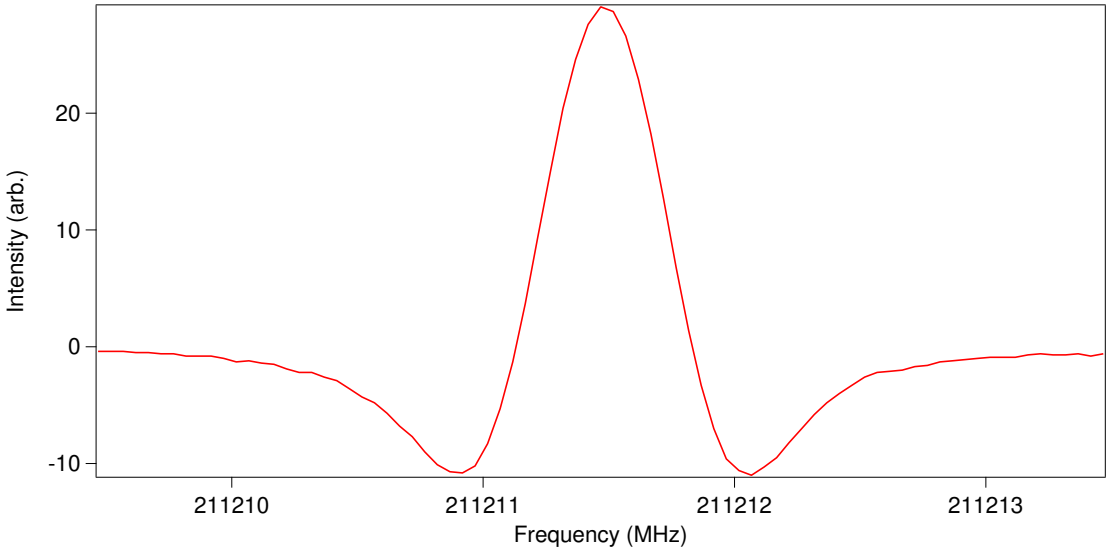

Figure 4.13: The $3_{1,3} \leftarrow 2_{1,2}$ formaldehyde transition at 211211.468 MHz. The transition was recorded sing lock-in detection with 10 averages. The sensitivity was set to 10 mv, the time constant was 10 ms, and the frequency step size was 0.05 MHz.

With this guidance, the cathode was refitted in order to be cooled with a recirculator. A second chilled ethylene glycol recirculator (PolyScience 950 Refrigerated Circulator) was set to -35 °C, and was then attached to the cathode. Ethylene glycol was used instead of methanol as it was inclusive if the recirculator could safely utilize methanol. The same formaldehyde line was recorded as before in order to compare with the liquid nitrogen cooling as seen in Figure 4.15. The signal was much more intense due to the formaldehyde not being frozen on the cooling lines. Once this was done, another attempt to produce protonated formaldehyde in the cathode was made. This time it looked like there was protonated formaldehyde in the initial scans,

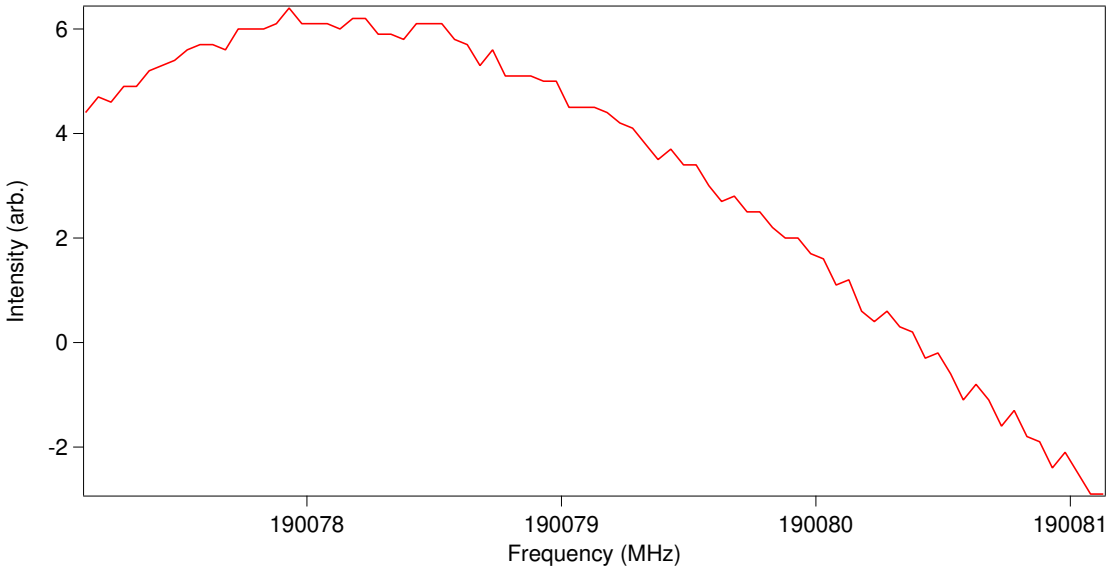

Figure 4.14: A non-detection of the $3_{0,3} \leftarrow 2_{0,2}$ protonated formaldehyde transition recorded at 190079.131 MHz using lock-in detection with 200 averages. The sensitivity was set to 10 mv, the time constant was 10 ms, and the frequency step size was 0.05 MHz. All that can be seen is the standing wave created by the viewports for the cathode.

but as the discharge was running it caused the cathode to heat up. As it heated up, the discharge got weaker and weaker, until the point where the discharge stopped running because it was too hot. The results of these scans are shown in Figure 4.16. The cathode overheated and shut off due to the output pressure of the ethylene glycol recirculator being used. When cooling with liquid nitrogen, high pressure liquid nitrogen tanks are used with the output pressure set to approximately 200 PSIG. In comparison, the recirculators only have an output pressure of a few PSIG. This means while there was some flow of chilled ethylene glycol, there was not sufficient flow to actually maintain the set temperature as the discharge was running. This meant that the production of protonated formaldehyde cannot be sustained over the long time scales that are necessary to produce a spectrum through the entire range of 50-1000 GHz.

Again, detecting protonated formaldehyde was nearly achieved, but due to the the lack of necessary equipment, it was unsuccessful. These experiments pushed the

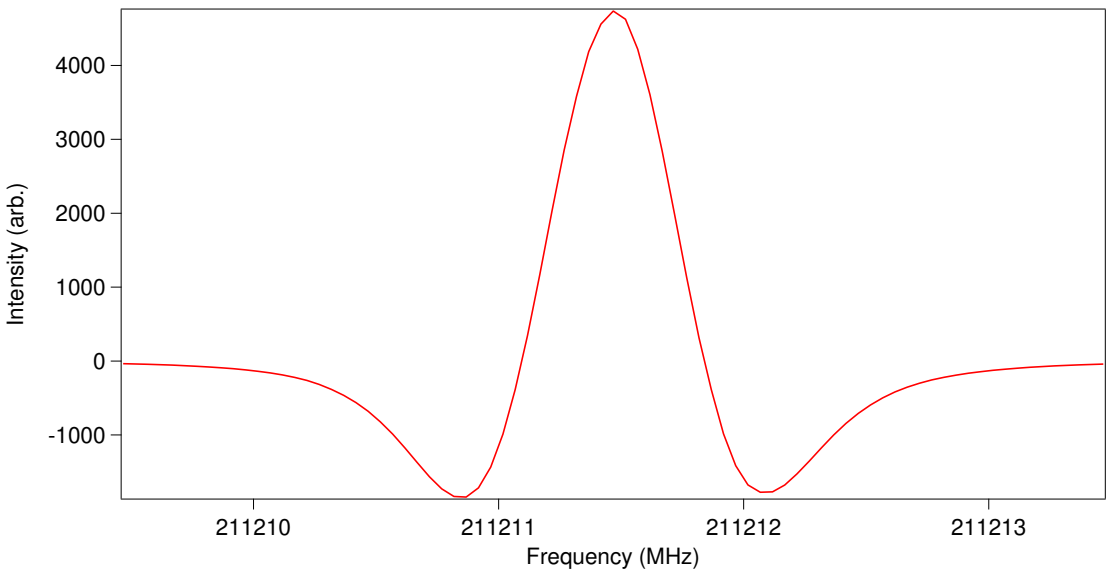

Figure 4.15: 10 avg, 200 mv, 10 ms, 0.05 MHz, Lock-in The $3_{1,3} \leftarrow 2_{1,2}$ formaldehyde transition at 211211.468 MHz. The transition was recorded using lock-in detection with 10 averages. The sensitivity was set to 200 mv, the time constant was 10 ms, and the frequency step size was 0.05 MHz.

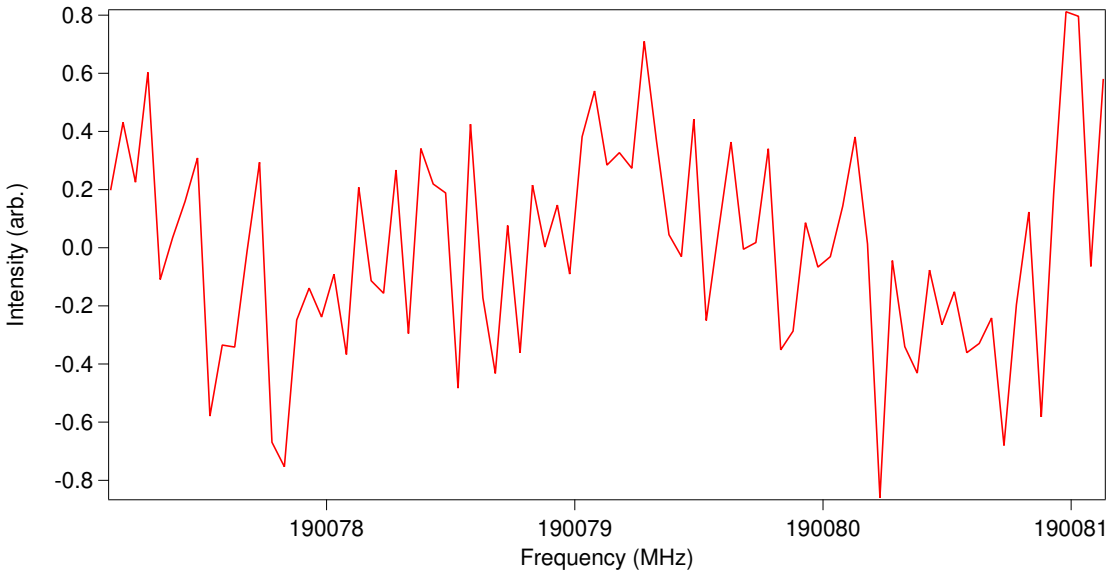

Figure 4.16: The $3_{0,3} \leftarrow 2_{0,2}$ protonated formaldehyde transition recorded at 190079.131 MHz using lock-in detection with 1002 averages. The sensitivity was set to 10 mv, the time constant was 10 ms, and the frequency step size was 0.05 MHz.

equipment to its limits both with the hollow cathode and with the pulsed discharge experiments. The pulsed discharge production of protonated formaldehyde set a lab record for the lowest detected absorption coefficient, demonstrating this was a difficult

experiment and the goals for this work were incredibly high. There is still hope to produce protonated formaldehyde and protonated methanol, but a few necessary adjustments are required.

4.4 Future Outlook on Protonated Formaldehyde

While the initial results were promising, the spectrum of protonated formaldehyde was continuously just out of reach. Despite not being able to produce and record the full rotational spectrum of protonated formaldehyde, all three of these experiments provided the lab with great insight on how to proceed going forward with protonated formaldehyde and with the eventual goal of protonated methanol. We now understand it is possible to produce protonated formaldehyde in a supersonic expansion source and that the hollow cathode can likely produce it as well, though both types of discharge sources require additional upgrades in order to get this project over the finish line. With regards to the pulsed discharge sources, a mass spectrometer is a must. This addition would allow for the real time detection of ions and thus allow for discharge parameters to be quickly tested and the ion signal detected and production optimized. In addition to the mass spectrometer, an ion trap would be another ideal addition to this experiment. This would allow for the build up of number density of the ion of interest, thus increasing the number of absorbers present over the number produced in the pulsed discharge. These two additions would likely be enough to detect protonated formaldehyde and record its rotational spectrum in higher frequency than previous works recorded. These upgrades would also be incredibly useful for protonated methanol and any other ion targets. With the hollow cathode, the simple addition of a high pressure recirculator should be sufficient to produce protonated formaldehyde in the hollow cathode. This would give the lab the ability to target other complex organic ions for production in the cathode and should be significantly cheaper to purchase than the upgrades required for the pulsed

discharge experiments. With that being said, it would be ideal to upgrade both types of discharge sources, thus gaining additional capabilities for them.

Chapter 5 Methanol-Argon Clusters

Over the course of working with protonated formaldehyde it was discovered that additional lines were being detected. None of these new lines matched the frequencies of previously-recorded molecules listed in the public spectroscopy databases. These unassigned lines were believed to have been caused by a weakly-bound cluster involving methanol. Such clusters are commonly observed in supersonic expansions, especially those using argon as the carrier gas. These clusters need to be investigated in order to minimize the number of unassigned lines when attempting to produce protonated methanol. Identification of the lines arising from clusters would allow one to focus on discharge product lines that could be protonated methanol instead of a methanol cluster.

The first detected line of this type is shown in Figure 5.1. It has been observed in both fast sweep scans and PVTLI scans. Considering that the only chemicals being used were methanol, argon, and the ever-present water, it was possible to predict the cause of this unassigned line. Since it was not a methanol line, it had to be a cluster of either methanol-argon, methanol-water, methanol dimer, water-argon, or water dimer. The water-argon and water dimer clusters are well characterized in this regime [154, 155], leaving the methanol clusters as the most likely carriers. In order to establish which possible cluster was producing this line, the carrier gas was changed from argon to helium. Using the fast-sweep data acquisition method, two spectra were collected centered on the unassigned line. The first spectrum was of methanol in argon gas and the second was methanol in helium gas. The results of this experiment are shown in Figure 5.2. A line is present at 145135.793 MHz when argon is present, but when the backing gas was switched to helium the signal disappeared. This suggests that this unknown line is caused by the argon-methanol

cluster. This does not mean that there are not additional lines being produced by with methanol-water or methanol-methanol clusters, but it does confirm the presence of argon-methanol.

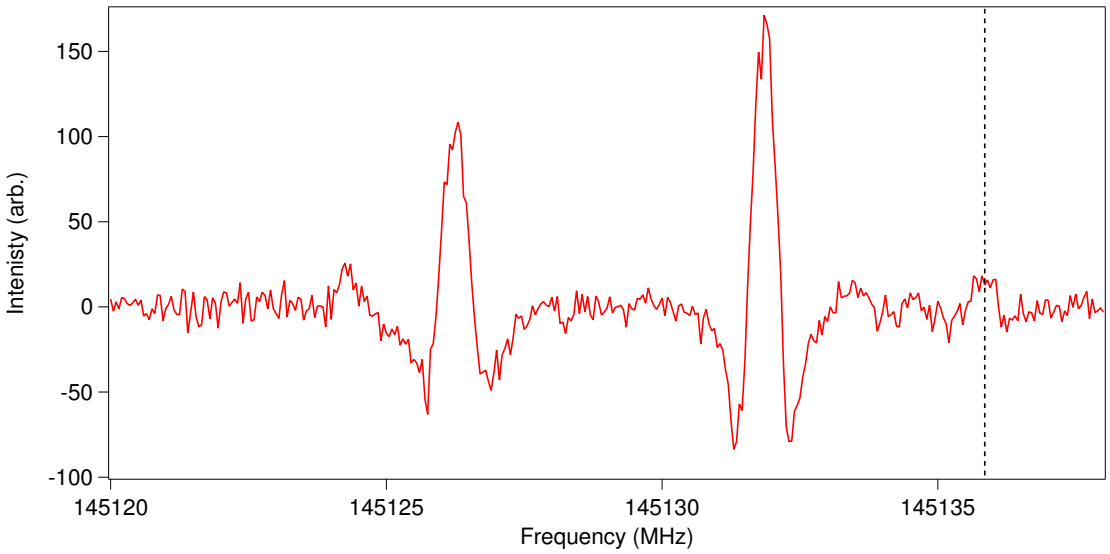

Figure 5.1: The first recording on the unknown line at 145135.793 MHz using fast sweep. The Frequency window scanned was 145120-145138 MHz with 5 averages with a spectral resolution of 50 kHz. The pulsed valve and scanning repetition rate was held at 20 Hz. The dashed black line delineates the location of the unassigned line.

5.1 Argon-Methanol Cluster Instrumentation

With the establishment that argon-methanol is present in the system, it was decided to optimize the setup in order to increase the production of the cluster. The optimized conditions are given below and were used for the duration of the experiment. To produce argon-methanol, argon gas (Nexair, ultra-high purity) flowed through liquid methanol (Fisher Scientific 99.9%) at 250 psig. The gas mixture supersonically expanded in the the chamber through a pulsed valve (Parker Hannifin, Series 9 general valve, 1 mm pinhole) set at a repetition rate of 10 Hz. The pulse width was set to 0.5-1 ms depending on pulse valve conditions, which resulted in operating pressures of roughly 35 mTorr. Below the pulsed valve was a set of spherical

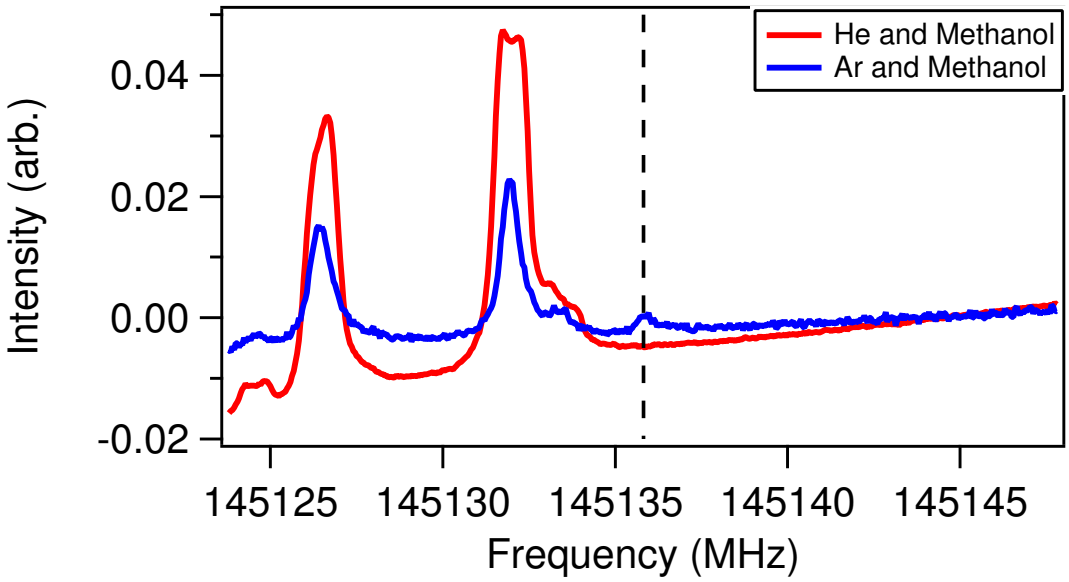

Figure 5.2: Two fast sweep scans were recorded with the backing gas for the blue trace was argon and in the red trace the backing gas was helium. It is plainly shown that the line at 145135.793 MHz is present when using argon, but is not present when using helium as the backing gas. This supports the conclusion that the spectral lines are produced by an argon-methanol cluster. The dashed black line delineates the location of the unassigned line.

mirrors (Edmund Optics, 15.24 cm diameter and 15.24 cm focal length, NT32-836) that formed a seven-pass optical cavity of millimeter/submillimeter radiation; this optical cavity probed the expansion approximately 6 cm from the pinhole of the valve. The millimeter/submillimeter radiation was produced using a signal generator (Agilent Technologies, E8257D PSG with 1EA, UNU, 550, and UNT options) and then multiplied to the appropriate probe frequency in the range of 50 GHz to 1 THz using a frequency multiplier chain (Virginia Diodes Inc., S197(c)). An InSb hot electron bolometer (QMC Ltd., QFI/2BI) was used as the detector for the millimeter/submillimeter beam. The output signal from the detector was recorded using a digital oscilloscope (National Instruments, PCI-5124) when using the fast sweep technique. For the PVTLI technique, the output of the bolometer is routed into a lock-in amplifier (Stanford Research Systems, Model SR 830 DSP), and then the processed signal from the lock-in is collected using a digital oscilloscope (National Instruments,

PCI-5124).

5.2 Argon-Methanol Cluster Results and Discussion

The first objective after optimizing for the production of argon-methanol was to complete a fast sweep band scan across band 5 which covers the 130-225 GHz frequency range. Each fast sweep segment had a frequency width of 24 MHz, a frequency resolution of 48 kHz, and 2000 averages. The data acquisition rate was held at 10 Hz for every scan. The scanning started at 130 GHz and stepped across frequency until reaching 225 GHz. The fast sweep scans were stitched together in order to produce the band scan shown in Figure 5.3. Once the band scan was recorded, spectral features were identified by eye through examination of the spectra. A global line list was made and then compared to known spectral lines for methanol using Splatalogue, a spectral line catalog provided by the National Radio Astronomy Observatory (NRAO) [156]. Once a final line list was compiled with only unassigned lines, they were then rescanned using PVTLI to obtain accurate line center frequencies.. Each PVTLI scan was produced using a modulation frequency of 50 kHz, a modulation deviation of 75 kHz, a time constant of 100 μs, and a frequency step size of 10 kHz. The sensitivity of each measurement was adjusted for the strength of the line, but was primarily set to 5 mV. After each dataset of time, intensity, and frequency was obtained, it was then integrated over the time when signal was present in order to produce a intensity versus frequency like that spectrum shown in Figure 5.4. Once each scan was recorded, a 2nd harmonic Gaussian line shape was fit to the spectral feature and the line center determined using the fit.

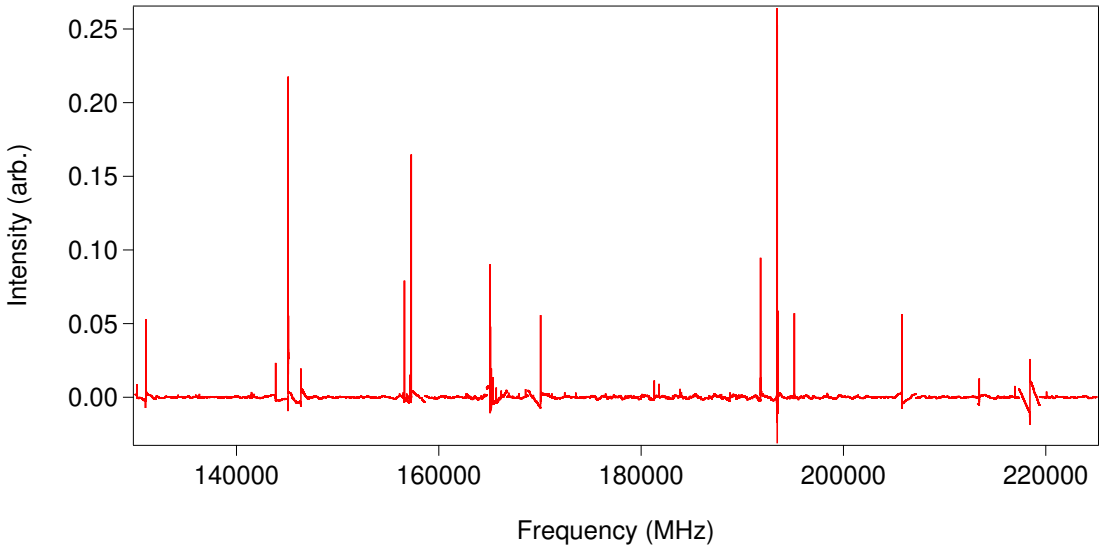

Figure 5.3: The band scan across 130-225 GHz using the fast sweep technique. These scans were not altered to have a consistent baseline. The slight shifts in baselines are likely due to small changes in power over the scanning window.

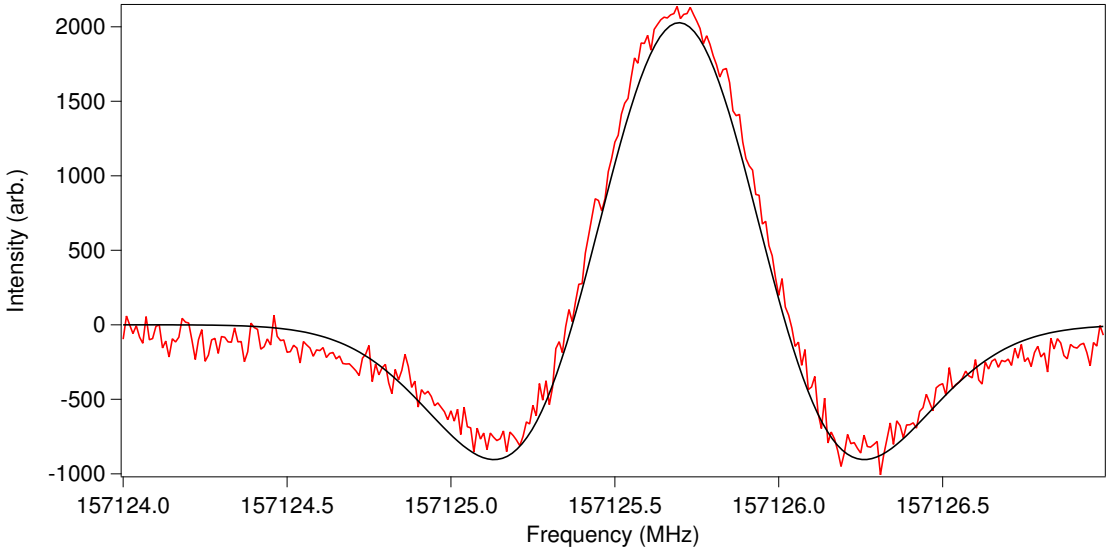

Figure 5.4: Here is an example of a PVTLI detection with 50 averages in the red trace. The sensitivity was set to 5 mV, the time constant was 100 μs, and the frequency step size was 10 kHz. The black trace is the second derivative fit for a Gaussian line shape. The line center of the fit was then used for the fit of the argon-methanol cluster.

Table 5.1: Argon-Methanol Transition Frequencies. Those with a * are microwave transitions that were previously reported.

Quantum Number	Transition Frequency (MHz)
$2_{1,2}$ - $1_{1,1}$	7869.510 0.004*
$2_{0,2}$ - $1_{0,1}$	8024.317 0.004*
$2_{1,1}$ - $1_{1,0}$	8177.627 0.004*
$2_{1,2}$ - $3_{0,3}$	11196.477 0.004*
$3_{1,3}$ - $2_{1,2}$	11802.616 0.004*
$3_{2,2}$ - $2_{2,1}$	12027.348 0.004*
$3_{2,1}$ - $2_{2,0}$	12030.316 0.004*
$3_{0,3}$ - $2_{0,2}$	12033.307 0.004*
$3_{1,2}$ - $2_{1,1}$	12264.588 0.004*
$1_{1,1}$ - $2_{0,2}$	15360.274 0.004*
$4_{1,4}$ - $3_{1,3}$	15733.740 0.004*
$4_{3,2}$ - $3_{3,1}$	16020.544 0.004*
$4_{3,1}$ - $3_{3,0}$	16020.556 0.004*
$4_{2,3}$ - $3_{2,2}$	16033.511 0.004*
$4_{0,4}$ - $3_{0,3}$	16038.498 0.004*
$4_{2,2}$ - $3_{2,1}$	16040.936 0.004*
$4_{1,3}$ - $3_{1,2}$	16349.332 0.004*
$5_{1,5}$ - $4_{1,4}$	19662.231 0.004*
$5_{2,4}$ - $4_{2,3}$	20037.146 0.004*
$5_{0,5}$ - $4_{0,4}$	20038.630 0.004*
$5_{2,3}$ - $4_{2,2}$	20051.967 0.004*
$5_{1,4}$ - $4_{1,3}$	20431.106 0.004*
$1_{1,0}$ - $1_{0,1}$	23538.693 0.004*
$6_{1,6}$ - $5_{1,5}$	23587.435 0.004*
$2_{1,1}$ - $2_{0,2}$	23692.002 0.004*
$3_{1,2}$ - $3_{0,3}$	23923.277 0.004*
$6_{0,6}$ - $5_{0,5}$	24032.458 0.004*
$4_{1,3}$ - $4_{0,4}$	24234.108 0.004*
$6_{1,5}$ - $5_{1,4}$	24509.165 0.004*
$14_{3,12}$ - $15_{1,15}$	136328.262 0.010
$6_{3,4}$ - $5_{2,3}$	141179.806 0.010
$6_{3,3}$ - $5_{2,3}$	141179.806 0.010
$6_{3,4}$ - $5_{2,4}$	141205.929 0.010
$6_{3,3}$ - $5_{2,4}$	141205.929 0.010
$12_{3,10}$ - $13_{1,13}$	142284.698 0.010
$7_{3,5}$ - $6_{2,4}$	145135.793 0.010
$7_{3,4}$ - $6_{2,4}$	145135.793 0.010
$7_{3,4}$ - $6_{2,5}$	145188.153 0.010
$7_{3,5}$ - $6_{2,5}$	145188.153 0.010

Continued on next page

Table 5.1 – *Continued from previous page*

Quantum Number	Transition Frequency (MHz)
$8_{3,6}$ - $7_{2,5}$	149073.859 0.010
$8_{3,5}$ - $7_{2,5}$	149073.859 0.010
$8_{3,5}$ - $7_{2,6}$	149168.093 0.010
$8_{3,6}$ - $7_{2,6}$	149168.093 0.010
$14_{5,10}$ - $15_{4,11}$	150268.262 0.010
$14_{5,9}$ - $15_{4,11}$	150268.262 0.010
$14_{5,10}$ - $15_{4,12}$	150268.262 0.010
$14_{5,9}$ - $15_{4,12}$	150268.262 0.010
$17_{2,15}$ - $16_{1,16}$	150359.973 0.010
$9_{3,7}$ - $8_{2,6}$	152989.743 0.010
$9_{3,6}$ - $8_{2,7}$	153146.822 0.010
$10_{3,8}$ - $9_{2,7}$	156878.743 0.010
$10_{3,7}$ - $9_{2,8}$	157125.698 0.010
$11_{3,9}$ - $10_{2,8}$	160735.833 0.010
$11_{3,8}$ - $10_{2,9}$	161106.232 0.010
$13_{4,10}$ - $13_{3,10}$	163476.882 0.010
$13_{4,9}$ - $13_{3,10}$	163476.882 0.010
$13_{4,10}$ - $13_{3,11}$	163493.758 0.010
$13_{4,9}$ - $13_{3,11}$	163493.758 0.010
$12_{4,9}$ - $12_{3,10}$	163576.183 0.010
$12_{4,8}$ - $12_{3,10}$	163576.183 0.010
$11_{4,8}$ - $11_{3,8}$	163644.213 0.010
$11_{4,7}$ - $11_{3,8}$	163644.213 0.010
$11_{4,8}$ - $11_{3,9}$	163650.578 0.010
$11_{4,7}$ - $11_{3,9}$	163650.578 0.010
$10_{4,7}$ - $10_{3,7}$	163713.593 0.010
$10_{4,6}$ - $10_{3,7}$	163713.593 0.010
$10_{4,7}$ - $10_{3,8}$	163717.232 0.010
$10_{4,6}$ - $10_{3,8}$	163717.232 0.010
$8_{4,5}$ - $8_{3,5}$	163827.504 0.010
$8_{4,4}$ - $8_{3,5}$	163827.504 0.010
$8_{4,5}$ - $8_{3,6}$	163828.537 0.010
$8_{4,4}$ - $8_{3,6}$	163828.537 0.010
$7_{4,4}$ - $7_{3,4}$	163873.683 0.010
$7_{4,3}$ - $7_{3,4}$	163873.683 0.010
$7_{4,4}$ - $7_{3,5}$	163873.683 0.010
$7_{4,3}$ - $7_{3,5}$	163873.683 0.010
$6_{4,3}$ - $6_{3,3}$	163912.668 0.010
$6_{4,2}$ - $6_{3,3}$	163912.668 0.010
$6_{4,3}$ - $6_{3,4}$	163912.668 0.010
$6_{4,2}$ - $6_{3,4}$	163912.668 0.010
$5_{4,2}$ - $5_{3,2}$	163945.496 0.010

Continued on next page

Table 5.1 – *Continued from previous page*

Quantum Number	Transition Frequency (MHz)
$5_{4,1}$ - $5_{3,2}$	163945.496 0.010
$5_{4,1}$ - $5_{3,3}$	163945.496 0.010
$5_{4,2}$ - $5_{3,3}$	163945.496 0.010
$12_{3,10}$ - $11_{2,9}$	164555.397 0.010
$12_{3,9}$ - $11_{2,10}$	165090.153 0.010
$13_{3,11}$ - $12_{2,10}$	168331.593 0.010
$13_{3,10}$ - $12_{2,11}$	169079.543 0.010
$14_{3,11}$ - $13_{2,12}$	173076.619 0.010
$19_{4,15}$ - $18_{0,18}$	175452.574 0.010
$15_{3,12}$ - $14_{2,13}$	177083.848 0.010
$19_{8,12}$ - $20_{7,13}$	177105.213 0.010
$19_{8,11}$ - $20_{7,13}$	177105.213 0.010
$19_{8,12}$ - $20_{7,14}$	177105.213 0.010
$19_{8,11}$ - $20_{7,14}$	177105.213 0.010
$4_{4,0}$ - $3_{3,0}$	179992.957 0.010
$4_{4,1}$ - $3_{3,0}$	179992.957 0.010
$4_{4,0}$ - $3_{3,1}$	179992.957 0.010
$4_{4,1}$ - $3_{3,1}$	179992.957 0.010
$18_{6,13}$ - $19_{7,12}$	180996.333 0.010
$18_{6,12}$ - $19_{7,12}$	180996.333 0.010
$18_{6,13}$ - $19_{7,13}$	180996.333 0.010
$18_{6,12}$ - $19_{7,13}$	180996.333 0.010
$16_{3,14}$ - $15_{2,14}$	181035.533 0.010
$16_{3,13}$ - $15_{2,14}$	181104.003 0.010
$5_{4,1}$ - $4_{3,1}$	183968.093 0.010
$5_{4,2}$ - $4_{3,1}$	183968.093 0.010
$5_{4,2}$ - $4_{3,2}$	183968.093 0.010
$5_{4,1}$ - $4_{3,2}$	183968.093 0.010
$6_{4,3}$ - $5_{3,2}$	187935.097 0.010
$6_{4,2}$ - $5_{3,2}$	187935.097 0.010
$6_{4,3}$ - $5_{3,3}$	187935.097 0.010
$6_{4,2}$ - $5_{3,3}$	187935.097 0.010
$20_{6,14}$ - $21_{4,17}$	188925.003 0.010
$18_{3,16}$ - $17_{2,16}$	189026.773 0.010
$7_{4,4}$ - $6_{3,3}$	191893.322 0.010
$7_{4,3}$ - $6_{3,3}$	191893.322 0.010
$7_{4,4}$ - $6_{3,4}$	191893.322 0.010
$7_{4,3}$ - $6_{3,4}$	191893.322 0.010
$15_{6,9}$ - $16_{5,11}$	192854.213 0.010
$15_{6,10}$ - $16_{5,11}$	192854.213 0.010
$15_{6,9}$ - $16_{5,12}$	192854.213 0.010
$15_{6,10}$ - $16_{5,12}$	192854.213 0.010

Continued on next page

Table 5.1 – *Continued from previous page*

Quantum Number	Transition Frequency (MHz)
$8_{4,5}$ - $7_{3,4}$	195841.953 0.010
$8_{4,4}$ - $7_{3,4}$	195841.953 0.010
$8_{4,5}$ - $7_{3,5}$	195841.953 0.010
$8_{4,4}$ - $7_{3,5}$	195841.953 0.010
$9_{4,6}$ - $8_{3,5}$	199779.677 0.010
$9_{4,5}$ - $8_{3,5}$	199779.677 0.010
$9_{4,6}$ - $8_{3,6}$	199780.729 0.010
$9_{4,5}$ - $8_{3,6}$	199780.729 0.010
$10_{4,7}$ - $9_{3,6}$	203706.079 0.010
$10_{4,6}$ - $9_{3,6}$	203706.079 0.010
$10_{4,7}$ - $9_{3,7}$	203708.069 0.010
$10_{4,6}$ - $9_{3,7}$	203708.069 0.010
$11_{4,8}$ - $10_{3,7}$	207619.812 0.010
$11_{4,7}$ - $10_{3,7}$	207619.812 0.010
$11_{4,8}$ - $10_{3,8}$	207623.510 0.010
$11_{4,7}$ - $10_{3,8}$	207623.510 0.010
$10_{5,5}$ - $10_{4,6}$	210357.138 0.010
$10_{5,6}$ - $10_{4,6}$	210357.138 0.010
$10_{5,5}$ - $10_{4,7}$	210357.138 0.010
$10_{5,6}$ - $10_{4,7}$	210357.138 0.010
$8_{5,3}$ - $8_{4,4}$	210490.202 0.010
$8_{5,4}$ - $8_{4,4}$	210490.202 0.010
$8_{5,3}$ - $8_{4,5}$	210490.202 0.010
$8_{5,4}$ - $8_{4,5}$	210490.202 0.010
$7_{5,2}$ - $7_{4,3}$	210545.307 0.010
$7_{5,3}$ - $7_{4,3}$	210545.307 0.010
$7_{5,2}$ - $7_{4,4}$	210545.307 0.010
$7_{5,3}$ - $7_{4,4}$	210545.307 0.010
$12_{4,9}$ - $11_{3,8}$	211519.728 0.010
$12_{4,8}$ - $11_{3,8}$	211519.728 0.010
$12_{4,9}$ - $11_{3,9}$	211526.198 0.010
$12_{4,8}$ - $11_{3,9}$	211526.198 0.010
$13_{4,10}$ - $12_{3,9}$	215404.408 0.010
$13_{4,9}$ - $12_{3,9}$	215404.408 0.010
$13_{4,10}$ - $12_{3,10}$	215415.179 0.010
$13_{4,9}$ - $12_{3,10}$	215415.179 0.010
$14_{4,11}$ - $13_{3,10}$	219272.548 0.010
$14_{4,10}$ - $13_{3,10}$	219272.548 0.010
$14_{4,11}$ - $13_{3,11}$	219289.743 0.010
$14_{4,10}$ - $13_{3,11}$	219289.743 0.010

5.2.1 Argon-Methanol Cluster Fit Utilizing SPFit

Once all lines were scanned and then processed in order to determine the line centers, the lines were then assigned using the SPFIT program in the CALPGM suite [157]. As noted in the previous work conducted on argon-methanol, both an A and E internal-rotor states are present for this cluster [133, 134]. A total of 133 new lines were added to the argon-methanol for the A state. At the time of this writing, only the A state lines have been successfully fit using the line list in Table 5.1 and a Watson A-reduced Hamiltonian in the I' representation with quartic, sextic, octic, and dodecic centrifugal distortion constants. The line list for the fit included the microwave transitions reported by Suenram *et al.* [133]. The parameters used to successfully fit these lines are displayed in Table 5.2. The uncertainty for the microwave transitions are reported by Suenram *et al.* to be 4 kHz and the uncertainty for the millimeter/submillimeter transitions were set to the frequency resolution of the scans, 10 kHz [133]. This is smaller than the RMS reported in the fit, which is 76.75 kHz. This discrepancy can be primarily contributed to the absence of proper terms to fit the internal motion in the argon-methanol cluster.

While SPFIT can successfully fit and predict most lines, the internal rotor terms were not included in the Hamiltonian, and therefore the A/E splitting was not modeled by the fit. The splitting arises from two sets of internal motion. The first set is caused by the methyl rotor and the second set is the rotation of the methanol molecule with respect to the argon atom [133]. There are a number of quartet features that have a predicted line centered on the quartet, indicating the A state fit is predictive despite lacking the necessary terms to model the splitting. Despite the lack of internal rotor analysis, this A state fit does provide quite useful information for this cluster. The highest level J observed is J = 20 with Ka = 8 and Kc = 16. The original microwave data only spanned the range of 7.8-24.5 GHz, while the added lines spanned from 130-225 GHz. It is interesting to note that the distortion constants

present across all three works are in relative good agreement.

There are still 39 unassigned lines discovered and confirmed with the fast sweep and PVTLI data. It is currently unknown if these lines belong to the argon-methanol cluster, to methanol-water, or to the methanol dimer. Using a program that is able to fit the E state lines for argon-methanol, like XIAM, will help finalize the fit for this cluster and elucidate what additional cluster the lines belong to. This additional fitting to include the internal rotor terms in the Hamiltonian is currently ongoing and was not completed in time for this dissertation. A subsequent article will soon be produced that will answer these questions. With the line list in its current state, it is still possible to compare these lines to unknown lines in other laboratory or astronomical data sets. The hope is that this work will be able to help assign some of these features as well as helping understand the chemistry occurring in methanol plasma when protonated methanol is finally attempted.

Table 5.2: Spectroscopic constants for the argon-methanol cluster with a comparison with previously reported constants from Suenram *et al.* and Tan *et al.*

Parameter	Suenram et al.	Tan at al.	This Work
A (MHz)	25,468.821(4)	25,505.286(33)	25,470.22840(290)
B (MHz)	2,084.42(2)	2,066.836(31)	2,082.9757(143)
C (MHz)	1,928.46(2)	1,923.194(32)	1,929.8998(144)
ΔJ (kHz)	21.90(2)	22.34(4)	21.1575(160)
ΔJK (kHz)	371.7(1)	408.34(68)	375.668(155)
ΔK (kHz)	-	-	1406.52(88)
δJ (kHz)	1.61(8)	1.85(2)	2.211(66)
δk (kHz)	474.(10)	370.(16)	332.8(82)
ΦJ (kHz)	-	-	-0.018680(278)
ΦJK (kHz)	-	-	-0.1359(56)
ΦKJ (kHz)	-	-	0.703(39)
ΦK (kHz)	10.1(8)	-	8.700(79)
ϕJ (Hz)	-	-	-22.40(63)
ϕJK (kHz)	-	-	-4.384(60)
ϕk (kHz)	-	-	-68.10(114)
LJ (Hz)	-	-	0.14754(177)
LJK (Hz)	-	-	15.339(272)
LJJK (Hz)	-	-	-1.452(35)
LKKJ (Hz)	-	-	-24.45(238)
LK (Hz)	-	-	-97.27(249)
lJ (Hz)	-	-	-0.4615(34)
lJK (Hz)	-	-	61.34(41)
lKJ (Hz)	-	-	-491.9(55)
lK (kHz)	-	-	1.9752(279)
PJ (mHz)	-	-	-0.0353(34)
PJK (Hz)	-	-	0.21087(198)
PKJ (Hz)	-	-	-1.0935(179)
PJJK (Hz)	-	-	-0.012780(88)
PKKJ (Hz)	-	-	1.804(55)
pJ (mHz)	-	-	0.9794(62)
pJJK (Hz)	-	-	-0.02388(76)
pKKJ (Hz)	-	-	6.609(37)
pK (Hz)	-	-	-20.23(32)
pJK (Hz)	-	-	-0.4094(74)
RMS (kHz)	-	-	76.748

Chapter 6 Conclusions and Future Works

In this thesis, the goal of producing and recording the millimeter/submillimeter spectrum of protonated methanol was discussed. This goal requires a significant amount of instrumentation development in order to succeed, and the work presented herein focuses on this aspect of the project. This development included more sensitive detection techniques, and techniques that will be able to help assign the spectra produced by this highly fluxional ion. The developed techniques include PVTLI, LIFS, and MW-mm double resonance. In addition to the developments in the spectroscopic instrumentation, research had to be conducted on how to best produce this ion. Thus, the development of a number of different ion sources was necessary. Instead of directly searching for an ion that has no previously recorded millimeter/submillimeter spectrum, it was decided to test the production of protonated formaldehyde with these new ion sources. This ion is structurally similar to that of protonated methanol and the proposed pathway to ion formation was also the same. This made it an excellent candidate to test how effective the ion sources were at protonation. In addition to testing the ion sources, there was still a large amount of frequency space that had not be previously scanned. This made the target ion of protonated formaldehyde an ideal choice. Unfortunately, while initial attempts at producing protonated formaldehyde were successful, the production was not stable or consistent enough to extended the millimeter/submillimeter spectrum past 385 GHz. Lastly as a means to help declutter the eventual spectrum of protonated methanol, the investigation of methanol-based clusters began. Producing the millimeter/submillimeter spectrum of methanol-based clusters has the benefit of decreasing the amount of unassigned lines in the initial protonated methanol scans, but also allows one to compare these cluster lines to astronomical data in order to determine if these clusters are seen in the ISM. With

our initial investigation into these clusters, only the argon-methanol cluster has been observed and been assigned in the frequency range of 130-225 GHz.

Bibliography

1. Koga, T. & Naraoka, H. A new family of extraterrestrial amino acids in the Murchison meteorite. *Scientific Reports* **7,** 760. doi:10.1038/s41598-017-00693-9 (07/2017).
2. Garrod, R. T. & Widicus Weaver, S. L. Simulations of Hot-Core Chemistry. *Chemical Reviews* **113.** PMID: 24024866, 8939–8960. doi:10.1021/cr400147g (2013).
3. Herbst, E. The chemistry of interstellar space. *Chem. Soc. Rev.* **30,** 168–176. doi:10.1039/A909040A (3 2001).
4. Herbst, E. & van Dishoeck, E. F. Complex Organic Interstellar Molecules. **47,** 427–480. doi:10.1146/annurev-astro-082708-101654 (09/2009).
5. van Dishoeck, E. F., Blake, G. A., Jansen, D. J. & Groesbeck, T. D. Molecular Abundances and Low-Mass Star Formation. II. Organic and Deuterated Species toward IRAS 16293-2422. **447,** 760. doi:10.1086/175915 (07/1995).
6. Agúndez, M. & Wakelam, V. Chemistry of Dark Clouds: Databases, Networks, and Models. *Chemical Reviews* **113,** 8710–8737. ISSN: 1520-6890. doi:10.1021/cr4001176 (10/2013).
7. Indriolo, N. & McCall, B. J. Cosmic-ray astrochemistry. *Chem. Soc. Rev.* **42,** 7763–7773. doi:10.1039/C3CS60087D (19 2013).
8. Garrod, R. T., Weaver, S. L. W. & Herbst, E. Complex Chemistry in Star-forming Regions: An Expanded Gas-Grain Warm-up Chemical Model. *The Astrophysical Journal* **682,** 283 (2008).
9. Van Dishoeck, E. F. Astrochemistry of dust, ice and gas: introduction and overview. *Faraday Discuss.* **168,** 9–47. ISSN: 1364-5498. doi:10.1039/c4fd00140k (2014).
10. Wirström, E. S. *et al.* Observational tests of interstellar methanol formation. *A&A* **533,** A24. doi:10.1051/0004-6361/201116525 (2011).
11. Theulé, P. *et al.* Thermal reactions in interstellar ice: A step towards molecular complexity in the interstellar medium. *Advances in Space Research* **52,** 1567–1579. ISSN: 0273-1177. doi:https://doi.org/10.1016/j.asr.2013.06.034 (2013).
12. Öberg, K. I. Photochemistry and Astrochemistry: Photochemical Pathways to Interstellar Complex Organic Molecules. *Chemical Reviews* **116.** PMID: 27099922, 9631–9663. doi:10.1021/acs.chemrev.5b00694 (2016).

13. Maity, S., Kaiser, R. I. & Jones, B. M. Formation of complex organic molecules in methanol and methanol–carbon monoxide ices exposed to ionizing radiation – a combined FTIR and reflectron time-of-flight mass spectrometry study. *Phys. Chem. Chem. Phys.* **17,** 3081–3114. doi:10.1039/C4CP04149F (5 2015).

14. Motiyenko, R. A., Margulès, L., Despois, D. & Guillemin, J.-C. Laboratory spectroscopy of methoxymethanol in the millimeter-wave range. *Phys. Chem. Chem. Phys.* **20,** 5509–5516. doi:10.1039/C7CP05932A (8 2018).

15. Ohishi, M., Suzuki, T., Hirota, T., Saito, M. & Kaifu, N. Detection of a new methylamine (CH_3NH_2) source: Candidate for future glycine surveys. *Publications of the Astronomical Society of Japan* **71.** 86. ISSN: 0004-6264. doi:10.1093/pasj/psz068 (07/2019).

16. Caruana, D. J. & Holt, K. B. Astroelectrochemistry: the role of redox reactions in cosmic dust chemistry. *Phys. Chem. Chem. Phys.* **12,** 3072–3079. doi:10.1039/B917817A (13 2010).

17. Gamez-Garcia, V. G. & Galano, A. Systematic Search for Chemical Reactions in Gas Phase Contributing to Methanol Formation in Interstellar Space. *The Journal of Physical Chemistry A* **121.** PMID: 28885025, 7393–7400. doi:10.1021/acs.jpca.7b05797 (2017).

18. Geppert, W. D. *et al.* Dissociative recombination of protonated methanol. *Faraday Discuss.* **133,** 177–190. doi:10.1039/B516010C (0 2006).

19. Jusko, P. *et al.* The FELion cryogenic ion trap beam line at the FELIX free-electron laser laboratory: infrared signatures of primary alcohol cations. *Faraday Discuss.* **217,** 172–202. doi:10.1039/C8FD00225H (0 2019).

20. Luca, A., Voulot, D. & Gerlich, D. *Low temperature reactions between stored ions and condensable gases: formation of protonated methanol via radiative association* 2002.

21. Lawson, P. A., Osborne, D. S. & Adams, N. G. Experimental electron-ion dissociative recombination rate constant and temperature dependence data for protonated methanol, ethanol, dimethyl ether and diethyl ether. *International Journal of Mass Spectrometry* **373,** 22–26. ISSN: 1387-3806. doi:https://doi.org/10.1016/j.ijms.2014.08.029 (2014).

22. Kleiner, I. Spectroscopy of Interstellar Internal Rotors: An Important Tool for Investigating Interstellar Chemistry. *ACS Earth and Space Chemistry* **3,** 1812–1842. doi:10.1021/acsearthspacechem.9b00079 (2019).

23. Autler, S. H. & Townes, C. H. Stark Effect in Rapidly Varying Fields. *Phys. Rev.* **100,** 703–722. doi:10.1103/PhysRev.100.703 (2 10/1955).

24. Widicus Weaver, S. L. Millimeterwave and Submillimeterwave Laboratory Spectroscopy in Support of Observational Astronomy. *Annual Review of Astronomy and Astrophysics* **57,** 79–112. doi:10.1146/annurev-astro-091918-104438 (2019).

25. Kroll, J. A., Shipman, S. T. & Weaver, S. L. W. The rotational spectrum of methyl ethyl ketone in its ground vibrational state. *Journal of Molecular Spectroscopy* **295,** 52–57. ISSN: 0022-2852. doi:https://doi.org/10.1016/j.jms.2013.10.005 (2014).

26. McCarthy, M. C., Zou, L. & Martin-Drumel, M.-A. To kink or not: A search for long-chain cumulenones using microwave spectral taxonomy. *The Journal of Chemical Physics* **146,** 154301. doi:10.1063/1.4981125 (2017).

27. Amano, T. & Warner, H. E. Laboratory detection of protonated formaldehyde (H2COH+). *APJL* **342,** L99–L101. doi:10.1086/185494 (07/1989).

28. Von Engel, A. *Ionized Gases* (Clarendon Press, 1955).

29. Thaddeus, P. & McCarthy, M. Carbon chains and rings in the laboratory and in space. *Spectrochimica Acta Part A: Molecular and Biomolecular Spectroscopy* **57,** 757–774. ISSN: 1386-1425. doi:https://doi.org/10.1016/S1386-1425(00)00442-X (2001).

30. Asvany, O. *et al.* High-Resolution Rotational Spectroscopy in a Cold Ion Trap: H_2D^+ and D_2H^+. *Phys. Rev. Lett.* **100,** 233004. doi:10.1103/PhysRevLett.100.233004 (23 06/2008).

31. Duncan, M. A. Infrared Laser Spectroscopy of Mass-Selected Carbocations. *The Journal of Physical Chemistry A* **116.** PMID: 23130985, 11477–11491. doi:10.1021/jp309037d (2012).

32. Petkie, D. T. *et al.* A fast scan submillimeter spectroscopic technique. *Review of Scientific Instruments* **68,** 1675–1683. doi:10.1063/1.1147970 (1997).

33. Melnik, D. G., Gopalakrishnan, S., Miller, T. A., De Lucia, F. C. & Belov, S. Submillimeter wave vibration–rotation spectroscopy of Ar·CO and Ar·ND_3. *The Journal of Chemical Physics* **114,** 6100–6106. doi:10.1063/1.1355660 (2001).

34. Hays, B. M., McCabe, M. N., Shipman, S. T. & Widicus Weaver, S. L. Fast sweep direct absorption (sub)millimeter-wave spectroscopy. *Review of Scientific Instruments* **87,** 113109. doi:10.1063/1.4967468 (2016).

35. Brown, G. G. *et al.* A broadband Fourier transform microwave spectrometer based on chirped pulse excitation. *Review of Scientific Instruments* **79,** 053103. doi:10.1063/1.2919120 (2008).

36. Zou, L., Hays, B. M. & Weaver, S. L. W. Weakly Bound Clusters in Astrochemistry? Millimeter and Submillimeter Spectroscopy of trans-HO_3 and Comparison to Astronomical Observations. *The Journal of Physical Chemistry A* **120,** 657–667. doi:10.1021/acs.jpca.5b09624 (2016).

37. Kaur, D. *et al.* Multipass cell for molecular beam absorption spectroscopy. *Appl. Opt.* **29,** 119–124. doi:10.1364/AO.29.000119 (01/1990).

38. Herriott, D. R. & Schulte, H. J. Folded Optical Delay Lines. *Appl. Opt.* **4,** 883–889. doi:10.1364/AO.4.000883 (08/1965).

39. Nagarajan, S., Neese, C. F. & De Lucia, F. C. Cavity-Based Medium Resolution Spectroscopy (CBMRS) in the THz: A Bridge Between High- and Low-Resolution Techniques for Sensor and Spectroscopy Applications. *IEEE Transactions on Terahertz Science and Technology* **7,** 233–243. ISSN: 2156-3446. doi:10.1109/TTHZ.2017.2680841 (05/2017).

40. Balle, T. J. & Flygare, W. H. Fabry–Perot cavity pulsed Fourier transform microwave spectrometer with a pulsed nozzle particle source. *Review of Scientific Instruments* **52,** 33–45. doi:10.1063/1.1136443 (1981).

41. Zhang, C.-H. & Sha, G.-H. Double Resonance Spectroscopy and Molecular Dynamics. *Science* **262,** 374–375. ISSN: 0036-8075. doi:10.1126/science.262.5132.374 (1993).

42. Schmitz, D., Shubert, V. A., Patterson, D., Krin, A. & Schnell, M. Phase Dependence of Double-Resonance Experiments in Rotational Spectroscopy. *The Journal of Physical Chemistry Letters* **6,** 1493–1498. doi:10.1021/acs.jpclett.5b00494 (2015).

43. Woods III, R. C., Ronn, A. M. & Wilson Jr., E. B. Double Resonance Modulated Microwave Spectrometer. *Review of Scientific Instruments* **37,** 927–933. doi:10.1063/1.1720367 (1966).

44. Martinache, L., Jans-bürli, S., Vogelsanger, B., Kresa, W. & Bauder, A. Microwave-microwave double-resonance experiments with pulsed molecular beams in crossed fabry-perot cavities. *Chemical Physics Letters* **149,** 424–428. ISSN: 0009-2614. doi:http://dx.doi.org/10.1016/0009-2614(88)85118-2 (1988).

45. Crabtree, K. N., Martinez, O., Barreau, L., Thorwirth, S. & McCarthy, M. C. Microwave Detection of Sulfoxylic Acid (HOSOH). *The Journal of Physical Chemistry A* **117,** 3608–3613. doi:10.1021/jp400742q (2013).

46. Crabtree, K. N. *et al.* Microwave spectral taxonomy: A semi-automated combination of chirped-pulse and cavity Fourier-transform microwave spectroscopy. *The Journal of Chemical Physics* **144,** 124201. doi:10.1063/1.4944072 (2016).

47. Martin-Drumel, M.-A., McCarthy, M. C., Patterson, D., McGuire, B. A. & Crabtree, K. N. Automated microwave double resonance spectroscopy: A tool to identify and characterize chemical compounds. *The Journal of Chemical Physics* **144,** 124202. doi:10.1063/1.4944089 (2016).

48. Reinhard, I., Callegari, C., Conjusteau, A., Lehmann, K. K. & Scoles, G. Single and Double Resonance Microwave Spectroscopy in Superfluid ^{4}He Clusters. *Phys. Rev. Lett.* **82,** 5036–5039. doi:10.1103/PhysRevLett.82.5036 (25 06/1999).

49. Wodarczyk, F. & Wilson, E. Radio frequency-microwave double resonance as a tool in the analysis of microwave spectra. *Journal of Molecular Spectroscopy* **37,** 445–463. ISSN: 0022-2852. doi:https://doi.org/10.1016/0022-2852(71)90176-7 (1971).

50. Sumiyoshi, Y., Katsunuma, H., Suma, K. & Endo, Y. Spectroscopy of Ar–SH and Ar–SD. I. Observation of rotation-vibration transitions of a van der Waals mode by double-resonance spectroscopy. *The Journal of Chemical Physics* **123,** 054324. doi:10.1063/1.1943967 (2005).

51. Markov, V. N., Xu, Y. & Jäger, W. Microwave-submillimeter wave double-resonance spectrometer for the investigation of van der Waals complexes. *Review of Scientific Instruments* **69,** 4061–4067. doi:10.1063/1.1149251 (1998).

52. Suma, K., Sumiyoshi, Y. & Endo, Y. Fourier transform microwave spectroscopy and Fourier transform microwave-millimeter wave double resonance spectroscopy of the ClOO radical. *The Journal of Chemical Physics* **121,** 8351–8359. doi:10.1063/1.1792591 (2004).

53. Jäger, W. & Gerry, M. C. L. Microwave-millimeter-wave double resonance experiments on Ar-CO. *The Journal of Chemical Physics* **102,** 3587–3592. doi:10.1063/1.468581 (1995).

54. Suma, K., Funato, W., Sumiyoshi, Y. & Endo, Y. Microwave and millimeter-wave spectroscopy of the open-shell van der Waals complex Ar-HO_2. *The Journal of Chemical Physics* **122,** 184302. doi:10.1063/1.1889429 (2005).

55. Green, D., Hammond, S., Keske, J. & Pate, B. H. Intramolecular vibrational energy redistribution and conformational isomerization in vibrationally excited 2-fluoroethanol: High-resolution, microwave-infrared double-resonance spectroscopy investigation of the asymmetric -CH_2(F) stretch near 2980 cm^{-1}. *The Journal of Chemical Physics* **110,** 1979–1989. doi:10.1063/1.477975 (1999).

56. Douglass, K. O. *et al.* Applications of Fourier transform microwave (FTMW) detected infrared–microwave double-resonance spectroscopy to problems in vibrational dynamics. *Journal of Molecular Spectroscopy* **239,** 29–40. ISSN: 0022-2852. doi:http://dx.doi.org/10.1016/j.jms.2006.05.015 (2006).

57. Lee, C. Y. & Pate, B. H. Dressed states of molecules and microwave-infrared double-resonance spectroscopic techniques employing an electric quadrupole focusing field. *The Journal of Chemical Physics* **107,** 10430–10439. doi:10.1063/1.474207 (1997).

58. Raston, P. L., Douberly, G. E. & Jäger, W. Single and double resonance spectroscopy of methanol embedded in superfluid helium nanodroplets. *The Journal of Chemical Physics* **141,** 044301. doi:10.1063/1.4887348 (2014).

59. Oka, T. New techniques in optical and infrared spectroscopy - Intracavity infrared-microwave double-resonance spectroscopy. *Philosophical Transactions of the Royal Society of London A: Mathematical, Physical and Engineering Sciences* **307,** 591–601. ISSN: 0080-4614. doi:10.1098/rsta.1982.0132 (1982).

60. Scappini, F., Kreiner, W. A., Frye, J. M. & Oka, T. Radiofrequency-infrared double-resonance spectroscopy of OsO_4 using microwave modulation sidebands on CO_2 laser lines. *Journal of Molecular Spectroscopy* **106,** 436–440. ISSN: 0022-2852. doi:http://dx.doi.org/10.1016/0022-2852(84)90174-7 (1984).

61. Ho, W. C., Pursell, C. J., Weliky, D. P., Takagi, K. & Oka, T. Infrared-microwave double resonance spectroscopy of molecular ions: HN_2^+. *The Journal of Chemical Physics* **93,** 87–93. doi:10.1063/1.459466 (1990).

62. Pursell, C. J., Weliky, D. P. & Oka, T. Collision-induced double resonance studies of HN_2^+ and HCN. *The Journal of Chemical Physics* **93,** 7041–7048. doi:10.1063/1.459426 (11/1990).

63. Goswami, M., Neill, J. L., Muckle, M., Pate, B. H. & Arunan, E. Microwave, infrared-microwave double resonance, and theoretical studies of $C_2H_4\cdots H_2S$ complex. *The Journal of Chemical Physics* **139,** 104303. doi:10.1063/1.4819787 (2013).

64. Callegari, C. *et al.* Finite size effects and rotational relaxation in superfluid helium nanodroplets: Microwave-infrared double-resonance spectroscopy of cyanoacetylene. *The Journal of Chemical Physics* **113,** 4636–4646. doi:10.1063/1.1288604 (2000).

65. Kerstel, E. R. T., Lehmann, K. K., Gambogi, J. E., Yang, X. & Scoles, G. The ν_1 vibrational predissociation lifetime of HCN_2 determined from upperstate microwave-infrared double-resonance measurements. *The Journal of Chemical Physics* **99,** 8559–8570. doi:10.1063/1.465579 (1993).

66. Henck, S. A., Mason, M. A., Yan, W.-B., Lehmann, K. K. & Coy, S. L. Microwave detected, microwave-optical double resonance of NH_3, NH_2D, NHD_2, and ND_3. I. Structure and force field of the $\tilde{A}$ state. *The Journal of Chemical Physics* **102,** 4772–4782. doi:10.1063/1.469525 (1995).

67. Henck, S. A., Mason, M. A., Yan, W.-B., Lehmann, K. K. & Coy, S. L. Microwave detected, microwave-optical double resonance of NH_3, NH_2D, NHD_2, and ND_3. II. Predissociation dynamics of the $\tilde{A}$ state. *The Journal of Chemical Physics* **102,** 4783–4792. doi:10.1063/1.469526 (1995).

68. Steimle, T. C., Zhang, R. & Heaven, M. C. The pure rotational spectrum of thorium monosulfide, ThS. *Chemical Physics Letters* **639,** 304–306. ISSN: 0009-2614. doi:https://doi.org/10.1016/j.cplett.2015.09.048 (2015).

69. Field, R. W., English, A. D., Tanaka, T., Harris, D. O. & Jennings, D. A. Microwave optical double resonance spectroscopy with a cw dye laser: BaO $X^1\Sigma$ and $A^1\Sigma$. *The Journal of Chemical Physics* **59,** 2191–2203. doi:10.1063/1.1680320 (1973).

70. Lehmann, K. K. & Coy, S. L. Use of microwave detected microwave-optical double resonance to assign the 6450 Å band of NH_3. *The Journal of Chemical Physics* **81,** 3744–3745. doi:10.1063/1.448128 (1984).

71. Lehmann, K. K. & Coy, S. L. Microwave detected, microwave-optical double resonance spectra of NO_2: A test of Hardwick's ergodicity conjecture. *The Journal of Chemical Physics* **83,** 3290–3296. doi:10.1063/1.449188 (1985).

72. Meulen, J. T., Ubachs, W. & Dymanus, A. Observation of ρ-doublet transitions in OH($A^2\Sigma^+_{1/2}$) by UV-microwave double resonance in a molecular beam. *Chemical Physics Letters* **129,** 533–537. ISSN: 0009-2614. doi:http://dx.doi.org/10.1016/0009-2614(86)80395-5 (1986).

73. Kerstel, E., Becucci, M., Pietraperzia, G. & Castellucci, E. High-resolution absorption, excitation, and microwave-UV double resonance spectroscopy on a molecular beam: S_1 aniline. *Chemical Physics* **199,** 263–273. ISSN: 0301-0104. doi:http://dx.doi.org/10.1016/0301-0104(95)00181-M (1995).

74. Boero, G. *et al.* Double-resonant x-ray and microwave absorption: Atomic spectroscopy of precessional orbital and spin dynamics. *Phys. Rev. B* **79,** 224425. doi:10.1103/PhysRevB.79.224425 (22 06/2009).

75. Merker, U., K. Srivastava, H., Callegari, A., K. Lehmann, K. & Scoles, G. Eigenstate resolved infrared and millimeter-wave-infrared double resonance spectroscopy of methylamine in the N-H stretch first overtone region. *Phys. Chem. Chem. Phys.* **1,** 2427–2433. doi:10.1039/A900370C (10 1999).

76. Matsuo, Y., Endo, Y., Hirota, E. & Shimizu, T. Direct observation of inversion transitions in the ν=5 state of NH_3 by millimeter wave-optical double resonance. *The Journal of Chemical Physics* **87,** 4395–4398. doi:10.1063/1.452900 (1987).

77. Matsuo, Y., Endo, Y., Hirota, E. & Shimizu, T. Inversion transition frequencies in the ν=5 state of NH_3 measured by millimeter wave-optical double resonance. *The Journal of Chemical Physics* **88,** 2852–2852. doi:10.1063/1.453971 (1988).

78. Park, G. B. *et al.* Millimeter-wave optical double resonance schemes for rapid assignment of perturbed spectra, with applications to the $\tilde{C}\ ^1B_2$ state of SO_2. *The Journal of Chemical Physics* **142,** 144201. doi:10.1063/1.4916908 (2015).

79. Coy, S. L., Lehmann, K. K. & Lucia, F. C. D. Millimeter-wave optical double resonance spectra of NO_2: How good a quantum number is N? *The Journal of Chemical Physics* **85,** 4297–4303. doi:10.1063/1.451825 (1986).

80. Callegari, A. *et al.* Eigenstate resolved infrared-infrared double-resonance study of intramolecular vibrational relaxation in benzene: First overtone of the CH stretch. *The Journal of Chemical Physics* **106,** 432–435. doi:10.1063/1.473205 (1997).

81. Andrews, A. M., Fraser, G. T. & Pate, B. H. Molecular-beam infrared-infrared double-resonance spectroscopy study of the vibrational dynamics of the acetylenic C-H stretch of propargyl amine. *The Journal of Chemical Physics* **109,** 4290–4301. doi:10.1063/1.477033 (1998).

82. Gambogi, J. E., Kerstel, E. R. T., Lehmann, K. K. & Scoles, G. Eigenstate resolved infrared/infrared double resonance spectroscopy of the $3\nu_1$ overtone band of 1-propyne: Intramolecular vibrational energy redistribution into a Coriolis-coupled bath. *The Journal of Chemical Physics* **100,** 2612–2622. doi:10.1063/1.467230 (1994).

83. Srivastava, H. K. *et al.* A sub-Doppler resolution double resonance molecular beam infrared spectrometer operating at chemically relevant energies (∼2 eV). *Review of Scientific Instruments* **71,** 4032–4038. doi:10.1063/1.1310343 (2000).

84. Dean, J. C. *et al.* UV Photofragmentation and IR Spectroscopy of Cold, G-Type β-O-4 and β-β Dilignol–Alkali Metal Complexes: Structure and Linkage-Dependent Photofragmentation. *The Journal of Physical Chemistry A* **119,** 1917–1932. doi:10.1021/jp512603n (2015).

85. Baraban, J. H. *et al.* The $\tilde{A}^1A_u$ state of acetylene: ungerade vibrational levels in the region 45,800-46,550cm^{-1}. *Molecular Physics* **110,** 2707–2723. doi:10.1080/00268976.2012.706329 (2012).

86. Park, G. B., Jiang, J., Saladrigas, C. A. & Field, R. W. Observation of b_2 symmetry vibrational levels of the SO_2 $\tilde{C}$ $^1B_2$ state: Vibrational level staggering, Coriolis interactions, and rotation-vibration constants. *The Journal of Chemical Physics* **144,** 144311. doi:10.1063/1.4944924 (2016).

87. Changala, P. B., Baraban, J. H., Merer, A. J. & Field, R. W. Probing cis-trans isomerization in the S_1 state of C_2H_2 via H-atom action and hot band-pumped IR-UV double resonance spectroscopies. *The Journal of Chemical Physics* **143,** 084310. doi:10.1063/1.4929588 (2015).

88. Page, R. H., Shen, Y. R. & Lee, Y. T. Infrared-ultraviolet double resonance studies of benzene molecules in a supersonic beam. *The Journal of Chemical Physics* **88,** 5362–5376. doi:10.1063/1.454574 (1988).

89. Kugel, H. W., Leventhal, M., Murnick, D. E., Patel, C. K. N. & Wood, O. R. Infrared-X-Ray Double-Resonance Study of $2P_{\frac{3}{2}} - 2S_{\frac{1}{2}}$ Splitting in Hydrogenic Fluorine. *Phys. Rev. Lett.* **35,** 647–650. doi:10.1103/PhysRevLett.35.647 (10 09/1975).

90. Urbanski, K., Antonova, S., Lyyra, A. M., Li, L. & Ji, B. The $G^1\Pi_g$ state of $^7Li_2$ revisited: Observation and analysis of high vibrational levels. *The Journal of Chemical Physics* **109,** 912–918. doi:10.1063/1.476632 (1998).

91. McCarthy, M. C., Kanamori, H., Li, M. & Field, R. W. Sideband optical-optical double resonance Zeeman spectroscopy. I. Theory of saturation and line shape behavior. *The Journal of Chemical Physics* **102,** 8295–8307. doi:10.1063/1.468822 (1995).

92. Li, M. & Field, R. W. Sideband optical-optical double resonance Zeeman spectroscopy of NiH: A new diagnostic for electronic and rotational assignment. *The Journal of Chemical Physics* **90,** 2967–2970. doi:10.1063/1.455897 (1989).

93. Hamilton, C. E., Kinsey, J. L. & Field, R. W. Stimulated Emission Pumping: New Methods in Spectroscopy and Molecular Dynamics. *Annual Review of Physical Chemistry* **37,** 493–524. doi:10.1146/annurev.pc.37.100186.002425 (10/1986).

94. Li, J. *et al.* Double-Resonance Spectroscopic Studies of Core-Penetrating Rydberg States of CaCl. *Journal of Molecular Spectroscopy* **193,** 403–411. ISSN: 0022-2852. doi:http://dx.doi.org/10.1006/jmsp.1998.7746 (1999).

95. Tandy, J., Wang, J.-G., Liévin, J. & Bernath, P. Investigating the electronic states of BaOH by V-type double resonance spectroscopy and *ab initio* calculations: Further evidence of perturbation from the $\tilde{A}'^2\Delta$ state. *Journal of Molecular Spectroscopy* **270,** 44–50. ISSN: 0022-2852. doi:http://dx.doi.org/10.1016/j.jms.2011.08.009 (2011).

96. Lundberg, J. K., Chen, Y., Pique, J.-P. & Field, R. W. Ultraviolet-Optical Double-Resonance study of the predissociated C'^1 A_g state of acetylene. *Journal of Molecular Spectroscopy* **156,** 104–122. ISSN: 0022-2852. doi:http://dx.doi.org/10.1016/0022-2852(92)90097-8 (1992).

97. Mehta-Hurt, D. N. *et al.* The spectroscopy and photochemistry of quinioline structural isomers: (E)- and (Z)-phenylvinylnitrile. *The Journal of Chemical Physics* **143,** 074304. doi:10.1063/1.4928191 (2015).

98. Lundberg, J. K., Jonas, D. M., Rajaram, B., Chen, Y. & Field, R. W. Rotationally resolved ultraviolet-ultraviolet double resonance study of the nonplanar $\tilde{E}$ state of acetylene. *The Journal of Chemical Physics* **97,** 7180–7196. doi:10.1063/1.463543 (1992).

99. Iketaki, Y. & Watanabe, T. Study of x-ray microscopy using ultraviolet and x-ray double-resonance absorption. *Optical Engineering* **35,** 2418–2422. doi:10.1117/1.600815 (1996).

100. El-Sayed, M. A. Phosphorescence microwave multiple resonance studies in determining the radiative and nonradiative properties of the triplet state. *Accounts of Chemical Research* **4,** 23–31. doi:10.1021/ar50037a004 (1971).

101. Cheng, T. H. & Hirota, N. Steady State and Transient Phosphorescence Microwave Double Resonance (PMDR) Studies of Aromatic Carbonyl Molecules; Studies of Experimental Conditions and Properties of π-π^* Triplet States. *The Journal of Chemical Physics* **56,** 5019–5034. doi:10.1063/1.1676983 (1972).

102. Pickett, H. *et al.* Submillimeter, Millimeter, And Microwave Spectral Line Catalog. *Journal of Quantitative Spectroscopy and Radiative Transfer* **60,** 883–890. ISSN: 0022-4073. doi:http://dx.doi.org/10.1016/S0022-4073(98)00091-0 (1998).

103. Shubert, V. A. *et al.* Chiral Analysis Using Broadband Rotational Spectroscopy. *The Journal of Physical Chemistry Letters* **7.** PMID: 26745342, 341–350. doi:10.1021/acs.jpclett.5b02443 (2016).

104. Chomiak, D., Taleb-Bendiab, A., Civis, S. & Amano, T. Millimetre-wave laboratory detection of H_2COH^+. *Canadian Journal of Physics* **72,** 1078–1081. doi:10.1139/p94-140 (1994).

105. Dore, L., Cazzoli, G., Civiš, S. & Scappini, F. Extended measurements of the millimeter wave spectrum of H_2COH^+. *Chemical Physics Letters* **244,** 145–148. ISSN: 0009-2614. doi:http://dx.doi.org/10.1016/0009-2614(95)00816-M (1995).

106. Dore, L., Cazzoli, G., Civiš, S. & Scappini, F. Millimeter-Wave Spectra of $H_2^{13}COH^+$ and D_2COD^+. *Journal of Molecular Spectroscopy* **183,** 107–112. ISSN: 0022-2852. doi:https://doi.org/10.1006/jmsp.1996.7229 (1997).

107. Bowen, R. D. & Williams, D. H. CH_3O^+ and $C_2H_5O^+$: high barriers to isomerisation and low barriers to symmetry-allowed 1,1-elimination. *J. Chem. Soc., Chem. Commun.,* 378–380. doi:10.1039/C39770000378 (11 1977).

108. Dill, J. D., Fischer, C. L. & McLafferty, F. W. Collisional activation and theoretical studies of gaseous COH_3^+ ions. *Journal of the American Chemical Society* **101,** 6531–6534. doi:10.1021/ja00516a010 (1979).

109. Osborne Jr., D. S., Lawson, P. A. & Adams, N. G. A study of the electron–ion dissociative recombination rate constants of the isotopomers of protonated carbon monoxide (HCO^+) and formaldehyde (H_3CO^+). *International Journal of Mass Spectrometry* **378.** SI: Bierbaum 65th Birthday, 193–195. ISSN: 1387-3806. doi:http://dx.doi.org/10.1016/j.ijms.2014.08.001 (2015).

110. Mosley, J. D., Cheng, T. C., McCoy, A. B. & Duncan, M. A. Infrared Spectroscopy of the Mass 31 Cation: Protonated Formaldehyde vs Methoxy. *The Journal of Physical Chemistry A* **116.** PMID: 22946445, 9287–9294. doi:10.1021/jp3072298 (2012).

111. Ros, P. Nonempirical Molecular-Orbital Calculations for Protonated Formaldehyde, Acetaldehyde, and Formic Acid. *The Journal of Chemical Physics* **49,** 4902–4916. doi:10.1063/1.1669978 (1968).

112. Schleyer, P. V. R., Jemmis, E. D. & Pople, J. A. 'CH_3O^+' and $CH_2{=}O^+H$: High barriers to isomerization. *J. Chem. Soc., Chem. Commun.,* 190–191. doi:10.1039/C39780000190 (5 1978).

113. Johansen, R. & Nilssen, E. W. AB initio hartree-fock and CI calculations on the bonding and stability of $[H_3CO]^+$ formed from $[HCO]^+$ and H_2. *Journal of Molecular Structure* **49,** 131–136. ISSN: 0022-2860. doi:http://dx.doi.org/10.1016/0022-2860(78)87012-4 (1978).

114. Hoffmann, M. & Schaefer H.F., I. Hydroxycarbene /HCOH/ and protonated formaldehyde - Two potentially observable interstellar molecules. **249,** 563–565. doi:10.1086/159315 (10/1981).

115. Defrees, D. & McLean, A. A priori predictions of the rotational constants for protonated formaldehyde and protonated methanol. *Chemical Physics Letters* **131,** 403–408. ISSN: 0009-2614. doi:http://dx.doi.org/10.1016/0009-2614(86)87175-5 (1986).

116. Del Bene, J. E., Gwaltney, S. R. & Bartlett, R. J. Base Properties of H_2CO in the Excited ln pi* State. *The Journal of Physical Chemistry A* **102,** 5124–5127. doi:10.1021/jp981093y (1998).

117. Blowers, P. & Masel, R. I. Calculated Vibrational Spectra for CH_nOH_m Species. *The Journal of Physical Chemistry A* **104,** 34–44. doi:10.1021/jp992343t (2000).

118. Castro, M. E., Niño, A. & Muñoz-Caro, C. Structural and vibrational theoretical analysis of protonated formaldehyde in its $\tilde{X}^1$ A' ground electronic state. *Theoretical Chemistry Accounts* **119,** 343–354. ISSN: 1432-2234. doi:10.1007/s00214-007-0392-5 (2008).

119. Aschi, M., N. Harvey, J., A. Schalley, C., Schröder, D. & Schwarz, H. Reappraisal of the spin-forbidden unimolecular decay of the methoxy cation†. *Chem. Commun.,* 531–533. doi:10.1039/A708642C (5 1998).

120. Sears, K. C., Ferguson, J. W., Dudley, T. J., Houk, R. S. & Gordon, M. S. Theoretical Investigation of Small Polyatomic Ions Observed in Inductively Coupled Plasma Mass Spectrometry: H_xCO^+ and $H_xN_2^+$ (x = 1, 2, 3). *The Journal of Physical Chemistry A* **112.** PMID: 18311946, 2610–2617. doi:10.1021/jp077209k (2008).

121. Antol, I., Eckert-Maksić, M., M Uller, T., Dallos, M. & Lischka, H. Valence and Rydberg states of protonated formaldehyde. *Chemical Physics Letters* **374,** 587–593. ISSN: 0009-2614. doi:http://dx.doi.org/10.1016/S0009-2614(03)00770-X (2003).

122. Jalbout, A. Can protonated glycoaldehyde and methyl formate form in the interstellar medium (ISM)? *Molecular Physics* **105,** 941–949. doi:10.1080/00268970701218696 (2007).

123. Halfen, D. T., Apponi, A. J., Woolf, N., Polt, R. & Ziurys, L. M. A Systematic Study of Glycolaldehyde in Sagittarius B2(N) at 2 and 3 mm: Criteria for Detecting Large Interstellar Molecules. *The Astrophysical Journal* **639,** 237–245. doi:10.1086/499225 (03/2006).

124. Ohishi, M. *et al.* Detection of A New Interstellar Molecular Ion, H_2COH^+ (Protonated Formaldehyde). *The Astrophysical Journal* **471,** L61–L64. doi:10.1086/310325 (11/1996).

125. Jones, P. A., Burton, M. G., Tothill, N. F. H. & Cunningham, M. R. Spectral imaging of the Sagittarius B2 region in multiple 7-mm molecular lines. *Monthly Notices of the Royal Astronomical Society* **411,** 2293–2310. ISSN: 0035-8711. doi:10.1111/j.1365-2966.2010.17849.x (03/2011).

126. Requena-Torres, M. A., Martin-Pintado, J., Martin, S. & Morris, M. R. The Galactic Center: The Largest Oxygen-bearing Organic Molecule Repository. *The Astrophysical Journal* **672,** 352–360. doi:10.1086/523627 (01/2008).

127. Bacmann, A., García-García, E. & Faure, A. Detection of protonated formaldehyde in the prestellar core L1689B. *Astronomy Astrophysics* **588,** L8. ISSN: 1432-0746. doi:10.1051/0004-6361/201628280 (03/2016).

128. Snyder, L. E., Buhl, D., Zuckerman, B. & Palmer, P. Microwave Detection of Interstellar Formaldehyde. *Phys. Rev. Lett.* **22,** 679–681. doi:10.1103/PhysRevLett.22.679 (13 03/1969).

129. Mangum, J. G., Wootten, A., Loren, R. B. & Wadiak, E. J. Observations of the Formaldehyde Emission in Orion-KL: Abundances, Distribution, and Kinematics of the Dense Gas in the Orion Molecular Ridge. **348,** 542. doi:10.1086/168262 (01/1990).

130. Ball, J. A., Gottlieb, C. A., Lilley, A. E. & Radford, H. E. Detection of Methyl Alcohol in Sagittarius. **162,** L203. doi:10.1086/180654 (12/1970).

131. Rodgers, S. & Charnley, S. Multiply deuterated molecules and constraints on interstellar chemistry. *Planetary and Space Science* **50.** Special issue on Deuterium in the Universe, 1125–1132. ISSN: 0032-0633. doi:https://doi.org/10.1016/S0032-0633(02)00073-9 (2002).

132. Osamura, Y., Roberts, H. & Herbst, E. The Gas-Phase Deuterium Fractionation of Formaldehyde. **621,** 348–358. doi:10.1086/427474 (03/2005).

133. Suenram, R. *et al.* Microwave spectrum, structure, and electric dipole moment of Ar-CH_3OH. *Journal of Molecular Spectroscopy* **137,** 127–137. ISSN: 0022-2852. doi:https://doi.org/10.1016/0022-2852(89)90274-9 (1989).

134. Tan, X., Sun, L. & Kuczkowski, R. The Methanol · Ar Complex: Apparent Reduction of the Methyl Group Internal Rotation Barrier. *Journal of Molecular Spectroscopy* **171,** 248–264. ISSN: 0022-2852. doi:https://doi.org/10.1006/jmsp.1995.1115 (1995).

135. Stockman, P. A., Blake, G. A., Lovas, F. J. & Suenram, R. D. Microwave rotation-tunneling spectroscopy of the water–methanol dimer: Direct structural proof for the strongest bound conformation. *The Journal of Chemical Physics* **107,** 3782–3790. doi:10.1063/1.474736 (1997).

136. Lovas, F. & Hartwig, H. The Microwave Spectrum of the Methanol Dimer for K= 0 and 1 States. *Journal of Molecular Spectroscopy* **185,** 98–109. ISSN: 0022-2852. doi:https://doi.org/10.1006/jmsp.1997.7371 (1997).

137. Lovas, F., Belov, S., Tretyakov, M., Stahl, W. & Suenram, R. The a-Type K = 0 Microwave Spectrum of the Methanol Dimer. *Journal of Molecular Spectroscopy* **170,** 478–492. ISSN: 0022-2852. doi:https://doi.org/10.1006/jmsp.1995.1086 (1995).

138. Ohashi, N. & Hougen, J. Analysis and Global Fit of Tunneling Splittings in the K = 0 a-Type Microwave Spectrum of the Methanol Dimer. *Journal of Molecular Spectroscopy* **170,** 493–505. ISSN: 0022-2852. doi:https://doi.org/10.1006/jmsp.1995.1087 (1995).

139. Tasić, U. *et al.* Ab initio and analytic intermolecular potentials for Ar–CH_3OH. *Phys. Chem. Chem. Phys.* **8,** 4678–4684. doi:10.1039/B609743J (40 2006).

140. Cappelletti, D., Candori, P., Falcinelli, S., Albertí, M. & Pirani, F. A molecular beam scattering investigation of methanol–noble gas complexes: Characterization of the isotropic potential and insights into the nature of the interaction. *Chemical Physics Letters* **545,** 14–20. ISSN: 0009-2614. doi:https://doi.org/10.1016/j.cplett.2012.07.020 (2012).

141. Han, H.-L., Camacho, C., Witek, H. A. & Lee, Y.-P. Infrared absorption of methanol clusters $(CH_3OH)n$ with n = 26 recorded with a time-of-flight mass spectrometer using infrared depletion and vacuum-ultraviolet ionization. *The Journal of Chemical Physics* **134,** 144309. doi:10.1063/1.3572225 (2011).

142. Provencal, R. A. *et al.* Infrared cavity ringdown spectroscopy of methanol clusters: Single donor hydrogen bonding. *The Journal of Chemical Physics* **110,** 4258–4267. doi:10.1063/1.478309 (1999).

143. Klemperer, W. & Vaida, V. Molecular complexes in close and far away. *Proceedings of the National Academy of Sciences* **103,** 10584–10588. ISSN: 0027-8424. doi:10.1073/pnas.0508231103 (2006).

144. Dunning, F. & Hulet, R. *Atomic, Molecular, and Optical Physics: Atoms and Molecules* ISBN: 9780080860183 (Elsevier Science, 1996).

145. *Principles of lock-in detection and the state of the art* Zurich Instruments, 11/2016.

146. *MODEL SR830DSP Lock-In Amplifier* Stanford Research Systems (2011).

147. Zou, L. *Astrochemistry in Star-forming Regions: Laboratory Millimeter–Submillimeter Spectroscopy and Broadband Astronomical Line Surveys* PhD thesis (Emory University, 2012).

148. Laas, J. C., Hays, B. M. & Widicus Weaver, S. L. Multipass Millimeter/Submillimeter Spectrometer to Probe Dissociative Reaction Dynamics. *The Journal of Physical Chemistry A* **117,** 9548–9554. doi:10.1021/jp3122402 (2013).

149. Cohen-Tannoudji, C. N. in *Amazing Light: A Volume Dedicated To Charles Hard Townes On His 80th Birthday* (ed Chiao, R. Y.) 109–123 (Springer New York, New York, NY, 1996). ISBN: 978-1-4612-2378-8. doi:10.1007/978-1-4612-2378-8_11.

150. Ahmed, E. H., Huennekens, J., Kirova, T., Qi, J. & Lyyra, A. M. in *Advances in Atomic, Molecular, and Optical Physics* (eds Berman, P., Arimondo, E. & Lin, C.) *Advances In Atomic, Molecular, and Optical Physics* Supplement C, 467–514 (Academic Press, 2012). doi:https://doi.org/10.1016/B978-0-12-396482-3.00009-0.

151. Yariv, A. *Quantum electronics* ISBN: 9780471609971 (Wiley, 1989).

152. Gagliardi, G. & Loock, H. *Cavity-Enhanced Spectroscopy and Sensing* ISBN: 9783642400032 (Springer Berlin Heidelberg, 2013).

153. Alligood DePrince, B., Rocher, B. E., Carroll, A. M. & Widicus Weaver, S. L. Extending high-finesse cavity techniques to the far-infrared. *Review of Scientific Instruments* **84,** 075107. doi:10.1063/1.4813274 (2013).

154. Zou, L. & Weaver, S. L. W. Direct measurement of additional Ar–H_2O vibration–rotation-tunneling bands in the millimeter–submillimeter range. *Journal of Molecular Spectroscopy* **324,** 12–19. ISSN: 0022-2852. doi:https://doi.org/10.1016/j.jms.2016.04.010 (2016).

155. Tretyakov, M. Y. *et al.* Water dimer and the atmospheric continuum. *Physics-Uspekhi* **57,** 1083–1098. doi:10.3367/ufne.0184.201411c.1199 (11/2014).

156. *Splatalogue Database for Astronomical Spectroscopy* National Radio Astronomy Observatory (2012).

157. Pickett, H. M. The fitting and prediction of vibration-rotation spectra with spin interactions. *Journal of Molecular Spectroscopy* **148,** 371–377. ISSN: 0022-2852. doi:https://doi.org/10.1016/0022-2852(91)90393-O (1991).